ABSTRACT

A Search for the Standard Model Higgs Boson
Produced in Association with a W Boson

Martin J. Frank, Ph.D.

Advisor: Jay R. Dittmann, Ph.D.

We present a search for a standard model Higgs boson produced in association with a W boson using data collected with the CDF II detector from $p\bar{p}$ collisions at $\sqrt{s} = 1.96$ TeV. The search is performed in the $WH \to \ell\nu b\bar{b}$ channel. The two quarks usually fragment into two jets, but sometimes a third jet can be produced via gluon radiation, so we have increased the standard two-jet sample by including events that contain three jets. We reconstruct the Higgs boson using two or three jets depending on the kinematics of the event. We find an improvement in our search sensitivity using the larger sample together with this multijet reconstruction technique. Our data show no evidence of a Higgs boson, so we set 95% confidence level upper limits on the WH production rate. We set limits between 3.36 and 28.7 times the standard model prediction for Higgs boson masses ranging from 100 to 150 GeV/c^2.

A Search for the Standard Model Higgs Boson
Produced in Association with a W Boson

by

Martin J. Frank, B.S.

A Dissertation

Approved by the Department of Physics

Gregory A. Benesh, Ph.D., Chairperson

Submitted to the Graduate Faculty of
Baylor University in Partial Fulfillment of the
Requirements for the Degree
of
Doctor of Philosophy

Approved by the Dissertation Committee

Jay R. Dittmann, Ph.D., Chairperson

Gregory A. Benesh, Ph.D.

Kenichi Hatakeyama, Ph.D.

Klaus Kirsten, Ph.D.

Anzhong Wang, Ph.D.

Accepted by the Graduate School
May 2011

J. Larry Lyon, Ph.D., Dean

Page bearing signatures is kept on file in the Graduate School.

Copyright © 2011 by Martin J. Frank
All rights reserved

TABLE OF CONTENTS

LIST OF FIGURES

LIST OF TABLES

LIST OF ABBREVIATIONS

CDF: Collider Detector at Fermilab.

CEM: Central electromagnetic calorimeter. We refer to CEM electrons when they were detected with the CEM.

CES: Central electromagnetic shower chamber system, which is located within the CEM.

CHA: Central hadronic calorimeter.

CLC: Cherenkov luminosity counter.

CMP: Central muon upgrade system.

CMU: Central muon system.

CMUP: The combination of the CMU and CMP system. We refer to CMUP muons when they were detected with the combined CMUP system.

CMX: Central muon extension system. We refer to CMX muons when they were detected with the CMX.

COT: Central outer tracker.

CPR: Central preradiator, which is located within the CEM.

HF: Heavy Flavor. This refers to heavy-flavored quarks, which are c, b in this analysis.

ISL: The intermediate silicon layers detector, the outermost part of the silicon detector.

LF: Light Flavor. This refers to light-flavored quarks, which are u, d, and b in this analysis.

MC: Monte Carlo. We use Monte Carlo simulations to model our signal and backgrounds.

PHA: Plug hadronic calorimeter.

PHX: Phoenix electrons. These are electrons that are detected with the PEM and have a Phoenix track.

PES: Plug electromagnetic shower chamber system, which is located within the PEM.

PEM: Plug electromagnetic calorimeter.

PPR: Plug preradiator, which is located within the PEM.

RF: Radio frequency. We use radio frequency cavities to accelerate charged particles.

SVX II: The silicon vertex detector of the CDF II detector.

TLEP: Tight lepton category, which consists of the sum of the CEM, CMUP, and CMX lepton categories.

WHA: Wall hadronic calorimeter.

WH: This refers to Higgs (H) production in association with a W boson.

XFT: eXtremely Fast Tracker. A subsystem of the CDF II trigger system that reconstructs tracks from the COT.

ACKNOWLEDGMENTS

I would like to thank my colleagues at Fermilab for their support during my analysis and detector work. The *WH* group has been a large part of my work at Fermilab, and I want to thank Drs. Weiming Yao and Craig Group for their leadership. My work would have been impossible if it were not for the guidance of Dr. Yoshikazu Nagai who helped me with every step of the analysis from the very beginning, for which I am very grateful. It was a pleasure to work with my fellow graduate students, Dr. Justin Keung, Timo Aaltonen, Adrian Buzatu, and Dr. Jason Slaunwhite, who showed me how important mutual encouragement can be. I also want to thank Dr. Homer Wolfe for his motivation and affirmation of my work and the CDF operations team for teaching me so much about the detector and accelerator while I was on shift; it was a wonderful learning experience. Of course, all of this work at CDF would not have been possible without the generous support of CDF's funding agencies, especially the United States Department of Energy, which funds our Baylor High Energy Physics (HEP) research group.

I am also grateful to Baylor University for the generous Presidential Scholar Program that supported me for the past five years and the Baylor Travel Awards that allowed me to attend several conferences across the United States. When I first came to Baylor, the Physics Department funded my work with a teaching assistantship, which I am very grateful for. It was a wonderful experience to serve as a teaching assistant under Drs. Linda Kinslow and Tibra Ali at Baylor and the late Dr. Mary Creason at Duke.

It has been a true honor to be part of the Baylor Physics Department, which is nothing short of one of the finest physics departments in the world. The exemplary leadership of Prof. Greg Benesh always ensured that we graduate students had nothing to worry about and could focus on our studies. I also want to thank the excellent

teachers who instructed me, Professors Jay Dittmann, Anzhong Wang, Yumei Wu, Gerald Cleaver, and Bennie Ward. I am also grateful to Mrs. Marian Nunn-Graves and Mrs. Chava Baker from the front office for always helping me so kindly with everything I needed. I would also like to thank the Baylor Mathematics Department for allowing me to use their LaTeX class file. Finally, I want to thank Professors Jay Dittmann, Ken Hatakeyama, Anzhong Wang, Greg Benesh and Klaus Kirsten for taking the time to serve on my dissertation committee.

While I was at Duke for only a short time, I want to thank Prof. Mark Kruse for his guidance and for ultimately leading me to my dissertation advisor, Prof. Jay Dittmann at Baylor University. I can hardly find the words to thank Prof. Dittmann. He took me in when I transferred from Duke and has taught me what it means to be a rigorous, humble, and kind physicist. In Germany, we refer to dissertation advisors as doctoral fathers, and I believe that he has truly been a father to me during my time here at Baylor. It has been a great honor to be part of the Baylor HEP group. I learned an immeasurable amount from our first postdoc, Dr. Nils Krumnack, who equipped me with all the necessary tools to efficiently and effectively tackle any problem. It was wonderful to have such kind colleagues as Karen Bland, Ben Wu, Tara Scarborough, Dr. Azeddine Kasmi, Dr. Hongxuan Liu, and Prof. Ken Hatakeyama. I especially want to thank Samantha Hewamanage, who, as the first graduate student from our group to work at Fermilab, put a tremendous amount of effort into learning how things work at Fermilab and without hesitation passed all of that information to the rest of our group. I also want to thank Nils Holgersson from Baylor's Classroom Technology Services for providing us with and teaching me about Baylor's advanced video conferencing technology. My dream to work on interesting problems with good people has been more than fulfilled during my time with our Baylor HEP group.

Of course, it would be impossible to make it through graduate school without friends, and Baylor had plenty of them! In particular, I want to thank Dr. Richard Obousy, Dr. Andreas Tziolas, James Creel, and Dr. Antonio Sánchez-Bayón. For their spiritual guidance during my time at Baylor, I want to thank Rev. Dr. Robert Flowers and Fr. David Liebham. I also want to thank my friends from Duke, Adam Sokolow and Dr. Seth Henshaw. The time at Fermilab was also much improved thanks to my good friend Dr. Nils Hüske, a true kindred spirit whose family opened their home to me when the two of us traveled to the Bielefeld Summer School in Germany. Finally, I want to acknowledge my closest friend during my time here at Baylor, Tim Renner. We started at Baylor together and made it through classes, exams, good times and bad. We have had many epic discussions where we bridged the gap between theory and experiment.

Since I was a child, it has been my dream to become a physicist, and I would have never made it this far if it had not been for the loving support of my wonderful family. My father has always nourished the very pragmatic and scientific side of me, while my mother always nourished my theoretical and abstract side, and my sister always nourished my sense of being a family unit and the importance of always maintaining a sense of humor. With this combination of backgrounds, I feel that I have truly found what I love to do and I am so grateful to my entire family! Since I got married last August, my family has expanded to include a second set of parents and siblings. I am very grateful to Barbara and Stuart for taking me on as their son and Sam and Leah and Ben and Amy for embracing me as their true brother.

Baylor University has not only provided me with an unbelievable education, but has served as the place where I met my wife and where the two of us got to know each other. This dissertation is so far the accumulation of my academic achievements, but it is shadowed into complete insignificance when compared to the love that I found here at Baylor. Mary and I got married last year on August 7^{th}

and I never knew before then that such deep love exists. I am grateful to God for gracing us with this love and for strengthening it during this challenging time of completing my degree. It is Mary's love that got me here today, so I dedicate this dissertation to her.

This work is dedicated to my wife who is the love of my life.

CHAPTER ONE

Introduction

Since the time of Democritus, human beings have been interested in describing the known world using its most fundamental constituents. From molecules to atoms to protons, neutrons, and electrons, scientists have endeavored to break down matter into ever smaller particles. Today, we understand that even protons and neutrons are composite particles that consist of quarks. These fundamental particles are classified into two broad categories: fundamental matter particles and fundamental force-mediating particles. Tables 1.1 and 1.2 summarize these particles and some of their attributes.

The current standard model of the interactions between the fundamental particles is based on a theory of symmetries that requires that the particle masses conform to specific rules. For example, all the quark masses have to be equal and all of the leptons and force-mediating particles have to be massless. However, as Tables 1.1 and 1.2 show, this is not what experimentalists have measured. In 1964, Peter Higgs introduced a way to endow all of these particles with their measured masses by postulating the existence of a field to which these particles couple and thereby derive their mass. This field is today known as the "Higgs field," and if it exists, it would imply the existence of a so-called Higgs boson. This dissertation is about a search for this boson.

The next sections will explain the standard model, quantum field theory, gauge symmetries, the Higgs mechanism, and the motivation of searching for associated Higgs production.

Table 1.1: The fundamental particles and some of their attributes [7, 8]. The weak hypercharge (Y) and weak isospin (I_3) are related to the charge by $q = I_3 + \frac{1}{2}Y$. The subscripts on the particle symbols indicate the handedness: R for right and L for left. Note that right-handed neutrinos do not exist. The charge is expressed in units of the elementary charge (e).

Name	Symbol	Mass	Charge	Spin	I_3	Y
electron	e_L^-	0.511 MeV/c^2	-1	$\frac{1}{2}$	$-\frac{1}{2}$	-1
	e_R^-	0.511 MeV/c^2	-1	$\frac{1}{2}$	0	-2
muon	μ_L^-	106 MeV/c^2	-1	$\frac{1}{2}$	$-\frac{1}{2}$	-1
	μ_R^-	106 MeV/c^2	-1	$\frac{1}{2}$	0	-2
tau	τ_L^-	1777 MeV/c^2	-1	$\frac{1}{2}$	$-\frac{1}{2}$	-1
	τ_R^-	1777 MeV/c^2	-1	$\frac{1}{2}$	0	-2
electron neutrino	$(\nu_e)_L$	< 2 eV/c^2	0	$\frac{1}{2}$	$\frac{1}{2}$	-1
muon neutrino	$(\nu_\mu)_L$	< 2 eV/c^2	0	$\frac{1}{2}$	$\frac{1}{2}$	-1
tau neutrino	$(\nu_\tau)_L$	< 2 eV/c^2	0	$\frac{1}{2}$	$\frac{1}{2}$	-1
up quark	u_L	1.7–3.3 MeV/c^2	$\frac{2}{3}$	$\frac{1}{2}$	$\frac{1}{2}$	$\frac{1}{3}$
	u_R	1.7–3.3 MeV/c^2	$\frac{2}{3}$	$\frac{1}{2}$	0	$\frac{4}{3}$
down quark	d_L	4.1–5.8 MeV/c^2	$-\frac{1}{3}$	$\frac{1}{2}$	$-\frac{1}{2}$	$\frac{1}{3}$
	d_R	4.1–5.8 MeV/c^2	$-\frac{1}{3}$	$\frac{1}{2}$	0	$\frac{4}{3}$
charm quark	c_L	1.27 GeV/c^2	$\frac{2}{3}$	$\frac{1}{2}$	$\frac{1}{2}$	$\frac{1}{3}$
	c_R	1.27 GeV/c^2	$\frac{2}{3}$	$\frac{1}{2}$	0	$\frac{4}{3}$
strange quark	s_L	101 MeV/c^2	$-\frac{1}{3}$	$\frac{1}{2}$	$-\frac{1}{2}$	$\frac{1}{3}$
	s_R	101 MeV/c^2	$-\frac{1}{3}$	$\frac{1}{2}$	$-\frac{1}{2}$	$\frac{1}{3}$
top quark	t_L	172 GeV/c^2	$\frac{2}{3}$	$\frac{1}{2}$	$\frac{1}{2}$	$\frac{1}{3}$
	t_R	172 GeV/c^2	$\frac{2}{3}$	$\frac{1}{2}$	0	$\frac{4}{3}$
bottom quark	b_L	4.19 GeV/c^2	$-\frac{1}{3}$	$\frac{1}{2}$	$-\frac{1}{2}$	$\frac{1}{3}$
	b_R	4.19 GeV/c^2	$-\frac{1}{3}$	$\frac{1}{2}$	0	$\frac{4}{3}$

Table 1.2: The force-mediating particles and their attributes [8]. The charge is expressed in units of the elementary charge (e).

Name	Symbol	Mass	Charge	Spin	Force
Photon	γ	0	0	1	electromagnetic
W Boson	W^+	80.4 GeV/c^2	1	1	weak
	W^-	80.4 GeV/c^2	-1	1	weak
Z Boson	Z	91.2 GeV/c^2	0	1	weak
Gluon	g_1	0	0	1	strong
	g_2	0	0	1	strong
	g_3	0	0	1	strong
	g_4	0	0	1	strong
	g_5	0	0	1	strong
	g_6	0	0	1	strong
	g_7	0	0	1	strong
	g_8	0	0	1	strong

1.1 Today's Standard Model of Physics

The standard model of particle physics attempts to explain the behavior of the most fundamental particles in nature and how they interact with each other. Over the past two centuries, we have discovered what we today believe to be the most fundamental building blocks of nature. Figure 1.1 shows a summary of these particles in table form.

The matter particles consist of leptons, neutrinos, and quarks. For each of the three types of leptons, the electron (e^-), the muon (μ^-) and the tau (τ^-), there is a corresponding neutrino, the electron neutrino (ν_e), the muon neutrino (ν_μ) and the tau neutrino (ν_τ). The six quarks include the up (u), down (d), charm (c), strange (s), top (t), and bottom (b) quarks. These particles are only half of the fundamental particles because we must also consider the antiparticles. The antimatter particles are the positron (e^+), the antimuon (μ^+), the antitau (τ^+), the electron antineutrino ($\bar{\nu_e}$), the muon antineutrino ($\bar{\nu_\mu}$), the tau antineutrino ($\bar{\nu_\tau}$), and the six antiquarks:

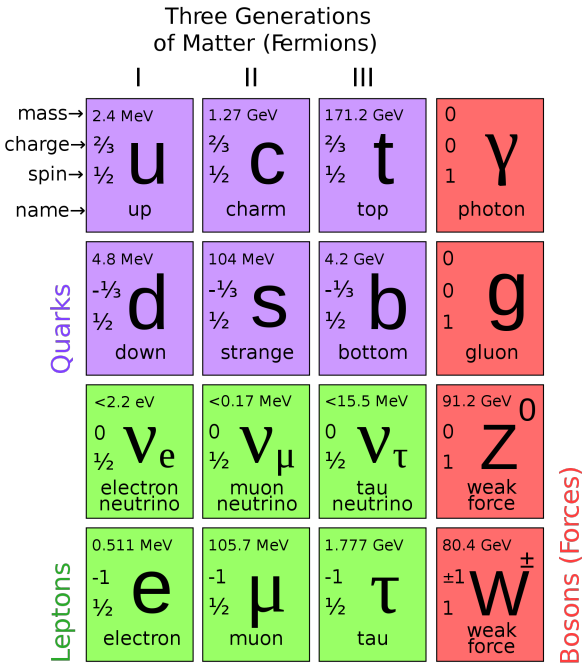

Figure 1.1: The table of fundamental particles.

antiup ($\bar{u}$), antidown ($\bar{d}$), anticharm ($\bar{c}$), antistrange ($\bar{s}$), antitop ($\bar{t}$), and antibottom ($\bar{b}$). In order to get the quantum numbers of the antiparticles, one reverses all of the additive quantum numbers, such as charge (q), handedness, weak isospin (I_3), and hypercharge (Y) [7]. One should also note that all matter particles have spin $\frac{1}{2}$ and are therefore fermions. In the next section we will see that this means that all matter particles can be represented by Dirac spinors, which are the wave functions of the Dirac equation.

A theory of fundamental particles must also provide a way for the matter particles to interact with each other. There are three forces that the standard model can describe in a unified way: the electromagnetic, the weak, and the strong force. Each one of those forces is mediated by one or more particles. When we describe a particle we need to know all of its properties before we can predict its behavior. In quantum mechanics and quantum field theory these properties are encoded as quantum numbers, like the charge or spin. Some of these quantum numbers are

closely related to a force and how much that force acts on the particle, so if one of these quantum numbers happens to be zero then the particle is "invisible" to that force.

This becomes clearer by talking about each force more concretely. The most familiar force is the electromagnetic force because it does not only act in the quantum world, but is also a macroscopic phenomenon. The electromagnetic force is mediated by the photon (γ) and is related to the charge (q) of the particle. For example, when two charged particles come close to each other, they exchange virtual photons, which transmit the electromagnetic force between them. On the other hand, the electromagnetic force does not act on a neutrino with zero charge. The next force is the weak force, which is mediated by three particles: the W^+, the W^-, and the Z^0, and it is related to a particle's weak isospin (I_3). It turns out that only the left-handed fundamental particles carry non-zero isospins. Finally, the strong force is mediated by eight gluons (g_1, g_2, g_3, g_4, g_5, g_6, g_7, and g_8) and is related to the combination of three quantum numbers, redness (R), greenness (G), and blueness (B), which each can take on a value of $+1$ for quarks and -1 for antiquarks. Of course, 0 is also allowed. All of these twelve force-mediating particles have spin 1 and are therefore bosons.

The above described standard model of particle physics has been immensely successful in its predictive power and has been tested to many orders of magnitude. Let us now look in more detail at the formalism that is used for standard model calculations, known as quantum field theory.

1.2 Quantum Field Theory

The laws of quantum mechanics cannot be derived from classical principles; they can at most be made plausible. We have to use non-classical ideas such as Planck's energy quantization, de Broglie's wave-particle duality, and especially the

concept of representing physical quantities with operators. When we combine the concepts of quantum mechanics and special relativity, we get two types of wave equations: the Klein-Gordon equation for spin-0 particles and the Dirac equation for spin-$\frac{1}{2}$ particles. The latter is used to describe all of the fundamental matter particles. Both wave equations reduce to the Schrödinger equation in the non-relativistic limit [7].

We will assume the fundamental principles of quantum field theory (QFT). The following sections are based on the excellent explanations of P. Schmüser's *Feynman-Graphen und Eichtheorien für Experimentalphysiker* (Feynman Graphs and Gauge Theories for Experimental Physicists), which contains more detail than is given here. Let us start by listing our assumptions and the necessary fundamental concepts from QFT:

(1) It is conventional to set the speed of light and the Planck constant to unity, so $c = 1$ and $\hbar = 1$.

(2) We will work in four space-time dimensions with the following metric:

$$g_{\mu\nu} = \begin{pmatrix} 1 & 0 & 0 & 0 \\ 0 & -1 & 0 & 0 \\ 0 & 0 & -1 & 0 \\ 0 & 0 & 0 & -1 \end{pmatrix} \tag{1.1}$$

(3) We will follow the Einstein summation convention in which two common indices are contracted and summed over. For example:

$$\phi_\mu \phi^\mu = \sum_{\mu=0}^{3} \phi_\mu \phi^\mu = \phi_0 \phi^0 + \phi_1 \phi^1 + \phi_2 \phi^2 + \phi_3 \phi^3 \tag{1.2}$$

(4) The four γ matrices are given by:

$$\gamma^0 = \begin{pmatrix} 1 & 0 & 0 & 0 \\ 0 & 1 & 0 & 0 \\ 0 & 0 & -1 & 0 \\ 0 & 0 & 0 & -1 \end{pmatrix} \quad \gamma^1 = \begin{pmatrix} 0 & 0 & 0 & 1 \\ 0 & 0 & 1 & 0 \\ 0 & -1 & 0 & 0 \\ -1 & 0 & 0 & 0 \end{pmatrix}$$

$$\gamma^2 = \begin{pmatrix} 0 & 0 & 0 & -i \\ 0 & 0 & i & 0 \\ 0 & i & 0 & 0 \\ -i & 0 & 0 & 0 \end{pmatrix} \quad \gamma^3 = \begin{pmatrix} 0 & 0 & 1 & 0 \\ 0 & 0 & 0 & -1 \\ -1 & 0 & 0 & 0 \\ 0 & 1 & 0 & 0 \end{pmatrix} \tag{1.3}$$

(5) The Dirac field equation is given by:

$$(i\gamma^\mu \partial_\mu - m)\psi(x) = 0 \tag{1.4}$$

where x is the position of the particle, m is the mass of the particle, $\psi(x)$ is the field of the particle in the form of a Dirac spinor (i.e. a 4-component column vector), and γ^μ are the four γ matrices shown above. Note that $\gamma^\mu \partial_\mu$ is not a dot product, but instead shorthand for $\gamma^0\partial_0 + \gamma^1\partial_1 + \gamma^2\partial_2 + \gamma^3\partial_3$.

(6) In QFT, fields create and annihilate particles. For example, when a field is operated on the vacuum, it gives rise to particles.

(7) Consider a field ϕ. If the Lagrangian density contains a squared term in ϕ then this field describes a massive particle with mass proportional to the coefficient. This is because a squared field term describes the coupling of that field to itself, and its coefficient gives the strength of that coupling, which is related to its mass. For example, the following Lagrangian describes a massive field ϕ with particle mass m:

$$\mathcal{L} = ... + \frac{1}{2}m^2\phi_\nu\phi^\nu + ... \tag{1.5}$$

1.3 Gauge Symmetries

Gauge symmetries can be best understood through a few concrete examples. First, let us remember the gauge invariance of the electromagnetic theory. We can construct the electric field ($\mathbf{E}$) and magnetic field ($\mathbf{B}$) using the electric potential (ϕ) and the magnetic vector potential ($\mathbf{A}$). Recall that the bold-faced symbols imply 3-vectors, so let us form the electromagnetic potential as a 4-vector as follows:

$$A^\mu = (\phi, \mathbf{A}) \tag{1.6}$$

We can calculate the electric and magnetic fields from A^μ. If we transform the potentials with a scalar function (χ) of the coordinates in the following way:

$$A^\mu \rightarrow A'^\mu = A^\mu - \partial^\mu \chi \tag{1.7}$$

the electric and magnetic fields are left invariant. This is an example of a gauge transformation: a transformation of the potential that leaves the fields, and therefore the physics, of the problem unaltered. We will now look at a gauge transformation in quantum field theory. Let us consider the Dirac equation of a free particle with charge q:

$$(i\gamma^\mu \partial_\mu - m)\psi(x) = 0 \tag{1.8}$$

and perform a local phase transformation of the field using the phase function $q\chi(x) = q\chi(t, \mathbf{x})$:

$$\psi'(x) = e^{iq\chi(x)}\psi(x) \tag{1.9}$$

We will now determine the form of $\psi'(x)$ by operating with $(i\gamma^\mu \partial_\mu - m)$ on both sides of Eq. (1.9):

$$\begin{aligned}
(i\gamma^\mu \partial_\mu - m)\psi'(x) &= (i\gamma^\mu \partial_\mu - m)e^{iq\chi(x)}\psi(x) \\
&= e^{iq\chi(x)}(i\gamma^\mu \partial_\mu - m)\psi(x) - q\gamma^\mu(\partial_\mu \chi(x))\psi'(x) \\
&= 0 - q\gamma^\mu(\partial_\mu \chi(x))\psi'(x) \\
&= q\gamma^\mu A'_\mu \psi'(x)
\end{aligned} \tag{1.10}$$

where we defined $A'_\mu = -\partial_\mu \chi(x)$. The first term is zero because $\psi(x)$ is a solution of the Dirac equation (see Eq. (1.8)). We can now see that the locally phase-transformed Dirac equation is no longer a "free" Dirac equation of a particle in a vacuum, but instead a Dirac equation with electromagnetic field. Thus a local phase transformation does not keep the Dirac equation invariant. However, if in addition to the local phase transformation a transformation of the field is performed, the Dirac equation becomes invariant. We therefore have the gauge transformation:

$$\psi'(x) = e^{iq\chi(x)}\psi(x) \tag{1.11}$$

$$A'_\mu(x) = A_\mu(x) - \partial_\mu \chi(x) \tag{1.12}$$

The coupling between the wave function of the charged particle and the external field can be realized by substituting the covariant derivative $D_\mu = \partial_\mu + iqA_\mu$ into the Dirac equation:

$$(i\gamma^\mu D_\mu - m)\psi(x) = 0 \quad \Rightarrow \quad (i\gamma^\mu \partial_\mu - m)\psi(x) = q\gamma^\mu A_\mu \psi(x) \tag{1.13}$$

We may apply other transformations to Dirac spinors, which result in vector fields that couple to these spinors. Local transformations of the weak isospin and the weak hypercharge lead to the existence of W and Z boson fields, and local transformations of the quarks' color lead to the existence of gluon fields. The quanta of these fields are known as "gauge bosons," and were previously referred to as force-mediating particles.

Let us now turn to the masses of the gauge bosons. The gauge invariance of the electromagnetic field is related to the fact that the photons do not have mass. Let us consider the electromagnetic wave equation:

$$\Box A^\nu - \partial^\nu \partial_\mu A^\mu = j^\nu \tag{1.14}$$

where $\Box = \nabla^2 - \frac{\partial^2}{\partial t^2}$ and j^ν is the 4-current. This equation is invariant under gauge transformations of the form shown in Eq. (1.7). This gauge transformation does not

work for massive vector bosons because of the mass term in the wave equation:

$$(\Box + M^2)W^\nu - \partial^\nu \partial_\mu W^\mu = j^\nu \tag{1.15}$$

This implies that *there is no gauge invariance for massive vector particles* [7].

1.4 The Higgs Mechanism

Invariance of the Dirac equation under local phase transformations of the wave function requires the existence of an external field to which the charged particles couple. The quanta of such fields, which are known as gauge bosons, must have zero mass for the gauge invariance to hold. These were the implications of the previous section, so it would seem senseless to apply such ideas to the weak force due to its very heavy gauge bosons (see Table 1.2). However, if we assume that the weak interactions themselves have infinite extent, but are shielded by a background field, then we could formulate a gauge invariant theory of the weak force. In other words, we assume that the vector bosons are actually massless and then formulate a gauge-invariant theory based on that assumption. The vector bosons then gain mass through the background field, which is known as the Higgs field.

As a final QFT exercise, let us investigate how the Higgs field is able to endow the W and Z bosons with mass, but keep the photon massless at the same time. We recall from classical mechanics that the Lagrangian is formed in the following way:

$$L = T - V \tag{1.16}$$

where T is the kinetic energy of the particle and V is its potential energy. The Lagrangian density in QFT is formed in a similar way with a kinetic and potential term, but instead of being a function of the coordinates directly, it is a function of the fields. Also recall Eq. (1.5), which gives the form of a field's mass term.

The following derivation comes from P. Schmüser's book. The simplest Higgs structure that will give the W and Z bosons mass is to use a Higgs doublet consisting

of two complex scalar fields:

$$\Phi = \begin{pmatrix} \phi^+ \\ \phi^0 \end{pmatrix} \tag{1.17}$$

The Higgs potential is chosen such that the amplitude of the Higgs field is non-zero at its minimum potential energy or equivalently in the vacuum. The Higgs potential is therefore chosen to be:

$$V(\Phi^\dagger, \Phi) = -\mu^2 \Phi^\dagger \Phi + \lambda^2 (\Phi^\dagger \Phi)^2 \tag{1.18}$$

where μ and λ are arbitrary constants. We assume that only the neutral Higgs field has a vacuum expectation value while the charged part vanishes. The charged part must vanish; otherwise, the photon will acquire a mass, as we will see later. Also note that the vacuum expectation value of a field is at its minimum potential energy. Based on all of our assumptions, the vacuum expectation value of the Higgs field can be written as:

$$\langle \Phi_0 \rangle = \frac{1}{\sqrt{2}} \begin{pmatrix} 0 \\ v \end{pmatrix} \tag{1.19}$$

where v is a real value on the minimum contour of the Higgs potential.

The Lagrangian density of the above Higgs potential is given by:

$$\mathcal{L}_{\text{Higgs}} = (\partial^\mu \Phi)^\dagger (\partial_\mu \Phi) - V(\Phi^\dagger, \Phi) \tag{1.20}$$

and that of the electroweak gauge fields is:

$$\mathcal{L}_{\text{Electroweak}} = -\frac{1}{4} F^i_{\mu\nu} F^{i\mu\nu} - \frac{1}{4} f_{\mu\nu} f^{\mu\nu} \tag{1.21}$$

where F and f are the electroweak field tensors, which are defined in terms of the four electroweak gauge fields (three SU(2) fields $\mathbf{W} = (W^1, W^2, W^3)$ and one U(1) field B) as follows:

$$F^i_{\mu\nu} = \partial_\mu W^i_\nu - \partial_\nu W^i_\mu - g \epsilon_{ijk} W^j_\mu W^k_\nu \tag{1.22}$$

$$f_{\mu\nu} = \partial_\mu B_\nu - \partial_\nu B_\mu \tag{1.23}$$

In order to ensure the coupling between the Higgs field and the electroweak gauge boson fields, we need to subsitute the derivative in Eq. (1.20) with the electroweak covariant derivative, which is defined as:

$$D^{\mu} = \partial^{\mu} + i\frac{g}{2}\tau \cdot \mathbf{W}^{\mu} - i\frac{g'}{2}B^{\mu} \tag{1.24}$$

where g is the coupling to the weak isospin, g' is the coupling to the weak hypercharge, and $\tau = (\tau_1, \tau_2, \tau_3)$ are the three Pauli matrices. The total Lagrangian density then becomes:

$$\begin{aligned} \mathcal{L} &= \mathcal{L}_{\text{Higgs}} + \mathcal{L}_{\text{Electroweak}} \\ &= (D^{\mu}\Phi)^{\dagger}(D_{\mu}\Phi) + \mu^2(\Phi^{\dagger}\Phi) - \lambda^2(\Phi^{\dagger}\Phi)^2 - \frac{1}{4}F^{i}_{\mu\nu}F^{i\mu\nu} - \frac{1}{4}f_{\mu\nu}f^{\mu\nu} \end{aligned} \tag{1.25}$$

With the Lagrangian density in hand, let us now observe how it behaves close to the Higgs field's vacuum expectation value by perturbing Eq. (1.19) along the real axis with a small real function $\eta(x)$:

$$\Phi(x) = \frac{1}{\sqrt{2}}\begin{pmatrix} 0 \\ v + \eta(x) \end{pmatrix} \tag{1.26}$$

The reason that we do not perturb along the imaginary axis is subtle, but in short it is because such a perturbation will result in a massless Goldstone boson field. This field can then be removed by the proper gauge transformation, so that it will not show up in the final Lagrangian density. Let us now apply the covariant derivative (Eq. (1.24)) to $\Phi(x)$:

$$D_{\mu}\Phi(x) = \frac{1}{\sqrt{2}}\begin{pmatrix} 0 \\ \partial_{\mu}\eta \end{pmatrix} + \frac{ig}{2\sqrt{2}}\begin{pmatrix} (W^1_{\mu} - iW^2_{\mu})(v + \eta) \\ 0 \end{pmatrix} \tag{1.27}$$

$$+\frac{i}{2\sqrt{2}}\begin{pmatrix} 0 \\ (g'B_{\mu} - gW^3_{\mu})(v + \eta) \end{pmatrix} \tag{1.28}$$

We construct the first term in Eq. (1.25):

$$\begin{aligned}(D^\mu\Phi)^\dagger(D_\mu\Phi) &= \frac{1}{2}(\partial^\mu\eta)(\partial_\mu\eta)+\frac{g^2(v+\eta)^2}{8}|W_\mu^1-iW_\mu^2|^2 \\ &\quad +\frac{(v+\eta)^2}{8}|g'B_\mu-gW_\mu^3|^2 \\ &\approx \frac{1}{2}(\partial^\mu\eta)(\partial_\mu\eta)+\frac{g^2v^2}{8}(|W_\mu^{(+)}|^2+|W_\mu^{(-)}|^2) \\ &\quad +\frac{v^2}{8}|g'B_\mu-gW_\mu^3|^2 \end{aligned} \tag{1.29}$$

The second equation is based on ignoring terms of second and higher order in η. The Lagrange density then becomes:

$$\begin{aligned}\mathcal{L} &= \left[\frac{1}{2}(\partial^\mu\eta)(\partial_\mu\eta)-\mu^2\eta^2\right]-\frac{1}{4}F_{\mu\nu}^iF^{i\mu\nu}-\frac{1}{4}f_{\mu\nu}f^{\mu\nu} \\ &\quad +\frac{1}{2}\frac{g^2v^2}{4}(|W_\mu^{(+)}|^2+|W_\mu^{(-)}|^2)+\frac{1}{2}\frac{v^2}{4}|g'B_\mu-gW_\mu^3|^2 \end{aligned} \tag{1.30}$$

The W^3 and B fields mix together to form the electromagnetic field A and the Z field of the weak force as follows:

$$A_\mu = W_\mu^3\sin\theta_W+B_\mu\cos\theta_W \tag{1.31}$$

$$Z_\mu = W_\mu^3\cos\theta_W-B_\mu\sin\theta_W \tag{1.32}$$

where θ_W is the weak mixing angle, which is also known as the Weinberg angle. It is related to the couplings g and g' as follows:

$$\cos\theta_W=\frac{g}{\sqrt{g^2+g'^2}},\quad \sin\theta_W=\frac{g'}{\sqrt{g^2+g'^2}} \tag{1.33}$$

The last term in Eq. (1.30) is of the form $g'B_\mu-gW_\mu^3$, which is parallel to the Z field, so we can substitute one for the other. However, we note that there is no additive B and W^3 component, so the Lagrangian contains no mass term for the electromagnetic field.

The final Lagrange density with the Z substitution becomes:

$$\begin{aligned}\mathcal{L} &= \left[\frac{1}{2}(\partial^\mu\eta)(\partial_\mu\eta)-\mu^2\eta^2\right]-\frac{1}{4}F_{\mu\nu}^iF^{i\mu\nu}-\frac{1}{4}f_{\mu\nu}f^{\mu\nu} \\ &\quad +\frac{1}{2}\frac{g^2v^2}{4}(|W_\mu^{(+)}|^2+|W_\mu^{(-)}|^2)+\frac{1}{2}\frac{g^2v^2}{4\cos^2\theta_W}|Z_\mu|^2 \end{aligned} \tag{1.34}$$

Based on Eq. (1.5), we can now extract the masses from Eq. (1.34):

$$M_{\text{Higgs}} = \sqrt{2}\mu \tag{1.35}$$

$$M_W = \frac{gv}{2} \tag{1.36}$$

$$M_Z = \frac{gv}{2\cos\theta_W} \tag{1.37}$$

$$M_\gamma = 0 \tag{1.38}$$

The last equation is based on the previous observation that there is no electromagnetic field term in Eq. (1.34). A similar process can be used to generate masses for the matter fermions. This is necessary because for the electroweak gauge invariance to hold, the leptons must have the same masses as their partner neutrinos, which are zero, so the leptons gain their masses through the Higgs mechanism. The strong gauge invariance requires that all of the quarks have the same mass, which is not the case according to experimental measurements (see Table 1.1), so we also must use the Higgs mechanism to give them different masses [7].

1.5 The Higgs Boson

The previous sections have laid the theoretical foundation for why the Higgs mechanism is essential to the standard model. In fact, P. Schmüser says in his book that the standard model stands or falls with the Higgs mechanism [7]. Equation (1.35) gives the mass of the Higgs boson as a function of μ, which is one of the arbitrary coefficients in the Higgs potential (see Eq. (1.18)). This means that there is no prediction of the Higgs mass from the formalism, so it is necessary to scan all possible masses for its existence. At the lower end of the mass spectrum, the Large Electron Positron collider (LEP) has excluded the existence of a Higgs boson below a Higgs mass of 114.4 GeV/c^2 at the 95% confidence interval [1]. Figure 1.2 shows the LEP exclusion plot. The Tevatron collaborations (CDF and DØ) have

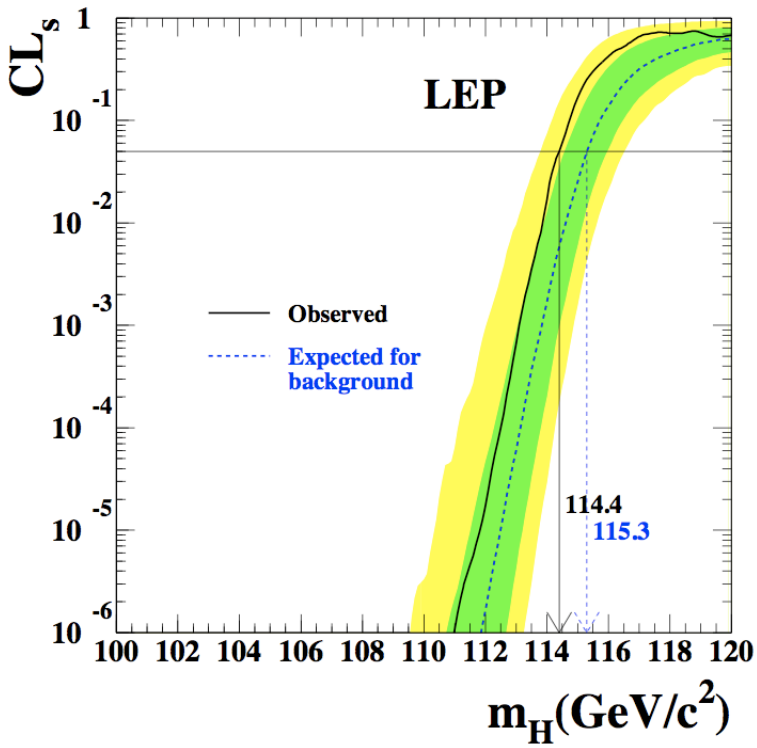

Figure 1.2: The confidence level ratio $CL_s = CL_{s+b}/CL_b$ for the signal plus background hypothesis. The solid line indicates the observed data and the dashed line indicates the median of the background expectations. The yellow band around the expected median corresponds to the 68% probability band and the green band to the 95% probability band. The horizontal line indicates $CL_s = 0.05$, so its intersection with the observed curve defines the 95% confidence level lower bound on the mass of the Standard Model Higgs boson [1].

also excluded a Higgs mass region from 158 to 175 GeV/c^2 [2]. Figure 1.3 shows the Tevatron exclusion plot.

While the theory does not provide a value for the Higgs mass, it provides indirect ways to calculate probable Higgs mass windows based on radiative corrections, which in turn are based on precision mass measurements of the W boson and top quark. The theory currently favors a Higgs boson with a mass less than 185 GeV/c^2. Figure 1.4 shows the region in which the Higgs boson could exist.

Now that we know which Higgs masses are excluded and which ones are probable, the question becomes how to search in the unknown mass regions. First, we need to consider the production and decay modes of the Higgs boson. Figure 1.5

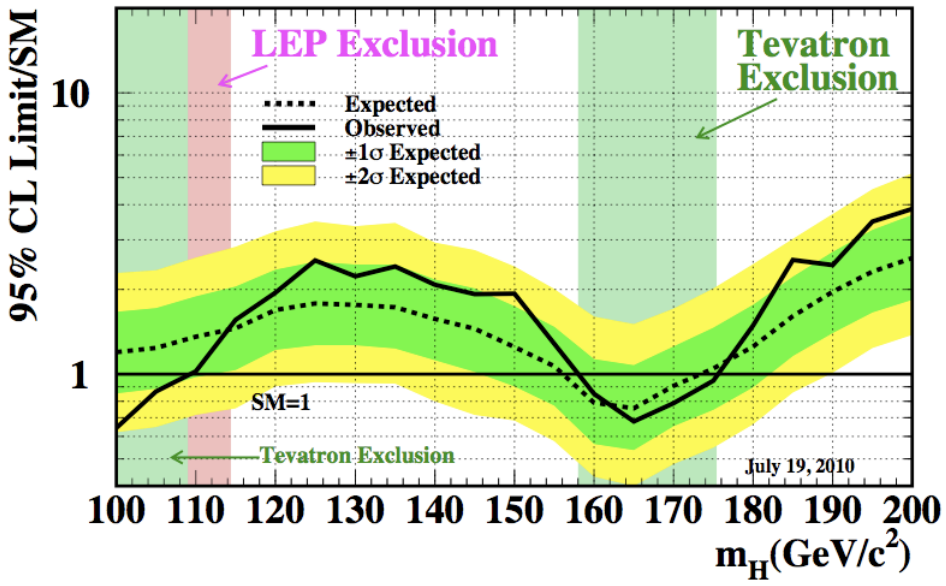

Figure 1.3: The latest combined search for the standard model Higgs boson coming from the CDF and DØ collaborations. The teal shading shows the mass ranges excluded by the Tevatron. The high mass exclusion region is $158 < m_H < 175$ GeV/c^2 [2].

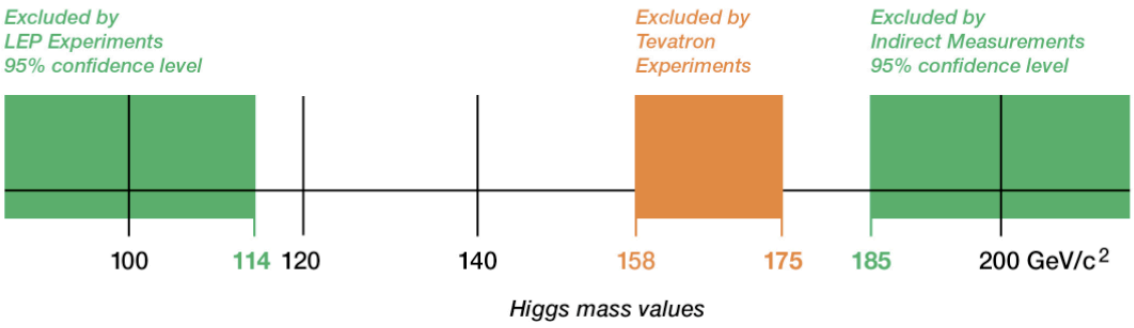

Figure 1.4: The allowed Higgs boson mass region. The orange Tevatron exclusion band is also at a 95% confidence level.

shows the cross sections of the Higgs production modes at the Tevatron for different mass values. These are the different ways in which we can produce a Higgs boson at the center of our detector. Figures 1.6 and 1.7 show the predicted decay modes of the Higgs boson for different masses. The total cross section that we observe for a given production and decay mode is the product of the production cross section and the decay branching ratio. In the high mass region, CDF collaborators consider gluon fusion ($gg \rightarrow H$), the largest cross section production mode, together with Higgs decay into two W bosons ($H \rightarrow WW$). This yields the largest number of Higgs events for a Higgs mass above approximately 135 GeV/c^2. Below that mass value, the maximal number of Higgs events would be reached by considering direct Higgs production through gluon fusion together with Higgs decay into a bottom and antibottom pair. However, the problem with this search channel is that the processes in which a quark/antiquark pair is produced are overwhelmingly numerous, so the Higgs signal would be very difficult to separate out. For this reason, we elect to search for Higgs production in association with a W boson ($qq \rightarrow WH$) instead of gluon fusion. That way, our event topology contains a lepton from the decay of the W, which we can easily identify. This means that the decay topology for associated Higgs production together with Higgs decay to a bottom/antibottom quark pair consists of a lepton and neutrino from the W decay and the bottom and antibottom quark from the Higgs decay.

The Feynman diagram for this decay mode is shown in Fig. 1.8. Table 1.3 shows the cross sections and branching ratios that we use for this analysis.

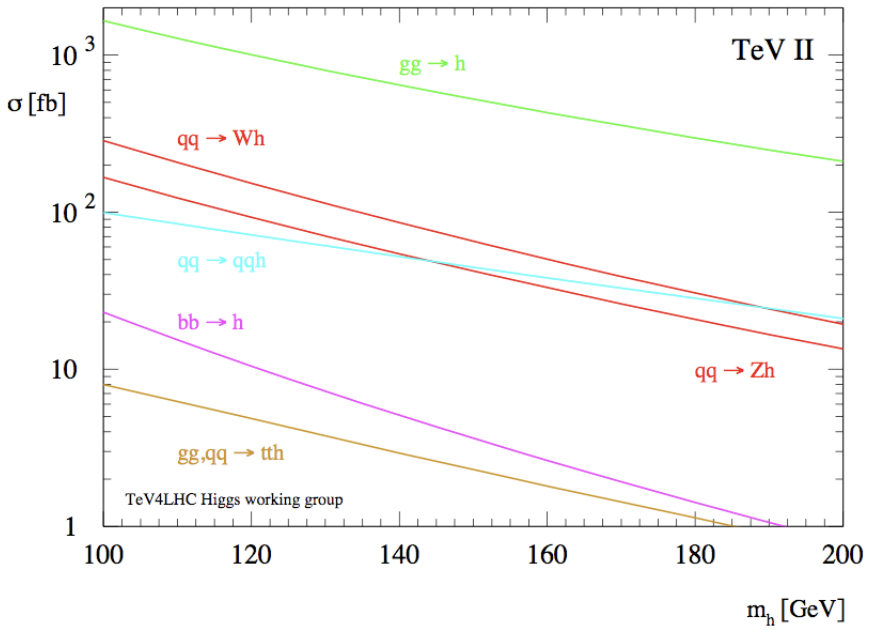

Figure 1.5: SM Higgs Production. This summary of standard model Higgs production modes was provided by the Tev4LHC Higgs working group. Each line shows the expected cross section for each Higgs production mode as a function of its mass at the Tevatron [3].

Table 1.3: Higgs production cross sections and branching ratios of the WH process [4, 9].

Higgs Mass (GeV/c^2)	Cross Section (fb) $\sigma(p\bar{p} \to W^{\pm}H)$	WH Branching Ratio (%) BR($H \to b\bar{b}$)
100	291.9	80.33
105	248.4	78.57
110	212.0	75.90
115	181.9	71.95
120	156.4	66.49
125	135.1	59.48
130	116.9	51.18
135	101.5	42.15
140	88.3	33.04
145	77.0	24.45
150	67.3	16.71

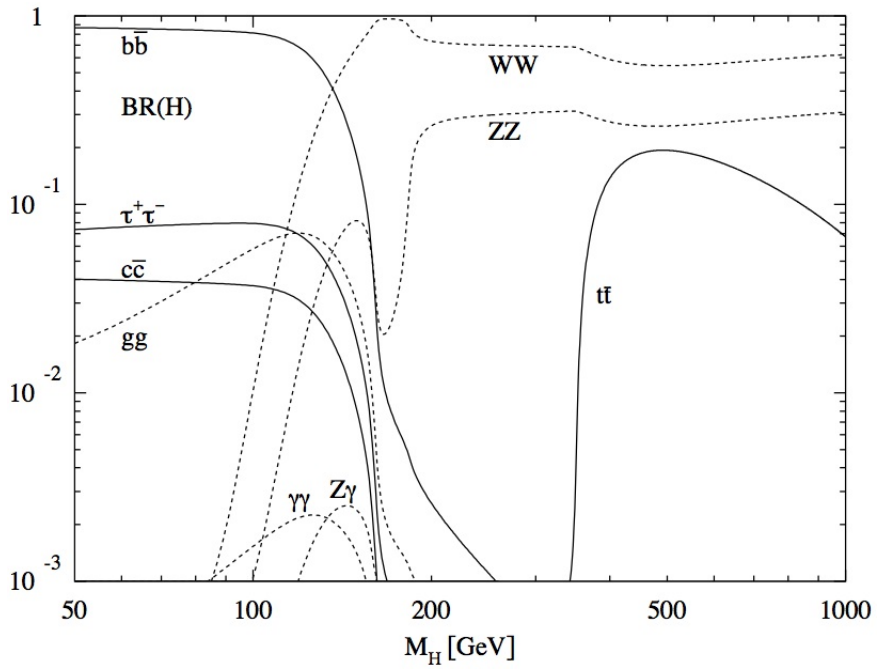

Figure 1.6: The branching ratios of the Higgs boson as a function of its mass (M_H) in the region $50 < m_H < 1000$ GeV/c^2. Each line corresponds to a predicted decay mode of the Higgs boson. Note that the sum of all decay modes is unity. The numbers in the above plot were generated with HDECAY, which calculates branching ratios of the standard model Higgs boson based on the current theoretical knowledge [4].

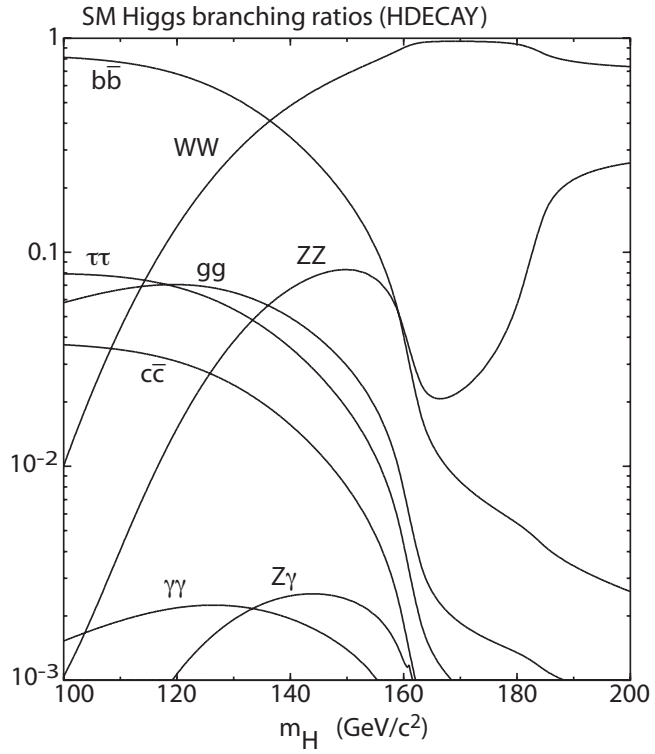

Figure 1.7: A magnified portion of Fig. 1.6 in the region of $100 < m_H < 200$ GeV/c^2. It focuses on the branching ratios with wich we are concerned.

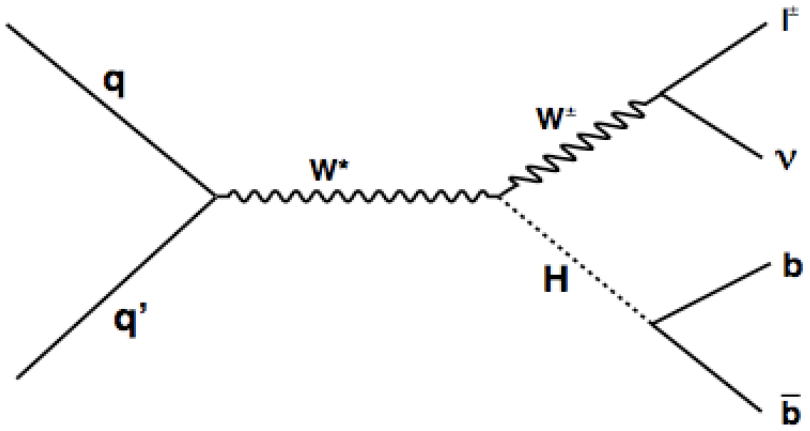

Figure 1.8: The Feynman diagram for associated Higgs production with a W boson (WH).

CHAPTER TWO

The Experiment

2.1 Introduction

In this chapter we describe the physical process by which experimentally significant events are produced and detected. We first explain how protons (p) and antiprotons ($\bar{p}$) are produced and accelerated at Fermilab. Once they reach an energy of 980 GeV, these particles are made to collide in our detector, the Collider Detector at Fermilab (CDF). CDF is a multi-purpose detector designed to detect the momentum, charge, energy, and many other kinematic properties of particles created in $p\bar{p}$ collisions. We describe the components of the detector and how they allow us to measure the properties of highly energetic particles. At the end of the chapter, we describe one of the CDF components in detail, the eXtremely Fast Tracker (XFT), and its monitoring software, which I designed.

2.2 Fermilab and the Tevatron

Fermilab was originally commissioned in 1967 by the United States Atomic Energy Commission under President Lyndon B. Johnson [12]. It is located in Batavia, Illinois and houses one of the world's most energetic particle colliders, the Tevatron, which has a 1 km radius. Figure 2.1 shows an aerial view of the laboratory with superimposed red lines indicating the accelerator complex. There are two significant run periods of the Tevatron, the first one is from 1992 to 1996, known as Run I, and the second one started after a short upgrade period in 2001, which is known as Run II.

The Tevatron is the final accelerator in a chain of accelerators that brings protons from rest to 980 GeV. Table 2.1 summarizes the final energies of each of the

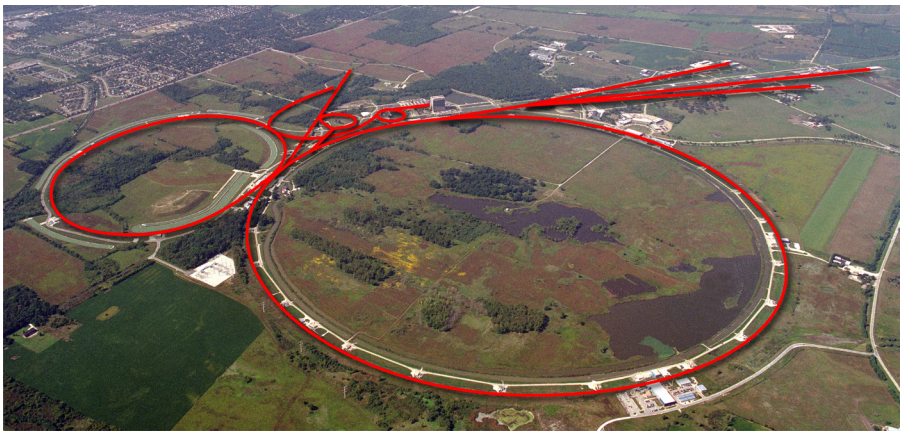

Figure 2.1: An aerial view of Fermilab with the accelerator complex highlighted in red.

accelerators. The following information regarding these accelerators can be found in greater detail in the Fermilab Operation Department's rookie books [13, 14]. Figure 2.2 shows all of the individual components of Fermilab's accelerator chain.

Table 2.1: The energy to which the protons are accelerated in each accelerator.

Accelerator	Energy (MeV)
Cockcroft-Walton	0.75
Linac	400
Booster	8,000
Main Injector	150,000
Tevatron	980,000

At the beginning of this chain, a hydrogen gas bottle is introduced into the Cockcroft-Walton generator where the hydrogen atoms are enriched with additional electrons to form H^- ions. The generator dome is held at a negative potential of 750 keV with respect to the Linac or linear accelerator entrance, which is grounded. Therefore, when the H^- ions enter the Linac, they are traveling with an energy of 750 keV.

The Linac then accelerates the H^- ions to 400 MeV using a series of radio frequency (RF) cavities. Such cavities are used in all of the subsequent accelerators to accelerate the protons. An RF cavity contains an electromagnetic standing wave synchronized with the movement of the protons in such a way that the electric field is aligned in the direction of the proton's momentum when it passes through the cavity. The proton experiences a force of qE in the cavity, so its acceleration will be $\frac{qE}{m}$, where E is the magnitude of the electric field and q and m are the proton's charge and mass, respectively.

The next stage of acceleration is the Booster ring, which passes the 400 MeV H^- ions from the Linac through a stripping foil. This removes the electrons from most of the H^- ions resulting in H^+ ions, which are simply protons [14]. The particles pass through a magnetic field, which only allows protons to enter the Booster ring. The Booster ring then accelerates the protons to 8 GeV by repeatedly passing them through several RF cavities. Dipole magnets keep the protons in this ring and all of the following rings by bending their paths.

The protons' next destination is the Main Injector ring, which has several functions, including facilitating antiproton production and accelerating protons and antiprotons. To produce antiprotons, the Main Injector feeds protons into the antiproton source where they collide with a nickel alloy. The antiprotons produced in this collision are collected in the Accumulator and sent to the Recycler ring, located along the ceiling of the Main Injector ring tunnel, which moves the antiprotons in the opposite direction from the protons in the Main Injector ring.

When the recycler is loaded with antiprotons and the Main Injector is loaded with protons, the loading of the Tevatron can begin. First, the protons are accelerated from 8 GeV to 150 GeV and then transferred into the Tevatron. Then, antiprotons are transferred from the Recycler and the Accumulator into the Main Injector, accelerated from 8 GeV to 150 GeV and then transferred into the Tevatron

moving in the opposite direction as the protons. The Tevatron accepts the protons and antiprotons from the Main Injector, which counter-circulate in three trains of 12 bunches each, yielding a total of 36 proton bunches and 36 antiproton bunches. The Tevatron is a circular synchrotron accelerator with eight RF accelerating cavities. It accelerates both protons and antiprotons from 150 GeV to their final energy of 980 GeV. The Tevatron uses superconducting magnets, which must be maintained at a temperature of approximately 4 K to stay superconducting, in order to bend the high energy beam. With the aid of these magnets, the protons and antiprotons are made to collide every 396 ns at two locations on the Tevatron ring, at CDF and at DØ (another detector on the Tevatron), with a center of mass energy of $\sqrt{s} = 1.96$ TeV. The particle intensity in the CDF detector ranges between 10^{31} and 10^{33} $\frac{\text{particles}}{\text{cm}^2\ \text{s}}$. This can be converted into more convenient units of barn (b) per second, where 1 b is defined as 10^{-28} m^2, so that our instantaneous collision intensity is between 1 and 100 $\frac{\text{particles}}{\mu\text{b}\ \text{s}}$. The instantaneous collision intensity is also known as the instantaneous luminosity (L), which can be integrated to yield the luminosity acquired over time:

$$\mathcal{L} = \int L\, dt \tag{2.1}$$

High energy physicists often quantify the collected amount of data in a detector by its integrated luminosity. Fig. 2.3 shows the luminosity delivered by the Tevatron as a function of time, from which it can be seen that the 10 fb^{-1} milestone was attained only very recently.

2.3 The Detector

In this section we describe the relevant components of the CDF II detector. First, we introduce the coordinate system that we use inside the detector. Then, we introduce each component starting closest to the beam pipe and working our way outwards. The system closest to the beam pipe and $p\bar{p}$ interaction point is the

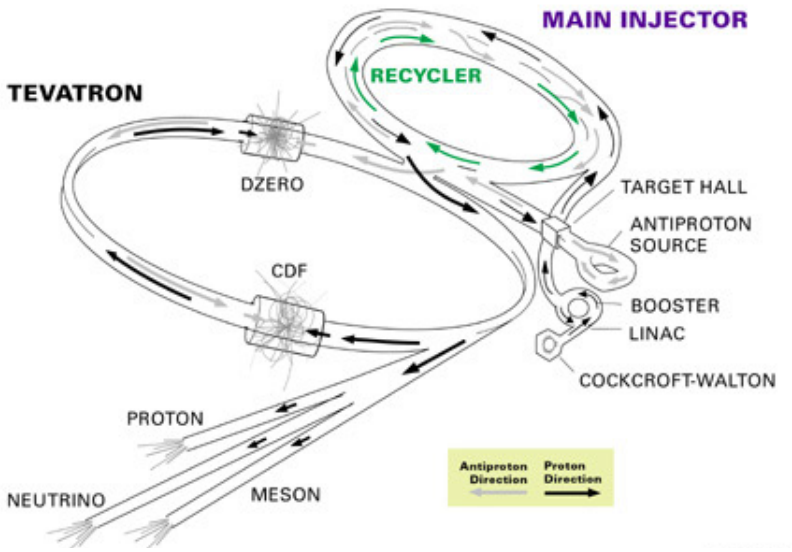

Figure 2.2: Fermilab's Accelerator Chain. Table 2.1 shows the energies of each accelerator. The dark arrows indicate the direction of the protons and the light arrows the direction of the antiprotons. The green arrows in the Recycler correspond to the direction of the antiprotons.

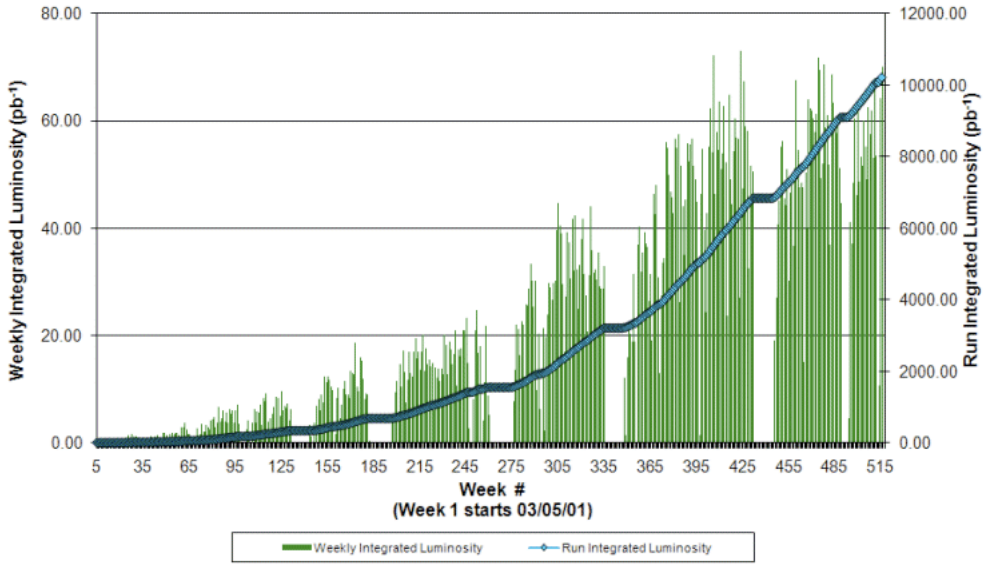

Figure 2.3: The weekly and total integrated luminosity delivered by the Tevatron for each week since the start of Run II [5].

silicon tracking detector, which is surrounded by the central outer tracker. These two systems are embedded in a 1.4 T solenoid magnet, which bends the paths of charged particles. Outside the magnet, we find the calorimeters, the electromagnetic and hadronic calorimeters, and the inner muon system. All of these systems are encased in heavy steel, which is designed to absorb most particles. The outside of the detector is lined with another muon system. Figure 2.4 is a photograph taken from the side of the detector while the silicon tracking system is being inserted. The descriptions are based on the CDF II detector technical design report [15]. The original CDF I detector design, which was used during Run I, is detailed in [16].

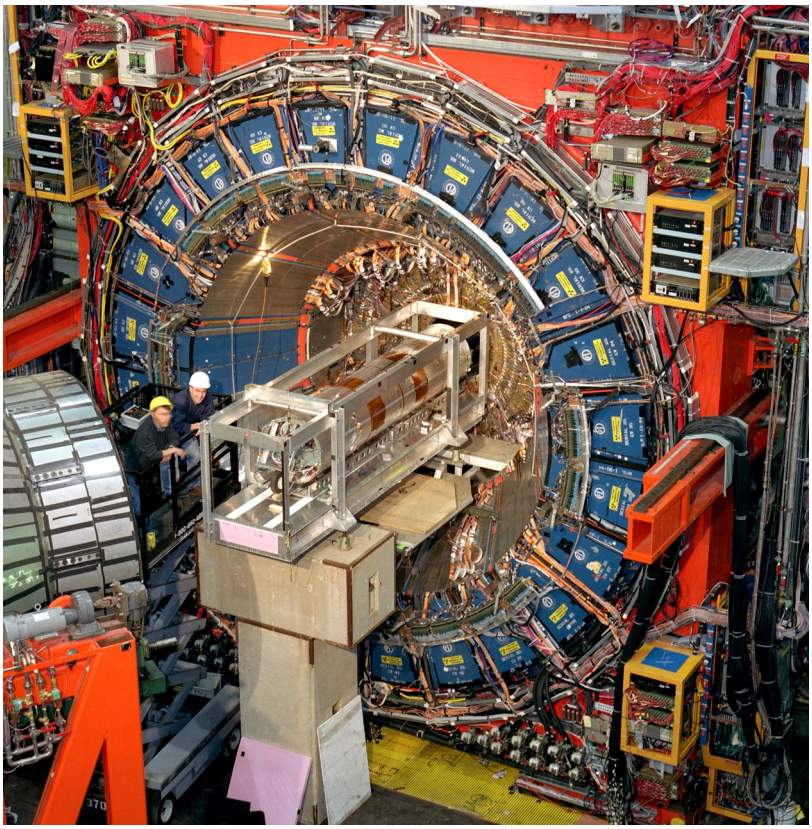

Figure 2.4: A photograph of CDF from the side as the silicon tracker is being inserted.

2.3.1 The Coordinate System

We use the coordinate system to describe the location and movement of particles in our detector. The CDF II detector geometry is described using a cylindrical coordinate system. The z-axis follows the proton direction, and the polar angle θ is usually expressed through the pseudorapidity η. The definition of pseudorapidity is based on the standard definition of rapidity:

$$y = \frac{1}{2} \ln \left(\frac{E + p_z}{E - p_z} \right) \tag{2.2}$$

by replacing the energy by the magnitude of the momentum three-vector (p):

$$\begin{aligned} \eta &= \frac{1}{2} \ln \left(\frac{p + p_z}{p - p_z} \right) \\ &= -\ln \left(\tan \frac{\theta}{2} \right) \end{aligned} \tag{2.3}$$

The advantage of using the pseudorapidity instead of the angle θ is that $\Delta\eta$ is Lorentz invariant with respect to boosts in the z direction for massless particles, while $\Delta\theta$ is not. This is very important for us because the center of mass frame of a $p\bar{p}$ collision is different with respect to the lab frame in the z direction from collision to collision. The tradeoff in using the pseudorapidity instead of the rapidity is that changes in it are not Lorentz invariant for massive particles. However, since the mass of most particles is much smaller than the energies inside of our detector, the pseudorapidity is a good approximation. The detector is approximately symmetric about $\eta = 0$ and in the azimuthal angle ϕ. The transverse energy is defined as $E_T = E \sin\theta$, and the transverse momentum as $p_T = p \sin\theta$. Figure 2.5 shows a schematic view of the CDF II detector indicating the beam pipe, which is the z-axis of our coordinate system. We now describe the individual components of Fig. 2.5.

2.3.2 The Silicon Tracker

The silicon tracker is closest to the beam pipe and $p\bar{p}$ interaction point; its location is shown in Fig. 2.5. The silicon tracker consists of three cylindrical sub-

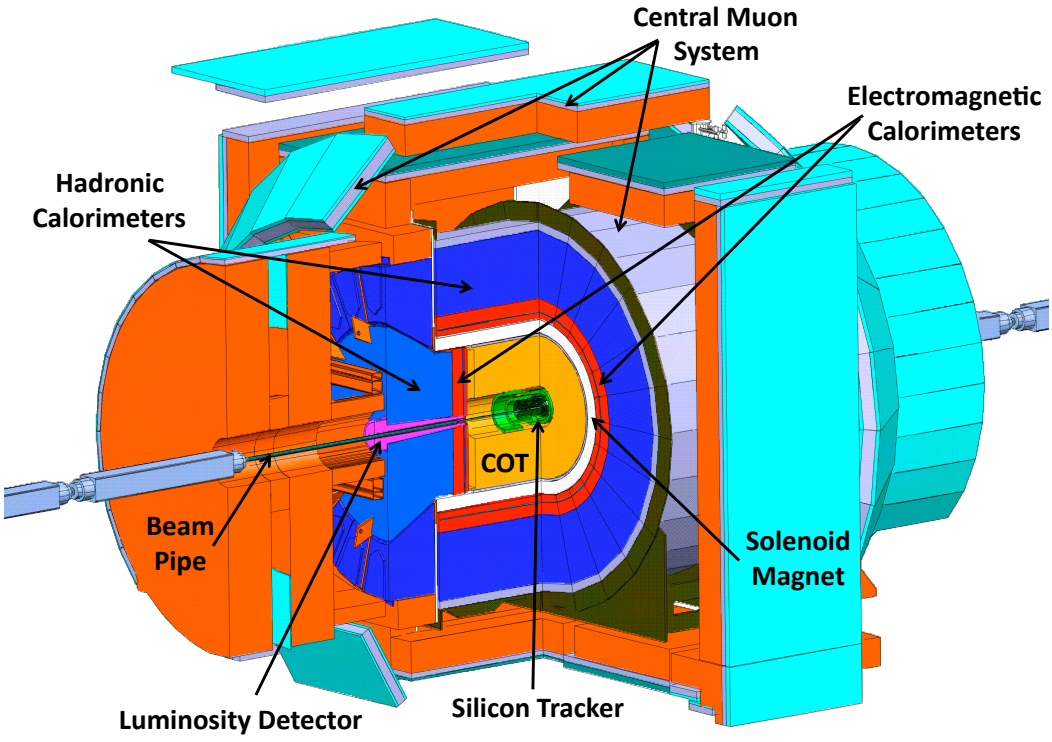

Figure 2.5: A schematic view of the CDF II detector with a section removed to reveal the tracking systems. The silicon tracker (Sec. 2.3.2) is shown in green and is closest to the beam pipe. The COT (Sec. 2.3.3) is shown in light orange. The solenoid magnet is shown in white. The electromagnetic calorimeters (Sec. 2.3.4.1) are shown in red, and the hadronic calorimeters (Sec. 2.3.4.2) are shown in dark blue. The muon systems (Sec. 2.3.5) are indicated in grey. The luminosity detector (Sec. 2.3.6) is shown in magenta.

systems, which are, in order from the center, Layer 00, the Silicon Vertex detector (SVX II), and the Intermediate Silicon Layers (ISL) [6]. Figure 2.6 shows all three systems from the end view.

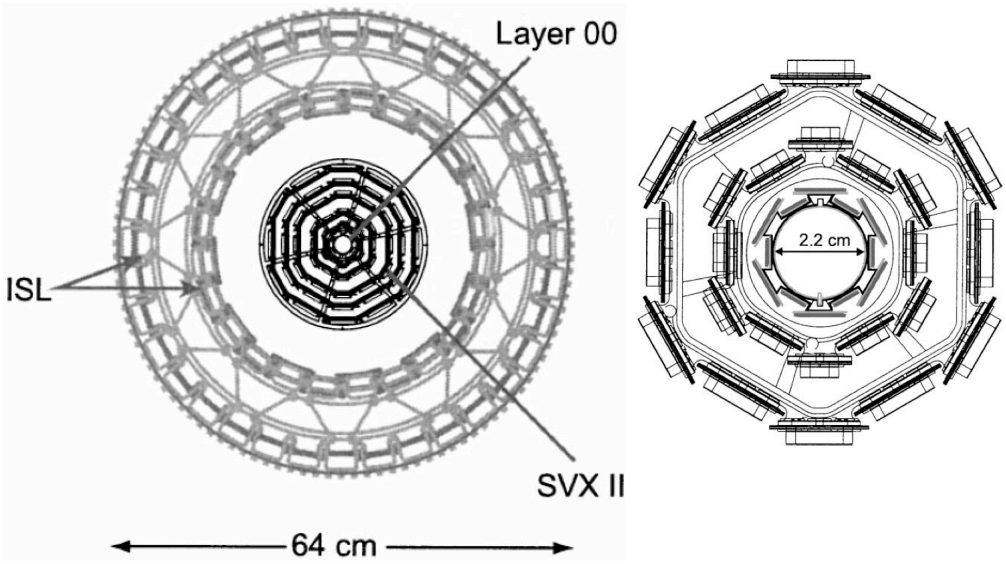

Figure 2.6: The left image shows an end view of the entire silicon tracker. The right image is a magnified portion of the center of the silicon tracker showing Layer 00 together with the first two layers of the SVX II detector [6].

As the name suggests, the silicon detector uses silicon chips for detection. When an energetic charged particle traverses one of these chips, it ionizes the silicon, which produces an electron and a positively charged ion, which is an electron/hole pair in the semiconductor. The silicon chips are set up similarly to a diode with a p-n junction across which we put a reverse potential, so there is no current flow. However, when one of these electron/hole pairs is produced, a small current flows, which we amplify and then read out as a signal. These chips are mounted on boards which are then arranged in layers around the beam pipe as is shown in Fig. 2.6. The silicon tracker provides the highest resolution tracking in our detector.

2.3.3 Central Outer Tracker

Surrounding the silicon tracker is the Central Outer Tracker (COT), which is shown in light orange in Fig. 2.5. The COT is a wire chamber consisting of 8 superlayers, each containing potential wire layers and 12 sense wire layers across which a voltage is applied (see top right of Fig. 2.7). The entire chamber is immersed in a gas which serves as the ionization medium. When an energetic charged particle traverses the gas, it ionizes several gas molecules, forming electrons and positively charged ions, which drift to the closest wires and create a current through a sense/field wire pair. We amplify that current and then read it out for each wire pair. Detectors that use this technique are also known as drift chambers. The individual wire positions are then used to reconstruct the tracks of the particles. The COT has two types of wires, axial and stereo. The axial wires are parallel to the beam axis (z-axis), and the stereo wires are tilted relative to the beam axis, so we can derive three-dimensional information from the combination of both types of wires. Figure 2.7 shows the organization of the wires into eight superlayers, four containing axial wires and four containing stereo wires.

The particle tracks provide the trajectory of each particle as it traverses our detector. Since the COT and silicon detector are immersed in a 1.4 T magnetic field, we can calculate a particle's momentum based on the curvature of its trajectory.

2.3.4 Calorimeters

At CDF, we use two different kinds of calorimeters to determine the energy of particles. We make use of different particles' penetration depths into lead and steel to differentiate them. All of our calorimeters employ a design of alternating scintillator and absorber plates. The idea is that the particles lose energy as they interact with the absorber material, so the more energetic a particle is the more layers it traverses before it is completely absorbed. The scintillating material gives

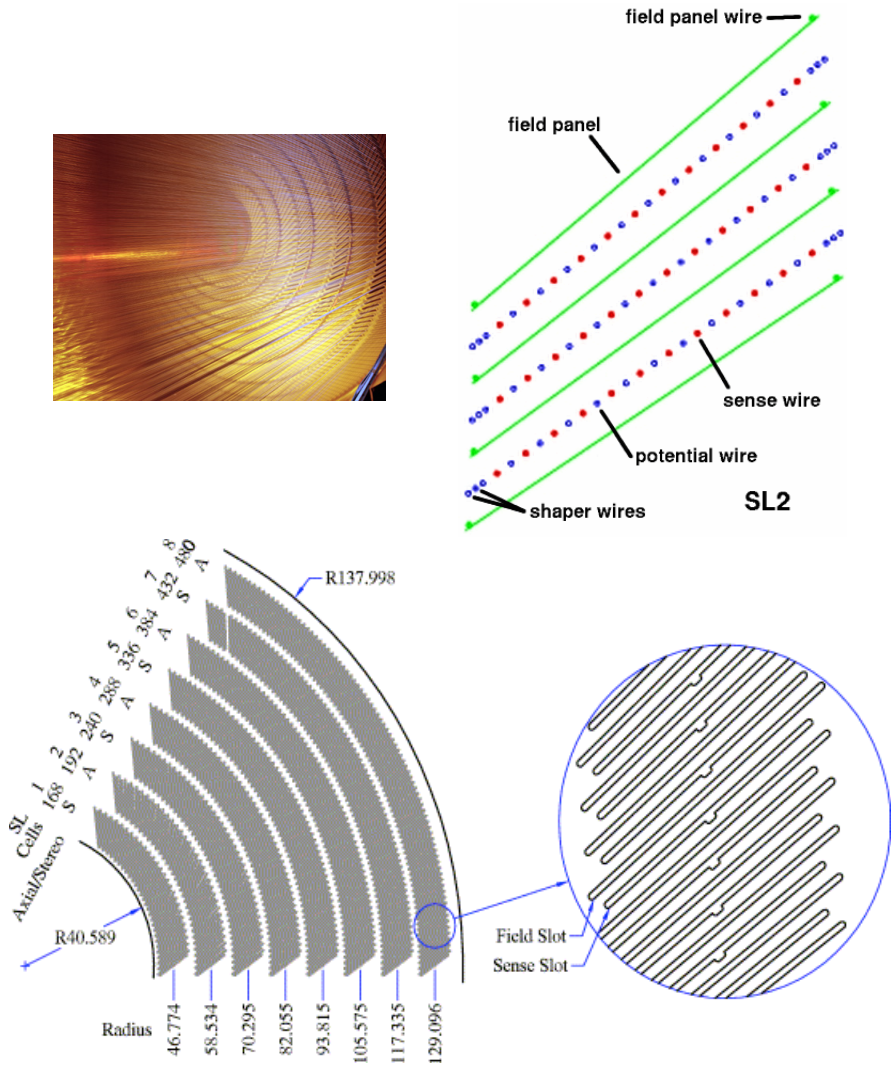

Figure 2.7: A picture of the inside of the COT showing the wires (top left), a schematic of the wire arrangement inside three cells of one superlayer (top right), and a schematic end view of a section of the COT (bottom). The bottom schematic shows how the wires are organized into superlayers. The number of cells for each superlayer is indicated, as well as what kind of wires are contained in each superlayer, axial (A) or stereo (S). A cell corresponds to 12 sense wires, which are arranged in the way shown in the schematic on the top right. The central radii of all superlayers in the bottom schematic are indicated in units of cm.

off light when an ionizing particle traverses it, so the more scintillating layers are traversed by a particle, the larger its energy. The light is read out by photomultiplier tubes and translated into an electric signal. Each calorimeter is organized into wedges. The central wedges are 15 degrees in azimuth by approximately 0.1 in pseudorapidity. Each wedge is read out by two photomultiplier tubes. The two types of calorimeters in our detector are the electromagnetic and the hadronic calorimeters. A very detailed description of both types of calorimeters can be found in [17].

2.3.4.1. *Electromagnetic Calorimeters* The electromagnetic calorimeter uses lead as the absorbing material and is calibrated to identify electrons and photons. In this analysis we use two electromagnetic calorimeters to identify electrons, the central electromagnetic calorimeter (CEM) and the plug electromagnetic calorimeter (PEM). Table 2.2 gives the η ranges of these two calorimeters. In Fig. 2.5, the electromagnetic calorimeters are indicated in red.

Table 2.2: η ranges for the two electromagnetic calorimeters. These ranges also define the central and plug regions of the detector.

Electromagnetic Calorimeter	Range
CEM	$0.0 < \|\eta\| < 1.1$
PEM	$1.1 < \|\eta\| < 3.6$

The electromagnetic calorimeters contain two additional detectors, the preradiator and the electromagnetic shower chamber. They exist in the central and plug region under the following names: central and plug preradiator (CPR and PPR) and central and plug electromagnetic shower system (CES and PES). The preradiator is used to discriminate electrons from photons. The electromagnetic shower system is mounted at the maximum shower depth of electromagnetic showers and allows us to measure the shower profile.

2.3.4.2. *Hadronic Calorimeters* The hadronic calorimeters use steel as the absorber material and are calibrated to detect hadronic particles. In this analysis, we use these calorimeters to identify energies of quark fragmentation and hadronization. These particles have a larger penetration depth than electromagnetic showers, so we can use the hadronic calorimeters to differentiate them. In this analysis, we make use of three hadronic calorimeters, the central (CHA), wall (WHA), and plug (PHA) hadronic calorimeters. They are indicated in blue in Fig. 2.5. Table 2.3 gives the η ranges of the hadronic calorimeters.

Table 2.3: η ranges for the hadronic calorimeters.

Hadronic Calorimeter	Range
CHA	$0.0 < \|\eta\| < 0.9$
WHA	$0.8 < \|\eta\| < 1.2$
PHA	$1.2 < \|\eta\| < 3.6$

2.3.5 Muon System

The muon system is used to identify muons based on the idea that most non-muon particles are absorbed by other detector components or the steel absorber before they reach the muon system. The muon system consists of small individual drift chambers, each working on the same principle as the COT. When these chambers detect a particle, we call it a muon stub. The muon stubs are then used together with the particle's track to identify a muon.

The three muon systems that we use in this analysis are shown in Fig. 2.5 and are known as the central muon system (CMU), the central muon upgrade (CMP), and the central muon extension (CMX). The CMU is mounted outside of the central calorimeters, the CMP is mounted outside of the steel absorber, and the CMX is mounted behind the wall hadronic calorimeter. The η ranges for all three systems

are shown in Table 2.4. Since the CMU and CMP systems cover the same η range, we designate them together as one system called CMUP.

Table 2.4: η ranges for the three muon systems.

Muon System	Range
CMU	$0.0 < \|\eta\| < 0.6$
CMP	$0.0 < \|\eta\| < 0.6$
CMX	$0.6 < \|\eta\| < 1.0$

2.3.6 Luminosity Detector

To measure instantaneous luminosity, we use two gaseous Cherenkov counters located between the plug system and the beam pipe at very shallow angles to the beam pipe. One counter is mounted in the proton direction, and the other one in the antiproton direction. One counter is revealed in Fig 2.5 and shown in magenta. This detector is known as the Cherenkov luminosity counter (CLC). It measures the average number of inelastic $p\bar{p}$ interactions per bunch crossing (μ), which can be related to instantaneous luminosity (L) in the following way:

$$\mu \cdot f_{\mathrm{BC}} = \sigma_{\mathrm{in}} \cdot L \tag{2.4}$$

where f_{BC} is the rate of bunch crossings and σ_{in} is the cross section of inelastic $p\bar{p}$ interactions. This cross section has been measured to be approximately 60 mb at a center of mass energy of $\sqrt{s} = 1.8$ TeV [18]. We use the method outlined in [19] to extrapolate that cross section to our center of mass energy of $\sqrt{s} = 1.96$ TeV. The rate of bunch crossings, accounting for abort gaps, is 1.7 MHz, so we can determine L directly from μ.

2.4 Trigger System

With approximately 1.7 million events per second, it would be impossible to store all of the detector output for every event on disk, so we implement a triggering system that decides which events contain important physics information and are therefore recorded on disk. At CDF, we use a three-level trigger system. The first two levels use hardware on a partial subset of the data to decide which events to keep and which ones to reject. The third level uses software to run over the entire data set and make a final decision about whether or not to reject an event. This system has been designed to minimize the amount of dead time due to the trigger decision. Figure 2.8 shows a flow chart of the trigger system.

In order to get a feeling for the rate reduction of the trigger system, let us look at the trigger rates for a data recording period, specifically run 303491. The global level 1 accept rate was approximately 23 kHz, which corresponds to a rate reduction factor of approximately 70. The level 2 accept rate was approximately 500 Hz, which corresponds to a further rate reduction of approximately 50. Finally, the level 3 accept rate was approximately 100 Hz, which corresponds to a rate reduction of approximately 5. In sum, the trigger system reduced the overall event rate by a factor of approximately 17,000.

2.5 eXtremely Fast Tracker

In this section, we will take a detailed look at the XFT monitor that I designed and which is currently in operation in the CDF control room [20]. The eXtremely Fast Tracker (XFT) is part of the CDF trigger system. It reconstructs tracks in the COT at level 1 and then sends the track information to the XTRP and level 2. Since the XFT processes events at the beam crossing rate, it needs to take certain shortcuts to reconstruct the tracks within the allotted time, which is much shorter than the time that the offline system requires for detailed track reconstruction. The

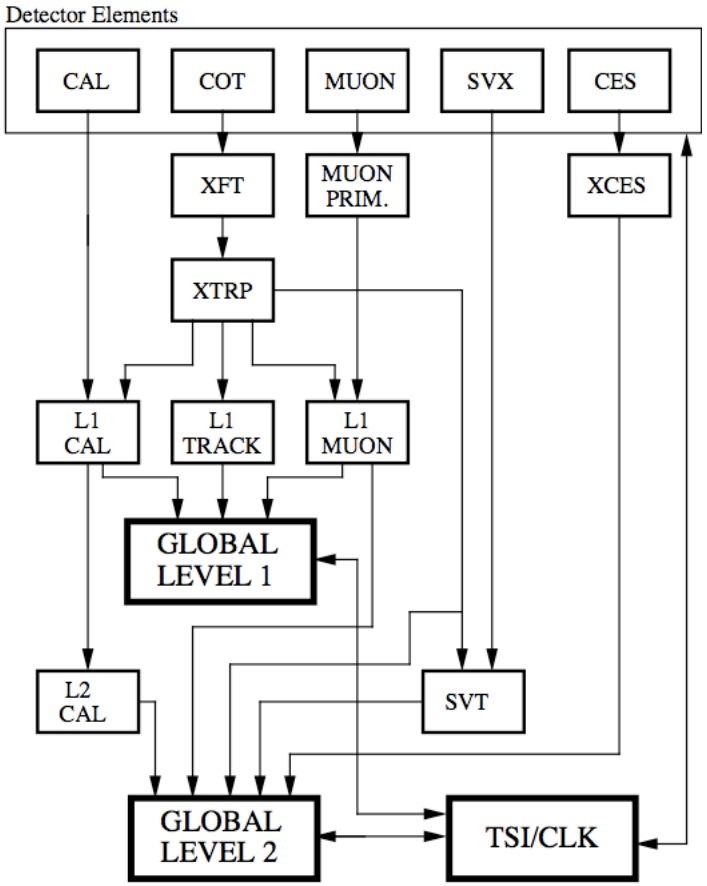

Figure 2.8: A schematic diagram showing the flow of the trigger decision. The very top shows the detector elements, which are read out by the triggering hardware and then processed to form a level one and level two decision. If the event is accepted at level two, it is forwarded to the computing farms for the level three decision.

XFT analyzes 1.8 million events per second, of which only about 140 are recorded to disk. The purpose of the XFT monitor is to compare the XFT tracks with the level 3 tracks in order to assure the proper function of the XFT trigger. A shift crew member monitors the standard plots in the control room. Once a problem is spotted, XFT experts can then consult the expert plots for a more detailed diagnosis.

2.5.1 Efficiency Definitions

The XFT monitor compares the information generated by the XFT to the level 3 information and then plots the appropriate efficiencies. These efficiencies can be used to monitor the function of each XFT component. The level 3 information is read out of the Level 3 Summary Bank and has to pass our track quality cuts (see Table 2.5). The XFT information comes from the TL2D, XFFD, and XSFD banks [21]. The XFT works in three stages: it first digitizes the hits on the wires, then constructs track segments from those hits, and finally constructs tracks from the track segments. Each of these steps is performed by a different piece of hardware within the XFT, so we monitor all three stages.

The XFT monitor uses the track parameterizations from [22] to calculate the ϕ position of the level 3 track at the desired radius. It then uses the detector geometry given in [23] to convert the ϕ position into the corresponding hit or segment position.

2.5.1.1. *Hit Finding Efficiency* The first stage is monitored with the hit finding efficiency. The XFT monitor loops over the outer 84 wirelayers (7 superlayers $\times$ 12 wirelayers/superlayer) and looks at each level 3 track. If a track comes within 0.4 cells of a wire, it increments the denominator. If the XFT finds a hit on that same wire then the numerator is also incremented. The efficiency is simply the numerator divided by the denominator.

Table 2.5: The following table gives the default requirements for a level 3 track to pass our quality requirements. Note that there are exceptions for the first two requirements: the curvature histograms require $p_T > 1.5$ GeV/c; the number of hits per superlayer can be changed in the setup file when running the XFTMonitor.

Cut Requirements
$p_T > 2$ GeV/c
at least 7 hits per superlayer in at least 7 superlayers
2 cm $< \|z_0\| <$ 60 cm
$\|z(r = 137 \text{ cm})\| < 155$ cm
track lies entirely within one half of COT

The cells corresponding to a level 3 track are calculated at each wirelayer. The XFT hit information is read out of the XFFD bank for the axial superlayers (2, 4, 6, and 8) and out of the XSFD bank for the stereo superlayers (3, 5, and 7). Note that the XFT only uses information from superlayers 2 through 8. Superlayer 1 is not used because its closeness to the beam pipe causes the wire occupancy to be too high to be useful for track reconstruction.

2.5.1.2. *Segment Finding Efficiency* The second stage is monitored with the segment finding efficiency. The XFT monitor loops over the outer seven superlayers and increments the denominator for each level 3 track. It then calculates the closest segment to the track within the superlayer. Finally, it checks whether the XFT recorded a segment in the same superlayer close to the level 3 segment. If the angular separation between those two segments contains less than or equal to 2 segments then the numerator is incremented. The efficiency is the numerator divided by the denominator.

The segments corresponding to a level 3 track are calculated at the middle of each superlayer. The XFT segment information is read out of the XFFD bank

for the axial superlayers (2, 4, 6, and 8) and out of the XSFD bank for the stereo superlayers (3, 5, and 7).

2.5.1.3. *Track Finding Efficiency* The last stage of the XFT is monitored with the track finding efficiency, which is the fraction of level 3 tracks that can be matched to an XFT track out of all level 3 tracks. The XFT monitor increments the denominator for each level 3 track. It also increments the numerator if it can match an XFT track to the same level 3 track. The efficiency is the numerator divided by the denominator.

The track matching works as follows. The XFT monitor calculates the closest segment to the level 3 track within each axial superlayer (2, 4, 6, and 8). It does the same for the XFT tracks and then compares the XFT and level 3 segments for each superlayer and then considers the maximum of those four distances for each XFT track. The XFT track with the smallest maximum distance is considered the closest track. If the segments of the closest XFT track and the level 3 track are within 5 segment distances of each other for all four axial superlayers, then the tracks match. The segments corresponding to a level 3 track are calculated at the middle of each superlayer. The XFT segments are calculated in the same way from the TL2D track information.

2.5.2 Monitoring Plots

This section shows the histograms generated by the XFT monitor and discuss the criteria for alarm. The histograms in this section were generated from stream A data between run 254999 and 255090 and required the `TEST_EXPRESS_W_NOTRACK_ROLXFT` trigger. The errors in the histograms are calculated using the Wilson Score Interval for one standard deviation.

Table 2.6: The following shows the most inefficient wires. These are the wires that have a hit efficiency of less than 1 with a confidence of 3 standard deviations. This corresponds to the output of the XFT monitor.

Superlayer: 2	Cell: 147	Wire: 11	Phi: 4.81056	Efficiency: 0.0416667	Error: 0.0306995
Superlayer: 4	Cell: 100	Wire: 0	Phi: 2.18166	Efficiency: 0.109375	Error: 0.0537616
Superlayer: 7	Cell: 199	Wire: 4	Phi: 2.89434	Efficiency: 0.03125	Error: 0.03125
Superlayer: 7	Cell: 199	Wire: 5	Phi: 2.89434	Efficiency: 0.0357143	Error: 0.0357143
Superlayer: 7	Cell: 217	Wire: 0	Phi: 3.15614	Efficiency: 0.675	Error: 0.104346
Superlayer: 7	Cell: 237	Wire: 11	Phi: 3.44703	Efficiency: 0.59375	Error: 0.122634
Superlayer: 7	Cell: 246	Wire: 6	Phi: 3.57792	Efficiency: 0.09375	Error: 0.0679882
Superlayer: 7	Cell: 385	Wire: 0	Phi: 5.5996	Efficiency: 0.15625	Error: 0.0880193

Figures 2.9, 2.10, and 2.11 show the plots that are displayed in the control room and monitored by a shift crew member. The background colors give a general indication of the XFT's state. When they are all green then everything is fine, or, in other words, all the efficiencies are above the alarm threshold, which is indicated by the dotted line. When a plot has a red background then the efficiencies dropped below the alarm threshold and an expert should be notified. Finally, a blue background indicates that the statistics are insufficient to make a conclusive statement on the XFT's state.

Figure 2.9 shows the track finding efficiency and track occupancy, Fig. 2.10 shows the segment finding efficiency for each superlayer, and Fig. 2.11 shows the worst hit finding efficiency per TDC for each superlayer. Fig. 2.10 shows a drop in the segment finding efficiency for superlayer 7. This drop can also be observed in Fig. 2.11 for the hit finding efficiency, which means that the drop is caused by some broken wires (see Table 2.6).

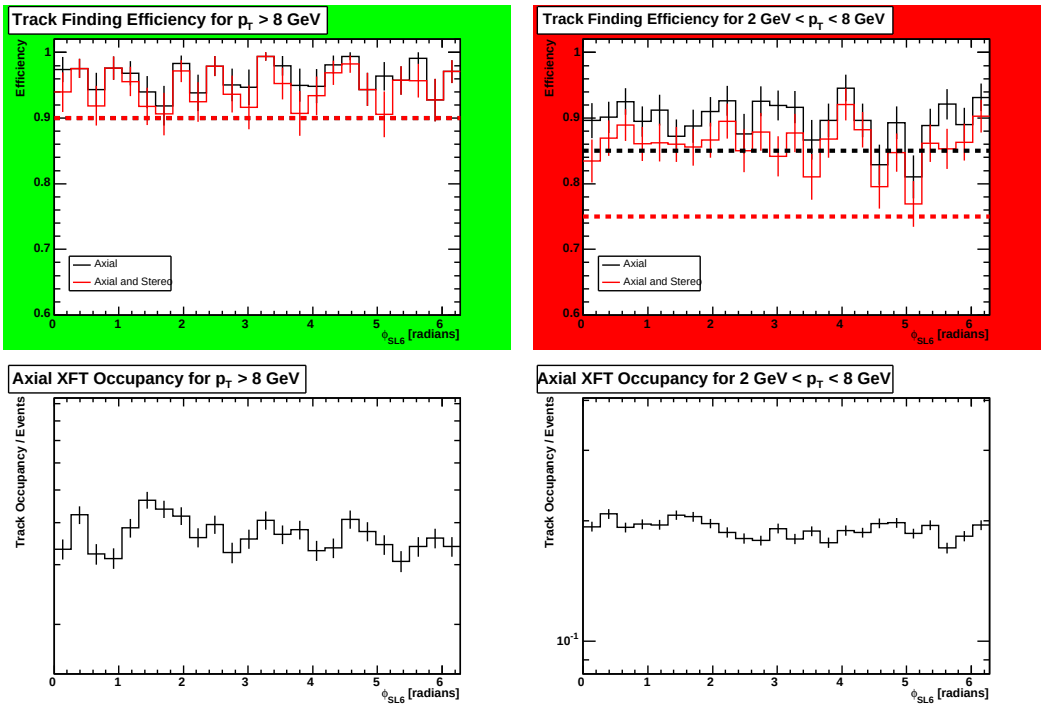

Figure 2.9: The top two plots show the track finding efficiency as a function of ϕ_{SL6} for different p_T cuts; high p_T is left and low p_T is right. ϕ_{SL6} is the angle of the level 3 track at the radius of the center of superlayer 6. The black line gives the efficiency for the axial system only (superlayers 2, 4, 6, and 8) and the red line shows the efficiencies for the entire system. The alarm thresholds, which are indicated by the dotted lines, can be set individually for the black and red efficiencies. The axial efficiency in the low p_T plot (right) drops below the alarm threshold for two bins, so the background changes to red in order to alarm the shift crew. The bottom two plots show the XFT track occupancy for high p_T (left) and low (right) p_T. These plots are included to make sure that there are no problems in any section of the detector. If there were a problem in one part of the detector then the efficiency would not change, but one would observe a drop in the track occupancy.

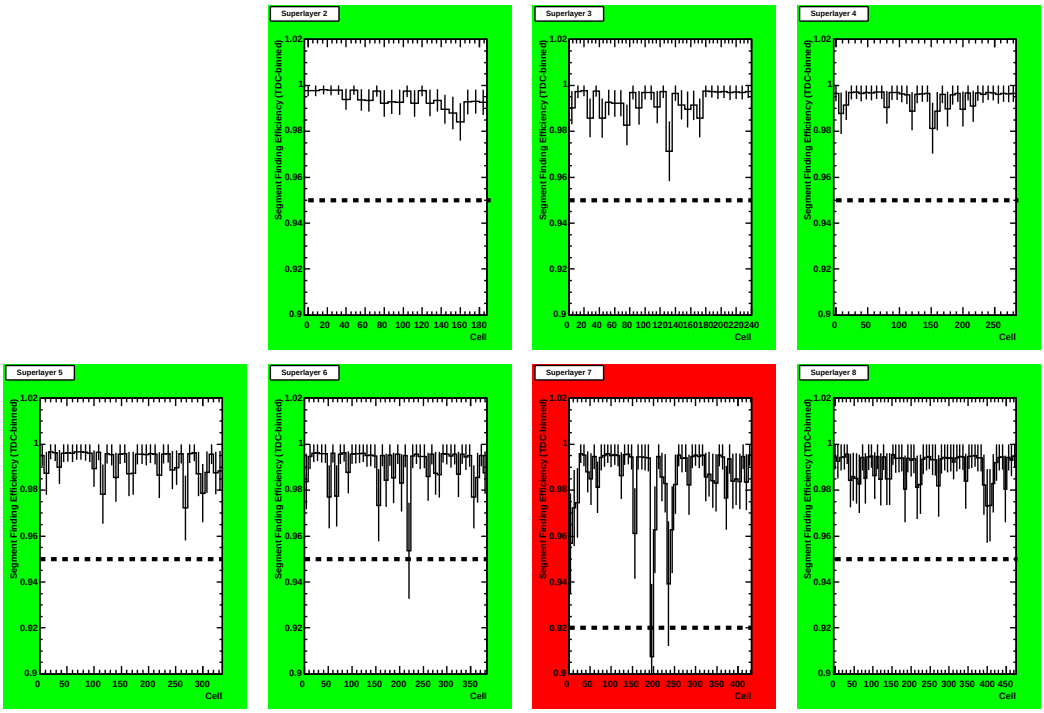

Figure 2.10: The segment finding efficiency for each superlayer. The background of the superlayer 7 plot turned red in order to alarm the shift crew because one of the efficiency bins dropped below the alarm threshold, which is indicated by the dotted line.

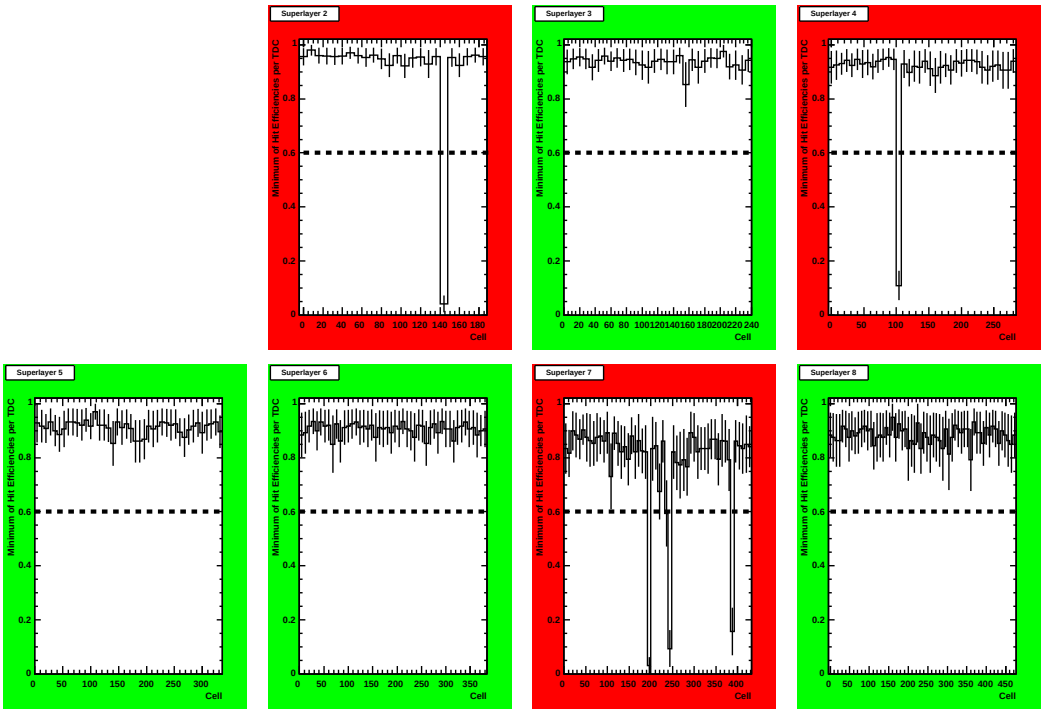

Figure 2.11: The worst hit finding efficiency within each set of 96 wires for each superlayer. The background of the superlayer 3, 4, and 7 plots turned red in order to alarm the shift crew because one or more of the efficiency bins dropped below the alarm threshold, which is indicated by the dotted line.

CHAPTER THREE

Object Identification

3.1 Introduction

This chapter describes the event selection that we use to isolate Higgs production in association with a W boson. As described in Chap. 1, the final state considered in this analysis consists of a lepton and a neutrino from the W decay and a bottom and antibottom quark pair ($b\bar{b}$) from the Higgs decay. Section 3.2 will describe how the decay products from the W boson are identified, and Sec. 3.3 will describe how the decay products of the Higgs boson are identified.

3.2 W Decay

The W boson has two main decay modes: leptonic and hadronic. Leptons are easier to identify in our detector than hadrons because they only consist of one high-momentum track in the tracking chamber and an isolated energy deposit in the electromagnetic calorimeter or muon system. Because the Higgs boson decay provides two additional bunches of hadrons, it is difficult to look for an event with four bunches of hadrons as opposed to an event with two hadron bunches and one lepton. For this reason, we only consider the leptonic W decay mode in this analysis. Other groups at CDF consider all hadronic decays. The leptonic decay mode consists of a lepton and its corresponding neutrino.

The W boson, when it decays leptonically, decays into one of three possible lepton/neutrino pairs: e^-/ν_e, μ^-/ν_μ, or τ^-/ν_τ. The first two leptons are easily identified in our detector because the electron is stable and the muon has a relatively long lifetime. However, the tau lepton has a very short lifetime, so it decays before it traverses the detector. This means that in order to identify a tau lepton, its decay

products, which usually manifest themselves as soft jets, have to be reconstructed. There are other groups at CDF that specialize in tau reconstruction and who are in fact working on a WH analysis with a tau-only final state. This analysis only considers the electron and muon final states. In the next sections, we will explain how we identify electrons and muons and describe all the kinematic variables used for identification.

When we look at a data event in our detector, we do not know *a priori* what particles have been produced. We only have the detector read-out, from which we indirectly attempt to identify what particles are produced. The following sections discuss how we use the detector read-out to identify different objects in an event.

This analysis uses two types of electrons: central and forward electrons. The central electrons are detected with the use of the CEM (see Sec. 2.3.4.1), so we refer to them as CEM electrons. The forward electrons are identified with the use of the PEM (see Sec. 2.3.4.1) and have to be matched to a Phoenix track, so we refer to them as PHX electrons. There are two types of muons that we use in this analysis. The first type is identified by the CMUP (see Sec. 2.3.5), so we refer to them as CMUP muons. The second type is identified with the use of the CMX (see Sec. 2.3.5), so we refer to them as CMX muons.

Let us now consider each one of the four lepton types (CEM, PHX, CMUP, CMX) and their identification individually.

3.2.1 CEM Electrons

The first step to identifying a CEM electron is to look for an isolated track together with an energy deposit in the CEM. We use two types of selection variables, kinematic and identification variables. Let us first consider the requirements on the kinematic selection variables:

- $E_T > 20.0$ GeV
- $z_0^{track} < 60.0$ cm
- Central Region ($|\eta| < 1.1$)
- Fiducial to CES
- Conversion rejection
- Isolation / $E_T < 0.1$
- N(Axial Track Segments) ≥ 3
- N(Stereo Track Segments) ≥ 2
- $p_T^{\text{track}} > \begin{cases} 10.0 \text{ GeV}/c \text{ and } E/p < 2 & \text{when } E_T < 100.0 \text{ GeV} \\ 50.0 \text{ GeV}/c & \text{when } E_T \geq 100.0 \text{ GeV} \end{cases}$

Let us look at each of the kinematic selection variables above and explain them in detail. We will only use 3-vectors in the following discussions:

- p_T^{track}: The magnitude of the track's momentum vector of the electron projected into the transverse plane of the detector, the xy-plane (see Sec. 2.3.1):

$$p_T^{\text{track}} = p^{\text{track}} \sin\theta \tag{3.1}$$

- E: The energy read out of the calorimeter in the direction of the track's momentum (p^{track}).

- E_T: The transverse energy, which is the calorimeter energy scaled by the transverse component of the momentum (see Sec. 2.3.1):

$$\begin{aligned} E_T &= E\left(\frac{p_T^{\text{track}}}{p^{\text{track}}}\right) && (3.2) \\ &= E\sin\theta && (3.3) \end{aligned}$$

- E/p: The ratio of energy to momentum. This can be rewritten as follows:

$$\frac{E}{p} = \frac{\sqrt{p^2+m^2}}{p} = \sqrt{1+\left(\frac{m}{p}\right)^2} \tag{3.4}$$

We expect this ratio to be close to unity for a particle with a mass much smaller than its momentum. This is the case for electrons since p is larger

than 10.0 GeV/c and $m_{e^-} = 0.511$ MeV/c^2 (see Table 1.1). Since we are working in natural units where $c = 1$, we omitted the extra factor of c in the above equation, which is necessary for this ratio to be unitless.

- z_0^{track}: The z component of the track where it intersects the beam line.
- Conversion rejection: We reject electrons that likely came from a conversion ($\gamma \to e^- e^+$) [24].
- Isolation / E_T: The energy deposited in the CEM within a cone of $\Delta R = 0.4$ around the electron cluster, but not including the energy of the electron cluster itself, divided by the electron E_T.
- N(Track Segments): Each superlayer in the COT has one layer of segments, which are reconstructed from at least five wire layers. This requirement is equivalent to requiring a track to have been registered on at least N superlayers with at least five hits in each superlayer. We make separate requirements for stereo and axial superlayers.

Now that we have defined all of the kinematic selection variables, let us consider the requirements on the identification variables. These variables help us distinguish electrons from other particles:

- $|\Delta Z_{\text{CES}}| < 3.0$ cm
- CES Strip $\chi^2 < 10.0$
- $L_{\text{shr}} < 0.2$
- $-3.0 < q \cdot \Delta X_{\text{CES}} < 1.5$
- $E_{\text{HAD}}/E_{\text{EM}} < 0.055 + 0.00045E$

Let us now examine each of the identification selection variables:

- $\Delta Z_{\rm CES}$ and $\Delta X_{\rm CES}$: The difference in the distances between the CES cluster position and its associated track extrapolated to that cluster in the z and transverse direction, respectively.

- CES Strip χ^2: Result from a χ^2 fit of the measured shower profile to an electron baseline shower profile acquired during test beam.

- $L_{\rm shr}$: Lateral shower sharing variable. It is defined as follows:

$$L_{\rm shr} = \frac{0.14 \sum_i (M_i - P_i)}{\sqrt{(0.14\sqrt{E_{\rm EM}})^2 + \sum_i (\Delta P_i)^2}} \tag{3.5}$$

  where the sums are over the towers in the EM cluster adjacent to the seed tower and in the same wedge as the seed tower. M_i is the measured energy in an adjacent tower, P_i is the predicted energy deposit in the adjacent tower, $E_{\rm EM}$ is the total electromagnetic energy in the cluster, and ΔP_i is an estimate of the uncertainty in P_i. This cut is effectively an energy isolation cut [25].

- $E_{\rm HAD}/E_{\rm EM}$: The ratio of energy measured in the hadronic calorimeter divided by the energy measured by the electromagnetic calorimeter. Electrons deposit the majority of energy in the electromagnetic calorimeter, so this ratio should be small for real electrons.

3.2.2 PHX Electrons

The identification of PHX electrons proceeds in a similar way as for CEM electrons except that we are now interested in electron objects in the plug region. The PHX electrons are reconstructed only using the tracking information from the silicon system and not from the COT. Here are the kinematic requirements that we place on PHX electrons:

- $E_T > 20.0$ GeV
- $z_0^{\text{track}} < 60.0$ cm
- Plug Region ($1.2 < |\eta| < 2.0$)
- N(Silicon Track Hits) ≥ 3
- $E_{\text{HAD}}/E_{\text{EM}} < 0.05$
- Isolation / $E_T < 0.1$
- PEM 3x3 $\chi^2 < 10.0$
- $1.2 < \eta_{\text{PES,2D}} < 2.0$
- ΔR(PES, PEM) < 3.0
- PES 2D 5x9 U > 0.65 and PES 2D 5x9 V > 0.65 when $E_T < 100.0$ GeV

The following explains all of the PHX-specific variables that have not already been mentioned in Sec. 3.2.1:

- N(Silicon Track Hits): The number of hits in the silicon tracker associated with the track.
- PEM 3x3 χ^2: Similar to CES Strip χ^2 except in the plug region using 9 PEM towers.
- $\eta_{\text{PES,2D}}$: The pseudorapidity measured by the PES cluster best matched to the track.
- ΔR(PES, PEM): The difference in R between the PES and PEM position measurement.
- PES 2D 5x9 U and V: The energy ratio of the central 5 towers to all 9 towers.

3.2.3 CMUP Muons

A muon is identified by a stub in the muon system together with a track pointing to that stub. We consider two types of muons corresponding to the two

muon systems: CMUP and CMX. The following list gives the requirements that we place on the identification of a CMUP muon. The additional muon variables are described at the end of Sec. 3.2.4:

- $p_T > 20.0$ GeV/c
- $z_0^{\text{track}} < 60.0$ cm
- $N(\text{Axial Track Segments}) \geq 3$
- $N(\text{Stereo Track Segments}) \geq 2$
- Fiducial to CMU
- Fiducial to CMP
- $|\Delta X_{\text{CMU}}| < 7.0$ cm
- $|\Delta X_{\text{CMP}}| < 5.0$ cm
- $E_{\text{HAD}} < \begin{cases} 6.0 \text{ GeV} & \text{when } p \leq 100.0 \text{ GeV}/c \\ 6.0 \text{ GeV} + 0.0280(p - 100.0) \text{ GeV} & \text{when } p > 100.0 \text{ GeV}/c \end{cases}$
- $E_{\text{EM}} < \begin{cases} 2.0 \text{ GeV} & \text{when } p \leq 100.0 \text{ GeV}/c \\ 2.0 \text{ GeV} + 0.0115(p - 100.0) \text{ GeV} & \text{when } p > 100.0 \text{ GeV}/c \end{cases}$
- $|d_0^{\text{track}}| < \begin{cases} 0.2 \text{ cm} & \text{when } N(\text{Silicon Track Hits}) = 0 \\ 0.02 \text{ cm} & \text{when } N(\text{Silicon Track Hits}) > 0 \end{cases}$

3.2.4 CMX Muons

The CMX identification requirements are very similar to the CMUP requirements except that we now put requirements on the CMX system instead of the CMUP system. The following shows all of the CMX identification requirements:

- $p_T > 20.0$ GeV
- $z_0^{\text{track}} < 60.0$ cm
- $N(\text{Axial Track Segments}) \geq 3$
- $N(\text{Stereo Track Segments}) \geq 2$
- Fiducial to CMX
- $|\Delta X_{\text{CMX}}| < 6.0$ cm
- $\rho_{\text{COT}} > 140.0$ cm

- Exclude wedge 14W for runs in the range: $190697 \leq \text{run} < 209760$

- $E_{\text{HAD}} < \begin{cases} 6.0 \text{ GeV} & \text{when } p \leq 100.0 \text{ GeV}/c \\ 6.0 \text{ GeV} + 0.0280(p - 100.0) \text{ GeV} & \text{when } p > 100.0 \text{ GeV}/c \end{cases}$

- $E_{\text{EM}} < \begin{cases} 2.0 \text{ GeV} & \text{when } p \leq 100.0 \text{ GeV}/c \\ 2.0 \text{ GeV} + 0.0115(p - 100.0) \text{ GeV} & \text{when } p > 100.0 \text{ GeV}/c \end{cases}$

- $|d_0^{\text{track}}| < \begin{cases} 0.2 \text{ cm} & N(\text{Silicon Track Hits}) = 0 \\ 0.02 \text{ cm} & N(\text{Silicon Track Hits}) > 0 \end{cases}$

The CMUP and CMX specific variables, which have not already been mentioned in Secs. 3.2.1 and 3.2.2 include:

- d_0^{track}: The distance of closest approach of the track to the beamline.

- ρ_{COT}: The radial distance from the beam pipe at which the reconstructed track crosses the end plane of the COT. This requirement ensures that the muon is within the range of the CMX trigger.

3.2.5 Neutrinos

Neutrinos have no charge and very small masses, so they interact very weakly with other matter, specifically with our detector. In fact, the probability that a neutrino interacts with our detector is so low that we do not consider neutrino detection at all and simply consider neutrinos to have escaped our detector. This means that we can only infer their presence indirectly by an overall deficit in detector energy. We therefore calculate a two-dimensional vector quantity known as the missing transverse energy, denoted by $\not\!\!E_{\mathbf{T}}$ and defined as follows:

$$\not\!\!E_{\mathbf{T}} = -\sum_i \mathbf{p_T}(i) \tag{3.6}$$

Table 3.1: This table gives the minimum required $\not\!\!E_T$ for each lepton category.

Lepton Type	Minimum $\not\!\!E_T$
CEM	20 GeV
PHX	25 GeV
CMUP	20 GeV
CMX	20 GeV

where $\mathbf{p_T}$ is the transverse momentum vector and the sum is over all detected particles. We will often refer to the magnitude of the missing transverse energy momentum vector by $\not\!\!E_T$. Since the neutrino carries half the energy of the W boson, which is at least half the rest mass of a W boson ($m_W = 80.4$ GeV/c^2), it should have an energy larger than 40 GeV. The transverse missing energy ($\not\!\!E_T$) is only a fraction of the total energy, so we place a conservative $\not\!\!E_T$ requirement on events. Table 3.1 shows the $\not\!\!E_T$ requirement for the different lepton categories.

3.3 H Decay

In this analysis, we search for a Higgs boson that decays to a bottom quark and an antibottom quark. When quarks are formed, they fragment into many particles because the isolated colored quarks will pull other quarks out of the vacuum to create more stable colorless hadrons. This creates a spray of particles, which we call a jet. Section 3.3.1 will explain how jets are identified. Once the jets are identified, we want to know which ones correspond to bottom quarks. According to the CKM matrix entry V_{tb}, the bottom quarks should transition more than 99% of the time to top quarks, but the mass of the top quark is so large that this transition is energetically unfavorable. This means that the bottom quarks will hadronize into B mesons before they decay to other quarks. Section 3.3.2 will explain how we identify bottom quarks.

3.3.1 Jets

When an isolated quark is generated in a collision, it will pull other quarks out of the vacuum, using the color force to form colorless hadrons. These hadrons will in turn decay as they travel through the detector. By the time all of the quark's decay products interact with our detector, they form a wide spray of particles, which is collectively known as a jet. We use jets to deduce the presence of quarks in our collisions. If there were only one quark in an event, this would amount to the easy task of summing together the momentum vectors of all particles in an event. Other particles are created from the underlying event and other interactions with the detector. This means that we have to cluster together the particles that actually came from the quark. There are many algorithms used for identifying jets.

Jet identification is a fascinating subject of study that brings theorists, phenomenologists, and experimentalists together. To date, there is no agreement on the best method of jet identification. The main difficulty with jet identification is that we do not fully understand the theory behind quark hadronization, which makes it difficult to simulate. For this reason, there are many algorithms that are used to identify jets. In this analysis, we use the JetClu algorithm with a cone size of $R = 0.4$. In Sec. 6.4.2, we will use an additional clustering algorithm, the K_T algorithm, to better understand the three-jet sample.

After the JetClu algorithm clusters all of the jets, we apply the following selection criteria to every jet to identify which ones to use for our analysis:

- Jet energy corrected $E_T > 20.0$ GeV
- $|\eta_{\text{detector}}| < 2.0$

In this analysis, we use level 5 corrected jets, which means that the jet energy is corrected for all of the following effects:

- Online/Offline Calibrations. Measured calibration factors are applied to the following subsystems to readjust their energy scales: CEM, CHA, WHA, PEM, PHA, and PPR.

- Eta Dependence. This correction makes the measured jet energies uniform along η. It is applied to jets outside of $0.2 < |\eta| < 0.6$ to make their energy scale correspond to jets inside that region.

- Multiple Interactions. When there is more than one interaction in a $p\bar{p}$ collision, the additional decay products contribute to the overall jet cluster energy. This contribution is subtracted out in the average.

- Energy Non-Linearity. This corrects the jet energy for any energy measurement non-lineartity of the calorimeters since the measured energy is always less than the true energy, especially for particles with low transverse momentum.

We sort the set of jets in descending order by jet-corrected E_T, so the first jet will always be the jet with highest jet-corrected E_T.

3.3.2 Bottom Quark Identification

We are given a set of jets in each event, and we now have to determine which ones correspond to bottom quarks. We use so-called tagging algorithms to determine which jets are likely to originate from a bottom quark. Specifically, we use three tagging algorithms in this analysis: the Secondary Vertex Tagger, the Jet Probability Tagger, and the Roma Neural Network Tagger. The following sections will explain each tagger in more detail.

3.3.2.1. *Secondary Vertex Tagger* The Secondary Vertex Tagger exploits the long lifetime of the b-hadrons. It reconstructs a secondary decay vertex displaced

from the interaction point. When the vertex is displaced sufficiently, the tagger tags the jet under consideration. The tagger provides three mutually exclusively outcomes: no tag, negative tag, or positive tag. A tag is considered positive when it is in line with the event kinematics and negative when it is on the opposite side of the primary vertex [26].

3.3.2.2. *Jet Probability Tagger* The Jet Probability Tagger uses track impact parameters to calculate the probability that a jet originated from the primary vertex [27]. This probability is very low for long-lived jets, so we require a probability less than 5% for a jet to be considered tagged.

3.3.2.3. *Roma Neural Network Tagger* This tagger uses an array of kinematic variables to train several neural networks [28]. We then cut on a specific value of the combined neural network output to use the tagger in a binary mode. There are three operating points that we can use: tight, loose, and ultra-loose [10]. This analysis uses the ultra-loose operating point to maximize the number of tagged jets, so we require a Roma neural network output larger than 0.0.

3.3.2.4. *Tagging Categories* As mentioned before, we are considering the Higgs decay to a bottom and an antibottom quark, which will yield two b-jets in our detector, so we use different combinations of tagged jets for each event. First, we must assign every jet one of the following tags:

(1) Secondary Vertex tag.

(2) Jet Probability tag, but no Secondary Vertex tag.

(3) Roma Neural Network tag, but no Jet Probability tag or Secondary Vertex tag.

(4) No tag.

We then combine the jet tags in each event to categorize the event. Every event falls into one of the following five tagging categories:

- $\geq$2S: The event contains two or more jets with a Secondary Vertex tag.
- S+J: The event contains one jet with a Secondary Vertex tag and at least one other jet with a Jet Probability tag.
- S+R: The event contains one jet with a Secondary Vertex tag and at least one other jet with a Roma Neural Network tag.
- 1S: The event contains exactly one jet with a Secondary Vertex tag and the other jets have no tags.
- none: The event does not contain a jet with a tag.

CHAPTER FOUR

Event Selection and Categorization

4.1 Introduction

In this chapter we discuss how to select events that are likely WH signal events from the data sample collected by the CDF detector. In the previous chapter, we saw how the different kinematic objects in a given event are identified. We now use these objects to find events with a WH decay signature, called WH events. The goal is to reject as many non-WH events as possible while keeping all of the WH events. At the end of this chapter, we describe how we separate the selected data sample into mutually independent samples, which are called analysis channels.

4.2 Data Sample

In this analysis, we use the data collected by the CDF detector during Run II from February 4, 2002 to June 19, 2010. When protons and antiprotons collide in the detector, we record the triggered output, which is known as an event. The time for which we continuously collect events is known as a run, which can be as short as a few minutes or as long as an entire day. We organize run ranges into periods. The data sample that corresponds to the dates at the beginning of this section starts with period 0 and run 138425 and ends with period 30 and run 293800. We also split the recorded data into data sets according to which triggers were fired (see Sec. 2.4). For this analysis, we use the following three data sets: `bhel` (central electrons), `bpel` (plug electrons), and `bhmu` (central muons).

4.3 Event Selection

This section explains each selection requirement in detail. We apply this event selection not only to the data sample, but also to samples of simulated events from

Monte Carlo (MC) programs (see Sec. 5.2), so we will note when the selection differs for the data or MC sample.

4.3.1 Good Runs

When we collect data in our detector, it sometimes happens that a detector component malfunctions, rendering part of the data useless. Instead of deleting every event for which there is a problem, CDF compiles lists of runs that are considered good or useful for analysis. These lists are compiled for different detector components. For data, we use the Top Group's version 36 good run list, which contains all of the runs with a functional silicon tracker, electron systems, and central muon systems (CMU, CMP, and CMX) where the CMX is ignored for runs before run 150145. For MC, we use the good run list that contains the runs with functional silicon tracker and electron systems.

4.3.2 Good z_0 Vertex

We only select MC events with a primary z vertex (z_0) within 60.0 cm because our detection efficiency decreases with z vertices further from the detector center [29].

4.3.3 Triggers

As explained in Sec. 2.4, we reduce the amount of data collected by only recording events that pass a set of predefined triggers. For this analysis, we require data events to pass at least one of the following level 3 triggers. There is a different set of triggers for each lepton type:

- CEM: We require `ELECTRON_CENTRAL_18` for all runs.
- PHX: We require `MET_PEM` for all runs.

- CMUP: For runs before and including run 229763, we require `MUON_CMUP18` or `MUON_CMUP18_L2_PT15`. After run 229763, we only require `MUON_CMUP18`.

- CMX: Table 4.1 shows the trigger requirements for the CMX muons.

The main triggers are explained in detail in Appendix A. We do not have a trigger requirement for MC events because the detector simulation does not model the triggers well.

Table 4.1: The trigger requirements for the CMX muons.

Run Range	Required Triggers
run $\leq$ 200272	`MUON_CMX18` or `MUON_CMX18_L2_PT15`
200272 $<$ run $\leq$ 226194	`MUON_CMX18_L2_PT15` or `MUON_CMX18_L2_PT15_LUMI_200`
226194 $<$ run $\leq$ 257201	`MUON_CMX18_&_JET10` or `MUON_CMX18_&_JET10_LUMI_270` or `MUON_CMX18_&_JET10_DPS`
257201 $<$ run	`MUON_CMX18`

4.3.4 Number of Leptons

The event must contain exactly one lepton that passes all of the identification requirements from Chap. 3. We also veto dilepton events, which are events that contain two or more of any combination of the following leptons:

- Tight leptons: leptons that pass the requirements from Chap. 3.

- Non-isolated leptons: leptons that pass the requirements from Chap. 3 except that the isolation / E_T cut is reversed. In other words, we require the lepton to have an isolation / E_T of larger than 0.1.

- Loose leptons: leptons that have looser requirements than the tight leptons. We use the definition from the `smry` branch.

- Fake leptons: These leptons are used for the construction of the non-W templates, which will be described in Secs. 5.4.1 through 5.4.3.

One of the purpose of the dilepton veto is to keep single-lepton analyses like this one and many-lepton analyses mutually exclusive. In other words, this veto ensures that we do not count events twice when the results of all analyses are combined. In addition, the dilepton veto helps to eliminate events that come from top quark pair production and events that contain a Z boson.

4.3.5 Z Veto

Since we are only interested in events that contain a W boson, we veto events that likely contain a Z boson due to misidentification of one of the leptons from the Z decay. This is achieved by rejecting events that contain a track, electromagnetic cluster, or jet that together with the lepton form an invariant mass between 76 and 106 GeV/c^2. This does not eliminate all of the Z events, but it keeps their number very small (see Sec. 5.6).

4.3.6 Cosmic Veto

Highly energetic muons can be created in the upper atmosphere and then penetrate our detector, so we veto any muon that comes from outside the detector. This is achieved by excluding events that contain back-to-back muons with the same impact parameter (d_0^{track}). We do not apply this veto to MC events because cosmic rays are not simulated in the CDF detector simulation.

4.3.7 Same Interaction

In order to ensure that the lepton and jets originate from the same interaction, we require that their initial z vertices are separated by less than 5.0 cm. This ensures that we do not consider objects from separate decay processes in one event.

4.3.8 Duplicate Events

It sometimes occurs that the same event ends up in multiple data sets, so in order to prevent double counting, we ensure that each event is only read once.

4.3.9 Heavy Flavor Filter

In Sec. 5.3.1, we will discuss the composition of the W + jets MC sample generated with two MC generators. The second generator adds extra partons to each sample, so sometimes an event that is only supposed to contain light-flavored quarks can end up with a heavy-flavored quark (b or c). In order to prevent this from happening, we veto events from the W + jets and Z + jets MC samples that contain inappropriate quarks. Specifically, we veto all W + LF and Z + LF events that contain one or more charm or bottom quarks, and we veto all $W + c/c\bar{c}$ and $Z + c\bar{c}$ events that contain a bottom quark. LF stands for light-flavored quarks and refers to u, d, and s.

4.3.10 QCD Veto

Some of the largest background sources are QCD multijet interactions that create heavy jets but do not contain a Higgs boson. This is one of the least understood backgrounds and hence the most difficult to exclude. There have been many studies of how to optimize this veto. In this analysis we chose to use the QCD veto that was used in the single-top analysis, which varies for each lepton type [30]. Before we detail the QCD vetoes, let us define two important quantities. The first

is the transverse mass of the W boson, which is calculated as follows:

$$\frac{1}{2}m_T^2 = p_T(\not\!\!E_T)p_T(\text{Lepton}) - p_x(\not\!\!E_T)p_x(\text{Lepton}) - p_y(\not\!\!E_T)p_y(\text{Lepton}) \quad (4.1)$$

Note that the transverse component of the $\not\!\!E_T$ vector is the same as the $\not\!\!E_T$. The second quantity is the $\not\!\!E_T$ significance, which is defined as follows:

$$\begin{aligned} \not\!\!E_{T\text{sig}} &= \frac{\not\!\!E_T}{\sqrt{\Delta\not\!\!E_T}} \\ \Delta\not\!\!E_T &= \sum_{\text{jet}} \left[C_{\text{JES}}^2 \cos^2(\Delta\phi(\not\!\!\mathbf{E_T}, \mathbf{p}_{\text{jet}}))E_{T,\text{jet}}\right] \\ &\quad + \cos^2(\Delta\phi(\not\!\!\mathbf{E}_{\mathbf{T},\text{vtx}} + \sum_{\text{jet}} \mathbf{p}_{\text{jet}}), \not\!\!\mathbf{E_T}))(E_{T,\text{sum}} - \sum_{\text{jet}} E_{T,\text{jet}}) \end{aligned} \quad (4.2)$$

where C_{JES} is the jet energy correction factor, $\not\!\!\mathbf{E}_{\mathbf{T},\text{vtx}}$ is the two-dimensional $\not\!\!E_T$ vector read out from the vertex branch, $E_{T\text{sum}}$ is the scalar sum of E_T read out of the met branch, and all bold faced quantities represent two-dimensional vectors in the transverse plane.

Here are the QCD vetoes for each lepton type:

- CEM: Veto events that have fewer than two tagged jets and for which any one of the following conditions holds:
  - $m_T < 20$ GeV/c^2
  - $\not\!\!E_{T\text{sig}} < -0.05m_T + 3.5$
  - If the event contains one jet,

    $\not\!\!E_{T\text{sig}} < -7.6 + 3.2|d\phi(\text{Lepton}, \text{Leading Jet})|$
  - If the event contains two or more jets,

    $\not\!\!E_{T\text{sig}} < 2.5 - 3.125|d\phi(\not\!\!E_T, \text{Second Leading Jet})|$
- PHX: Veto events for which any one of the following conditions holds:
  - $m_T < 20$ GeV/c^2

- $\not\!\!E_{T\,\mathrm{sig}} < 2.0$
- $\not\!\!E_T < 45 - 30|d\phi(\not\!\!E_T, \text{Leading Jet})|$
- If the event contains two or more jets,
  $\not\!\!E_T < 45 - 30|d\phi(\not\!\!E_T, \text{Second Leading Jet})|$

- CMUP: Veto events that have fewer than two tagged jets and for which the following condition holds:
  - $m_T < 10$ GeV/c^2
- CMX: Veto events that have fewer than two tagged jets and for which the following condition holds:
  - $m_T < 10$ GeV/c^2

One of the general principles for the design of the above veto is that we do not veto double tagged events in the TLEP sample.

4.4 Event Classification

Now that we have selected the events that we believe have the maximal fraction of *WH* events, let us classify them into different analysis channels. The signal sample is first split into two large samples, the two-jet sample and the three-jet sample. Within each sample, we further divide the events into twelve orthogonal analysis channels. First, we analyze each lepton category separately, so each sample is divided into four lepton categories in the following order: CEM, PHX, CMUP, and CMX. In some cases, we summarize the CEM, CMUP, and CMX lepton categories into one category entitled tight leptons (TLEP). Then we split the sample one more time based on tagging category, so that each tagging category is analyzed separately. The four tagging categories are: $\geq$2S, S+J, S+R, and 1S. Section 3.3.2.4 explains these tags in detail. Table 4.2 shows all twenty-four channels schematically.

We also need control samples to ensure that our background modeling is correct outside of the signal region. We pick two control regions for untagged and single tagged events. The first region consists of events that contain exactly one jet, and the second region consists of events that contain four or more jets. By definition, an event with two or more tagged jets has to contain at least two jets, so the control region for events with more than one tagged jet consists of events that contain four or more jets. The jet counts are based on jets that pass the identification requirements from Sec. 3.3.1. We also use the entire data sample before application of tagging information as a control sample, which is known as the pretag sample.

Table 4.2: The subdivision of the 24 analysis channels.

2 Jets	CEM ≥2S	CEM S+J	CEM S+R	CEM 1S
	CMUP ≥2S	CMUP S+J	CMUP S+R	CMUP 1S
	CMX ≥2S	CMX S+J	CMX S+R	CMX 1S
	PHX ≥2S	PHX S+J	PHX S+R	PHX 1S
3 Jets	CEM ≥2S	CEM S+J	CEM S+R	CEM 1S
	CMUP ≥2S	CMUP S+J	CMUP S+R	CMUP 1S
	CMX ≥2S	CMX S+J	CMX S+R	CMX 1S
	PHX ≥2S	PHX S+J	PHX S+R	PHX 1S

CHAPTER FIVE

Background Modeling

5.1 Introduction

In order to calculate the amount of signal in our data, we first need to understand all of the backgrounds. The data sample consists of events that pass the data selection criteria detailed in Chap. 4, which include events that contain one lepton, one neutrino, one bottom quark jet, and one antibottom quark jet. We attempt to isolate events from associated Higgs boson production with this selection, but of course some events with the same decay products from different decay processes also become included in this selection, as well as events bearing the same event signature as associated Higgs boson production due to the misidentification of some object. Such events are called background events. In this chapter, we explain how we model these background events. In Chap. 6, we will use these models to help us separate background-like data events from signal-like data events.

The method that we use to model the background events is commonly known at CDF as Method II and has successfully been used in the $t\bar{t}$ cross section measurement [31] and the single top observation [30]. This method relies on the assumption that we understand all of the background processes in the sample. With this assumption, some of the backgrounds are fitted to the data to fill in the gaps between the background model and data [32].

5.2 Monte Carlo Based Backgrounds

It might seem that the best way to calculate the kinematic properties of a decay taking place from a $p\bar{p}$ collision inside of the CDF detector would be to use quantum field theory to calculate the appropriate Feynman diagrams. This works

well for the leading-order Feynman diagram that involves the quarks from the proton and antiproton. However, when we start to consider the quarks that are produced in such a collision and try to calculate how they travel through space radiating gluons and creating other quarks from the vacuum, we quickly reach the limits of our understanding. Since we do not completely understand how to model quarks in a vacuum, it would be impossible to calculate the interaction of all the hadronized particles with the CDF detector. For this reason, we make use of Monte Carlo simulations.

A Monte Carlo (MC) simulation is first created based on the leading-order Feynman diagram of a process. The simulation then utilizes statistical techniques to sample the total phase space available to the interacting particles. Instead of providing an analytical output, a MC simulation yields individual events that, within the limit of many events, approximate the physics of the interaction. In this analysis, we use three types of MC-generated samples in order to take advantage of different modeling strengths of the available generators. The first type is entirely generated by PYTHIA version 6.216, and we will refer to such samples as "PYTHIA generated." The second type is generated by ALPGEN version 2.10 prime with the latest updates from MLM and then showered with PYTHIA version 6.325. In other words, ALPGEN calculates the kinematic distributions of the leading-order Feynman diagram particles, and PYTHIA then calculates the gluons that can radiate from the partons, also known as parton showering. We will refer to samples of this second type as "ALPGEN + PYTHIA generated." The third type is generated by MadEvent and showered with PYTHIA and we will refer to such samples as "MadEvent + PYTHIA generated." The MC-generated output is then processed by the CDF detector simulation, which provides its output in the same way as the data. This final output will henceforth be referred to as "MC sample."

We apply the same event selection criteria to the MC samples that we apply to the data. Since each MC sample is generated with an arbitrary number of events, we need to scale the number of MC events such that they properly correspond to the number of collected data events. Furthermore, we need to scale the number of MC events by various efficiencies from the data and MC samples. The following equation gives the scaled number of MC events:

$$N_i = (\sigma \cdot BR)_i \cdot \int L\,dt \cdot \frac{N_i^{\text{sel}}}{N_i^{\text{tot}}} \cdot \epsilon_{z_0}^{\text{data}} \cdot \epsilon_{\text{trig}}^{\text{data}} \cdot SF_{\text{lep ID}} \cdot SF_{\text{tag}} \tag{5.1}$$

- i: Index of MC sample.
- N_i: The number of events of MC sample i that we expect in our data sample.
- $(\sigma \cdot BR)_i$: MC sample i's production cross section multiplied by its branching ratio.
- $\int L\,dt$: Integrated luminosity (see Sec. 2.3.6).
- N_i^{tot}: The "total" number of events of MC sample i that pass the z_0 good vertex and good run list requirements (see Secs. 4.3.2 and 4.3.1).
- N_i^{sel}: The number of events of MC sample i that pass our event selection from Chap. 4.
- $\epsilon_{z_0}^{\text{data}}$: z_0 vertex requirement efficiency in data. This efficiency is used as a luminosity correction since the CLC reports the luminosity for the entire z range [29].
- $\epsilon_{\text{trig}}^{\text{data}}$: Trigger efficiency in data.
- $SF_{\text{lep ID}}$: Lepton identification and reconstruction scale factor.
- SF_{tag}: Tagging scale factor. We use a different scale factor for each tagging category: $SF_{\geq 2\text{S}}$, $SF_{\text{S+J}}$, $SF_{\text{S+R}}$, and $SF_{1\text{S}}$. Note that this scale factor is equal to unity for pretag events.

Table 5.1: The efficiencies and scale factors that we use in this analysis. These numbers come from the Joint Physics Group's scale factor text file for period 28. We use the run-averaged values from the text file. The PHX trigger efficiency is calculated as the product of four trigger efficiency functions parameterized by lepton E_T: `L1L2L3MET`, `L1PEM`, `L2PEM20`, and `L3PEM`.

	$\epsilon_{z_0}^{\text{data}}$	$\epsilon_{\text{trig}}^{\text{data}}$	$SF_{\text{lep ID}}$
CEM	0.972 ± 0.002	0.961 ± 0.004	0.976 ± 0.005
PHX	0.972 ± 0.002	(see caption)	0.918 ± 0.009
CMUP	0.972 ± 0.002	0.877 ± 0.008	0.891 ± 0.009
CMX	0.972 ± 0.002	0.90 ± 0.01	0.948 ± 0.009

The first two terms in Eq. (5.1), $(\sigma \cdot BR)_i \cdot \int L\,dt$, represent the number of events of MC sample i's decay process expected for the collected amount of data. The next term $(\frac{N_i^{\text{sel}}}{N_i^{\text{tot}}})$ gives the efficiency of our data selection in MC sample i. The last four terms scale the number of expected MC events by inefficiencies in data and MC. Tables 5.1 and 5.2 show the efficiencies and scale factors used in this analysis. A scale factor is the ratio of the efficiency in data to the efficiency in MC $(\frac{\epsilon^{\text{data}}}{\epsilon^{\text{MC}}})$. Such scale factors are necessary because the MC cannot model all of the effects in the data perfectly.

The tagging scale factors are more complicated to compute because we have to correct for events migrating between tagging categories due to the individual scale factors. These are the scale factor definitions that we use for this analysis:

$$SF_{\geq 2\text{S}} = SF_{\text{S}}^2 \tag{5.2}$$

$$SF_{\text{S+J}} = SF_{\text{S}}\ SF_{\text{J}} + \frac{1}{N_{\text{S+J}}} \left[2N_{\geq 2\text{S}}\ SF_{\text{S}}\ (1 - SF_{\text{S}})\ SF_{\text{J}}\right] \tag{5.3}$$

$$SF_{\text{S+R}} = SF_{\text{S}}\ SF_{\text{R}} + \frac{1}{N_{\text{S+R}}} \left[2N_{\geq 2\text{S}}\ SF_{\text{S}}\ (1 - SF_{\text{S}})\ (1 - SF_{\text{J}})\ SF_{\text{R}}\right] + \frac{1}{N_{\text{S+R}}} \left[N_{\text{S+J}}\ SF_{\text{S}}\ (1 - SF_{\text{J}})\ SF_{\text{R}}\right] \tag{5.4}$$

Table 5.2: The scale factors for the individual taggers, which are then combined into the scale factors for the individual tagging categories in Eqs. (5.2)–(5.5). The values of the Secondary Vertex and Jet Probability scale factors come from the b-Tagging Group for period 28. The Roma Neural Network tagger value comes from [10]. Muon jets are jets that contain a muon. We use a weighted average to determine the Roma Neural Network scale factor and its unceretainty for each event from the individual scale factors and uncertainties for each jet. We use $\frac{1}{(\Delta SF_j)^2}$ as the weight, where ΔSF_j is the scale factor uncertainty for jet j.

Jet Tagger	$SF_{\text{Jet Tagger}}$
Secondary Vertex (S)	0.96 ± 0.05
Jet Probability (J)	0.78 ± 0.05
Roma Neural Network (R)	0.8881 – 0.0046 (E_T(jet) – 45 GeV) for muon jets 0.785 – 0.182 (N(z-vertices) – 1.8) for non-muon jets

$$
\begin{aligned}
SF_{\text{1S}} \;=\; & SF_{\text{S}} + \\
& \frac{1}{N_{\text{1S}}} \left[2N_{\geq \text{2S}} \; SF_{\text{S}} \; (1 - SF_{\text{S}}) \; (1 - SF_{\text{J}}) \; (1 - SF_{\text{R}}) \right] \\
& \frac{1}{N_{\text{1S}}} \left[N_{\text{S+J}} \; SF_{\text{S}} \; (1 - SF_{\text{J}}) \; (1 - SF_{\text{R}}) \right] \\
& \frac{1}{N_{\text{1S}}} \left[N_{\text{S+R}} \; SF_{\text{S}} \; (1 - SF_{\text{R}}) \right]
\end{aligned} \tag{5.5}
$$

where SF_{S}, SF_{J}, and SF_{R} refer to the scale factors of the three taggers shown in Table 5.2.

The following list shows the decay processes that we treat as MC-based backgrounds:

- Top Pair Production ($t\bar{t}$)
- Single Top Production (s-channel)
- Single Top Production (t-channel)
- Diboson (WW, WZ, and ZZ)
- Z + jets

Table 5.3: The theoretical cross section and branching ratio used for each MC-based background process. The branching ratio depends on the sample in consideration. Some MC samples were generated inclusively with all decay modes, so we only need to multiply by unity. Other samples were generated exclusively with leptonic decays, so we have to use the leptonic branching ratio.

Background	Cross Section (pb)	Branching Ratio
$t\bar{t}$	7.04 ± 0.44	1.0
Single Top (s-channel)	1.046 ± 0.07	0.324
Single Top (t-channel)	2.10 ± 0.19	0.324
WW	11.66 ± 0.70	1.0
WZ	3.46 ± 0.30	1.0
ZZ	1.51 ± 0.20	1.0
Z + jets	787.4 ± 85.0	1.0

Table 5.3 shows the cross sections and branching ratios for each of the above processes. In this analysis we assume a top mass (m_t) of 172.5 GeV/c^2. Table 5.4 shows the identification names and generators used for each MC sample.

5.2.1 Z + Jets

The Z + jets background is considered an MC-based background in this analysis because its overall contribution to our backgrounds is small. There is no MC

Table 5.4: The sample identifications and MC generator used for each MC sample. The information for the Z + jets and W + jets samples appears in Tables 5.5–5.7.

MC Sample Name	Generator	Sample IDs
$t\bar{t}$	PYTHIA	`ttop25`
Single Top (s-channel)	MadEvent + PYTHIA	`stop26 stop23`
Single Top (t-channel)	MadEvent + PYTHIA	`stop27_28 stop3m`
WW	PYTHIA	`ihht1a`
WZ	PYTHIA	`jhht1a`
ZZ	PYTHIA	`khht1a`

sample that contains all of the Z + jets events, so we have to combine the following three samples whose exact composition and relative cross sections are given in Table 5.5:

(1) Z + Light Flavor: One Z boson together with light-flavored quarks (u, d, or s).

(2) $Z + b\bar{b}$: One Z boson together with a pair of bottom/antibottom quarks plus light-flavored quarks.

(3) $Z + c\bar{c}$: One Z boson together with a pair of charm/anticharm quarks plus light-flavored quarks.

Since the relative cross sections of the individual samples are not the same, we have to weigh them as follows when combining them into one Z + jets sample:

$$\begin{aligned} \frac{N^{\text{sel}}_{Z+\text{jets}}}{N^{\text{tot}}_{Z+\text{jets}}} &= \frac{1}{\sigma_{\text{total}}} \sum_j \sigma_j \frac{N^{\text{sel}}_j}{N^{\text{tot}}_j} \\ \sigma_{\text{total}} &= \sum_j \sigma_j \end{aligned} \tag{5.6}$$

The above sum is taken over all Z + jets processes (j) listed in Table 5.5. Equation (5.6) is then plugged into Eq. (5.1) to calculate the number of Z + jets events. One may notice that the individual Z + jets processes are added up in the same way as the other backgrounds except for being scaled by an additional factor of $\frac{\sigma_j}{\sigma_{\text{total}}}$.

5.3 W + Jets Backgrounds

The backgrounds from Sec. 5.2 are all calculated from MC simulations and the corresponding measured cross sections. We will now use a mixture of MC and data to model the backgrounds that contain one W boson and quarks. This is a substantial background for this analysis because it has the same final state as the WH decay. We use the MC sample for the kinematic distributions, but we fit it to

Table 5.5: Sample identifications and relative cross sections for the Z + jets sample. All samples were generated using ALPGEN + PYTHIA. In this table, p stands for parton, which means light-flavored quark (u, d, or s) here.

MC Sample Name	Process	Relative Cross Section (pb)	Sample IDs
Z + Light Flavor	$Z(e,e)+0p$	158	`ztopp0 btopz0`
	$Z(e,e)+1p$	21.6	`ztopp1 btopz1`
	$Z(e,e)+2p$	3.47	`ztop2p btop2d`
	$Z(e,e)+3p$	0.550	`ztop3p btopz3`
	$Z(e,e)+\geq 4p$	0.0992	`ztop4p btopz4`
	$Z(\mu,\mu)+0p$	158	`ztopp5 btopz5`
	$Z(\mu,\mu)+1p$	21.6	`ztopp6 btopz6`
	$Z(\mu,\mu)+2p$	3.47	`ztop7p btop7d`
	$Z(\mu,\mu)+3p$	0.548	`ztop8p btopz8`
	$Z(\mu,\mu)+\geq 4p$	0.0992	`ztop9p btopz9`
	$Z(\tau,\tau)+0p$	158	`ztopt3 btopza`
	$Z(\tau,\tau)+1p$	21.5	`ztopt4 btopzb`
	$Z(\tau,\tau)+\geq 2p$	4.14	`ztopt2 btopzc`
$Z + b\bar{b}$	$Z(e,e)+b\bar{b}+0p$	0.511	`ztopb0 btopzd`
	$Z(e,e)+b\bar{b}+1p$	0.134	`ztopb1 btopze`
	$Z(e,e)+b\bar{b}+\geq 2p$	0.0385	`ztopb2 btopzf`
	$Z(\mu,\mu)+b\bar{b}+0p$	0.511	`ztopb5 btopzg`
	$Z(\mu,\mu)+b\bar{b}+1p$	0.134	`ztopb6 btopzh`
	$Z(\mu,\mu)+b\bar{b}+\geq 2p$	0.0385	`ztopb7 btopzi`
	$Z(\tau,\tau)+b\bar{b}+\geq 0p$	0.625	`ztopbt btopzj`
$Z + c\bar{c}$	$Z(e,e)+c\bar{c}+0p$	1.08	`ztopc0 btopzk`
	$Z(e,e)+c\bar{c}+1p$	0.331	`ztopc1 btopzl`
	$Z(e,e)+c\bar{c}+\geq 2p$	0.107	`ztopc2 btopzm`
	$Z(\mu,\mu)+c\bar{c}+0p$	1.08	`ztopc5 btopzn`
	$Z(\mu,\mu)+c\bar{c}+1p$	0.332	`ztopc6 btopzo`
	$Z(\mu,\mu)+c\bar{c}+\geq 2p$	0.107	`ztktc7 btopzp`
	$Z(\tau,\tau)+c\bar{c}+\geq 0p$	1.28	`ztopct btopzq`

the data to determine the overall normalization. This fit will be described in more detail in Sec. 5.5.

We use this fitting method for the W + jets background instead of calculating it from the measured cross section because if we were to use the cross section, its uncertainty would dominate our systematic uncertainty. The fitting method allows us to measure the contribution of W + jets events in our data sample directly.

5.3.1 W + Jets Kinematic Distributions (Shapes)

As a first step, the W + jets sample is determined in a similar way as the Z + jets sample, except that we do not determine an overall normalization. We use the same process as above (see Eq. (5.6)) to create the following three templates whose exact composition and relative cross sections are given in Tables 5.6 and 5.7:

(1) W + LF: One W boson together with light-flavored (LF) quarks (u, d, or s).

(2) $W + b\bar{b}$: One W boson together with a pair of bottom/antibottom quarks plus light-flavored quarks.

(3) $W + c/c\bar{c}$: One W boson together with one charm quark or a pair of charm/anticharm quarks plus light-flavored quarks:

- $W + c$
- $W + c\bar{c}$

5.3.2 Normalization

Now that we have the shapes of the three W + jets templates (W + LF, $W + b\bar{b}$, and $W + c/c\bar{c}$), we can proceed to determine the normalizations. Before we can understand how the normalization of the W + jets sample is calculated,

Table 5.6: Sample identifications and relative cross section used for the W + LF and $W + b\bar{b}$ samples. All samples were generated using ALPGEN + PYTHIA. In this table, p stands for parton, which means light-flavored quark (u, d, or s) here.

MC Sample Name	Process	Relative Cross Section (pb)	Sample IDs
W + LF	$W(e,\nu_e) + 0p$	1800	ptopw0 utop00
	$W(e,\nu_e) + 1p$	225	ptopw1 utop01
	$W(e,\nu_e) + 2p$	35.3	ptop2w utop02
	$W(e,\nu_e) + 3p$	5.59	ptop3w utop03
	$W(e,\nu_e) + \geq 4p$	1.03	ptop4w utop04
	$W(\mu,\nu_\mu) + 0p$	1800	ptopw5 utop05
	$W(\mu,\nu_\mu) + 1p$	225	ptopw6 utop06
	$W(\mu,\nu_\mu) + 2p$	35.3	ptop7w utop07
	$W(\mu,\nu_\mu) + 3p$	5.59	ptop8w utop08
	$W(\mu,\nu_\mu) + \geq 4p$	1.03	ptop9w utop09
	$W(\tau,\nu_\tau) + 0p$	1800	utopw0 utop10
	$W(\tau,\nu_\tau) + 1p$	225	utopw1 utop11
	$W(\tau,\nu_\tau) + 2p$	35.4	utop2w utop12
	$W(\tau,\nu_\tau) + 3p$	5.60	utop3w utop13
	$W(\tau,\nu_\tau) + \geq 4p$	1.03	utop4w utop14
$W + b\bar{b}$	$W(e,\nu_e) + b\bar{b} + 0p$	2.98	btop0w btop00
	$W(e,\nu_e) + b\bar{b} + 1p$	0.888	btop1w btop01
	$W(e,\nu_e) + b\bar{b} + \geq 2p$	0.287	btop2w btop02
	$W(\mu,\nu_\mu) + b\bar{b} + 0p$	2.98	btop5w btop05
	$W(\mu,\nu_\mu) + b\bar{b} + 1p$	0.889	btop6w btop06
	$W(\mu,\nu_\mu) + b\bar{b} + \geq 2p$	0.286	btop7w btop07
	$W(\tau,\nu_\tau) + b\bar{b} + 0p$	2.98	dtop0w btop10
	$W(\tau,\nu_\tau) + b\bar{b} + 1p$	0.888	dtop1w btop11
	$W(\tau,\nu_\tau) + b\bar{b} + \geq 2p$	0.286	dtop2w btop12

Table 5.7: The sample identifications and relative cross sections for the $W + c/c\bar{c}$ samples. All samples were generated using ALPGEN + PYTHIA. In this table, p stands for parton, which means light-flavored quark (u, d, or s) here.

MC Sample Name	Process	Relative Cross Section (pb^{-1})	Sample IDs
$W + c/c\bar{c}$	$W(e,\nu_e) + c\bar{c} + 0p$	5.00	`ctop0w btop15`
	$W(e,\nu_e) + c\bar{c} + 1p$	1.79	`ctop1w btop16`
	$W(e,\nu_e) + c\bar{c} + \geq 2p$	0.628	`ctop2w btop17`
	$W(\mu,\nu_\mu) + c\bar{c} + 0p$	5.00	`ctop5w btop20`
	$W(\mu,\nu_\mu) + c\bar{c} + 1p$	1.79	`ctop6w btop21`
	$W(\mu,\nu_\mu) + c\bar{c} + \geq 2p$	0.628	`ctop7w btop22`
	$W(\tau,\nu_\tau) + c\bar{c} + 0p$	5.00	`etopw0 btop25`
	$W(\tau,\nu_\tau) + c\bar{c} + 1p$	1.80	`etopw1 btop26`
	$W(\tau,\nu_\tau) + c\bar{c} + \geq 2p$	0.628	`etopw2 btop27`
	$W(e,\nu_e) + c + 0p$	17.1	`stopw0 otopwd`
	$W(e,\nu_e) + c + 1p$	3.39	`stopw1 otopwe`
	$W(e,\nu_e) + c + 2p$	0.507	`stopw2 otopwf`
	$W(e,\nu_e) + c + \geq 3p$	0.0830	`stopw3 otopwg`
	$W(\mu,\nu_\mu) + c + 0p$	17.1	`stopw5 otopwh`
	$W(\mu,\nu_\mu) + c + 1p$	3.39	`stopw6 otopwi`
	$W(\mu,\nu_\mu) + c + 2p$	0.507	`stopw7 otopwj`
	$W(\mu,\nu_\mu) + c + \geq 3p$	0.0830	`stopw8 otopwk`
	$W(\tau,\nu_\tau) + c + 0p$	17.1	`stopwa otopwl`
	$W(\tau,\nu_\tau) + c + 1p$	3.39	`stopwb otopwm`
	$W(\tau,\nu_\tau) + c + 2p$	0.507	`stopwc otopwn`
	$W(\tau,\nu_\tau) + c + \geq 3p$	0.0830	`stopwd otopwo`

we need to understand the QCD backgrounds. Section 5.5 then explains how the W + jets and QCD backgrounds are normalized together.

5.4 QCD Background

All of the backgrounds that we have considered so far contain a W or a Z boson. The QCD background deals with events where a jet mismeasurement fakes a W decay signature and is therefore also known as the non-W background. It mainly comes from events with two jets where the energy of one jet is mismeasured and the other jet looks like an electron by leaving a track in the COT associated with an electromagnetic energy deposit [33]. This is one of the hardest backgrounds to estimate because we cannot generate an MC sample that properly describes mismeasurements in the detector. In the past, we would estimate the amount of QCD background from the data by constructing QCD ratios outside of the signal region and then extrapolate them into the signal region. Today, we use a method that is based on creating QCD templates from fake leptons. An extensive discussion on the advantages of this technique appears in [33]. The fake lepton templates are different for each lepton type, so let us consider them one by one:

5.4.1 Fake CEM Template

The template for fake central electrons is created by selecting data events from the `bhel` sample using the same selection criteria as for the data except that we change the definition of an electron. This is achieved by requiring the reverse of any two of the electron identification cuts shown in Sec. 3.2.1 [33]. This template is therefore known as the antielectron template and is orthogonal to the electron data.

5.4.2 Fake CMUP and CMX Templates

The template for fake CMUP (CMX) muons is generated by selecting data events from the `bhmu` sample, except that the isolation requirement in Sec. 3.2.3

(Sec. 3.2.4) is reversed. This template is therefore known as the non-isolated muon template. When we select the non-isolated muons, we remove any jet that falls within $\Delta R = 0.4$ of the non-isolated muon in order to prevent using the same object twice, once as the fake muon and once as a jet. Furthermore, we correct the $\not\!\!E_{\mathbf{T}}$ vector to account for the additional calorimeter energy associated with the non-isolated muon. The vector components are corrected as follows:

$$\not\!\!E_{Ti}^{\text{corrected}} = \not\!\!E_{Ti} - p_i(\text{muon}) + (E_{\text{HAD}} + E_{\text{EM}})\frac{p_i(\text{muon})}{p(\text{muon})} \tag{5.7}$$

where i stands for the x and y components of the $\not\!\!E_{\mathbf{T}}$ and $\mathbf{p}$(muon) vectors.

5.4.3 Fake PHX Template

The template for fake PHX electrons is generated from a jet-triggered data sample (`gjt1`) to which we apply our standard selection, except that we redefine the electron identification requirements to apply to jets. This means that every object that is identified as an electron is actually a jet. This template is known as the jet electron template. These are the requirements for a jet to be identified as an electron:

- $E_T(\text{jet}) > 20.0$ GeV
- $N(\text{jet tracks}) \geq 4$
- $0.8 < F_{\text{EM}} < 0.95$
- $1.2 < |\eta(\text{jet})| < 2.0$

where the electromagnetic fraction (F_{EM}) is defined as the fraction of electromagnetic energy in the combined electromagnetic and hadronic calorimeter, mathematically this looks as follows:

$$F_{\text{EM}} = \frac{E_{\text{EM}}}{E_{\text{EM}} + E_{\text{HAD}}} \tag{5.8}$$

5.4.4 Tagged Fake Templates

We now have fake templates for each of the lepton categories, so let us consider how we modify these templates for each tagging category. We use all events of each template for the pretag sample. For the 1S category, we only use events that pass the QCD veto (see Sec. 4.3.10) and that only contain one jet taggable by the Secondary Vertex Tagger (SecVtx). A SecVtx taggable jet is defined as a jet that contains at least two secondary vertex tracks. For the S+J and S+R categories, we only use events that contain at least one SecVtx taggable jets, and for the $\geq$2S category, we only use events that contain at least two SecVtx taggable jets

5.5 Normalization of the W + Jets and QCD Backgrounds

With the W + jets and QCD background shapes in hand (see Secs. 5.3 and 5.4), we can now determine the normalization for each background. The idea is to fit the W + jets and QCD background shapes to the data minus the MC backgrounds itemized in Sec. 5.2.

Let us define the following conventions: when we consider a distribution $g_j(x)$ from source j over a kinematic variable x, we refer to a specific bin in that distribution when we write a second subscript i; for example, $g_{WW,i}(\phi_{\text{lep}})$ refers to bin i of the WW distribution of ϕ_{lep}. When we omit the second index, we refer to the entire distribution, for example $g_{t\bar{t}}(\eta_{b1})$ refers to the entire $t\bar{t}$ distribution of η_{b1}. When it is clear what kinematic variable is considered, we might drop the argument of g. We also define d to stand for g_{data} (and d_i for $g_{\text{data},i}$). Let us also define the number of events of source j that pass our selection cuts from Chap. 4 as N_j.

We fit the shapes as a function of $\not\!\!E_T$ because the QCD backgrounds are peaked at a lower $\not\!\!E_T$ than the W + jets backgrounds, so this provides a good separation variable. The QCD backgrounds are peaked at a lower $\not\!\!E_T$ because the $\not\!\!E_T$ is due to mismeasurement of the jets and not from a neutrino as in the W + jets backgrounds.

Here is the fit that we want to perform:

$$d(\not\!\!E_T) = p_{\rm QCD} g_{\rm QCD}(\not\!\!E_T) + p_W g_W(\not\!\!E_T) + g_{\rm MC}(\not\!\!E_T) \tag{5.9}$$

where $p_{\rm QCD}$ and p_W are the two free fit parameters, also known as strength factors, and g_W is short for $g_{W+\rm jets}$. The following section will explain in detail how this fit is performed.

5.5.1 Fitting the Background Models to Data

It is a fairly common problem in high energy physics to fit the sum of background models to data for a given kinematic distribution. In concrete terms, we subdivide a kinematic distribution into n bins and then investigate how to fit the sum of background templates $\{f_1, f_2, ..., f_n\}$ to the data $\{d_1, d_2, ..., d_n\}$. R. Barlow and C. Beeston introduce a method of performing this fit which incorporates the statistical fluctuations due to the finite statistics of the background samples [34]. To understand the fit, let us define and adopt some of their useful nomenclature. Let $f_i(p_1, p_2, ..., p_M)$ represent the predicted number of events in the bin, given by the strength factors p_j and the number of background events g_{ji} from source j in bin i:

$$f_i = \sum_{j=1}^{m} p_j g_{ji} \tag{5.10}$$

As mentioned above, we will perform this fit as a function of $\not\!\!E_T$ because it gives the best QCD/W separation. Since the QCD background is peaked in the low $\not\!\!E_T$ region, we do not apply the $\not\!\!E_T$ requirements from Table 3.1 for the purpose of this fit. Table 5.8 shows the fit ranges used for the different lepton categories. The sources in this analysis consist of three categories: QCD, W, and MC. Section 5.4 explains how the QCD template is created, Sec. 5.3 explains how the W template is created, and Sec. 5.2 explains how the MC template and normalization are determined. Since the normalization of the MC template is already determined, we do not need to fit it, so we set $p_{\rm MC} = 1.0$. This means that only p_W and $p_{\rm QCD}$ need to be determined by

Table 5.8: This table gives the $\not\!\!E_T$ values of the fitting ranges for the QCD fit.

Lepton Type	Fit Range Minimum (GeV)	Fit Range Maximum (GeV)
CEM	0	100
PHX	10	100
CMUP	0	100
CMX	0	100

the fitting algorithm. The fit is performed by maximizing a binned likelihood that is not only based on the Poisson fluctuations of the data, but also on the Poisson fluctuations of the finite number of background events in each bin [34]. The ROOT package `TFractionFitter` implements this technique.

We use this fitting method to determine the QCD normalization in all channels and the W normalization in the pretag channels. For the tagged categories, the fit is performed by fixing the W normalizations to the values that we will calculate in the next sections. In other words, p_W in Eq. (5.9) is fixed for the tagged fits. This fit is performed for each lepton category individually. Figures 5.1 and 5.2 show the results of the QCD fits for the two and three-jet samples.

The number of events in the double-tagged samples are sometimes too small to be able to perform a meaningful fit, so we implement a low-statistics fitting method for such samples. We perform the fit in the combined sample of all four tagging categories (≥2S, S+J, S+R, and 1S), known as ≥1S, and then extrapolate the number of QCD events into the double-tagged sample as follows:

$$N_{\rm QCD}^{\text{double tag}} = \frac{B^{\text{double tag}} + C^{\text{double tag}}}{B^{\geq 1\rm S} + C^{\geq 1\rm S}} N_{\rm QCD}^{\geq 1\rm S} \tag{5.11}$$

where B is the number of events that fail the $\not\!\!E_T$ requirement from Table 3.1 and C is the number of events that fail the isolation / E_T requirement from Secs. 3.2.1–3.2.4.

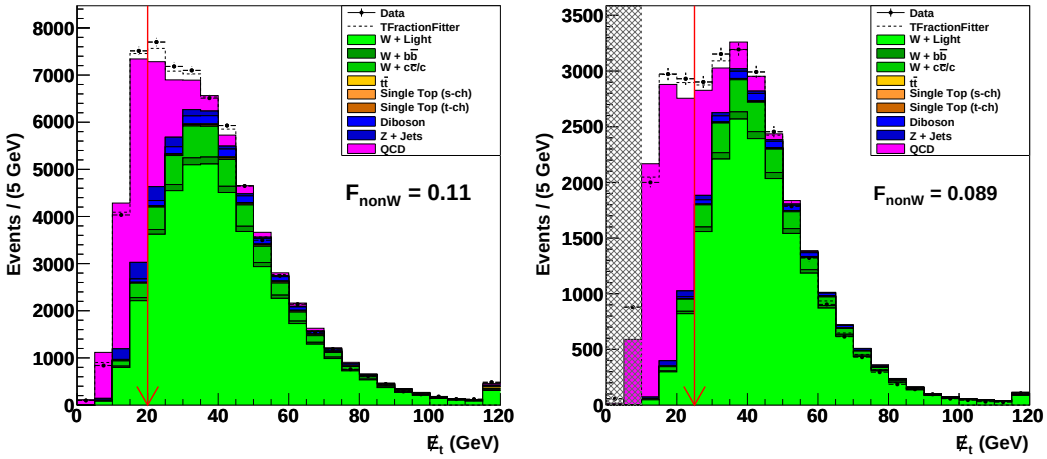

(a) CEM QCD Estimate

(b) PHX QCD Estimate

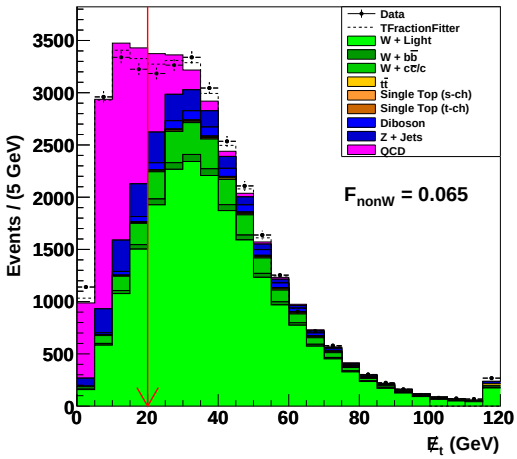

(c) CMUP QCD Estimate

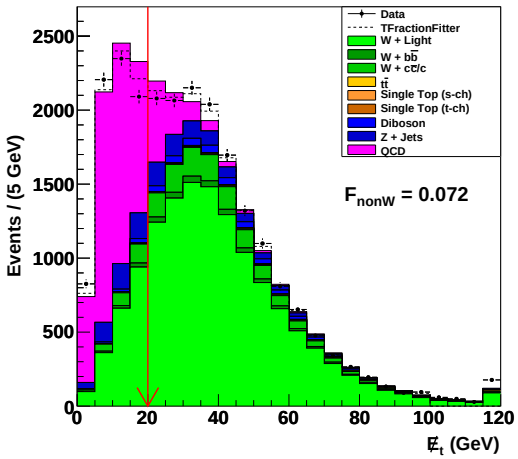

(d) CMX QCD Estimate

Figure 5.1: The QCD estimates for all lepton categories in the two-jet pretag sample. F_{nonW} is equivalent to the QCD fraction (F_{QCD}).

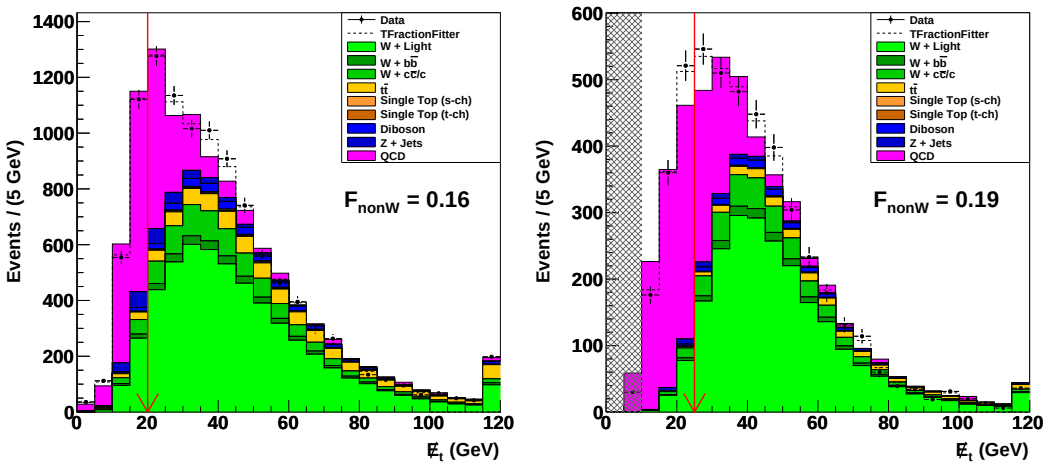

(a) CEM QCD Estimate

(b) PHX QCD Estimate

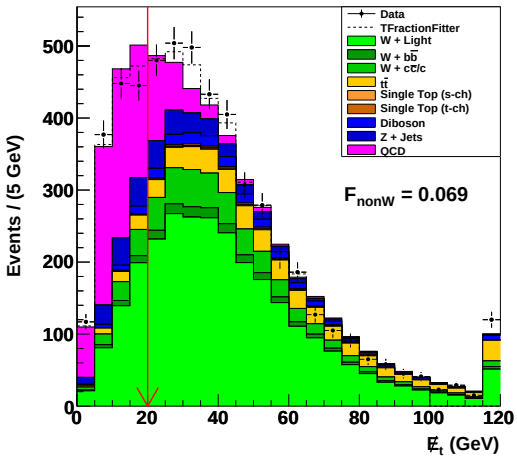

(c) CMUP QCD Estimate

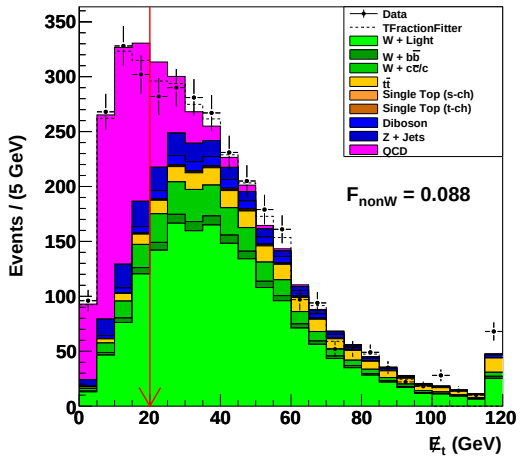

(d) CMX QCD Estimate

Figure 5.2: The QCD estimates for all lepton categories in the three-jet pretag sample. F_{nonW} is equivalent to the QCD fraction (F_{QCD}).

5.5.2 QCD Fraction

The QCD normalization can now be used to determine the QCD fraction in the data sample, which is defined as follows:

$$F_{\mathrm{QCD}} = \frac{\int_{\not\!\!E_{T\,\mathrm{min}}}^{\infty} p_{\mathrm{QCD}} g_{\mathrm{QCD}}(\not\!\!E_T) d\not\!\!E_T}{N_{\mathrm{data}}} \tag{5.12}$$

$\not\!\!E_{T\,\mathrm{min}}$ corresponds to the $\not\!\!E_T$ requirement from our object identification requirements (see Table 3.1), and N_{data} corresponds to the number of data events after application of the same $\not\!\!E_T$ requirement.

5.5.3 W + Jets

The QCD fraction from the pretag sample is the starting point for determining the W normalization in the tagged channels. First, let us estimate the number of W + jets events in the pretag sample:

$$\begin{aligned} N_{W+\mathrm{jets}} &= N_{data} - N_{QCD} - \sum_{j \in MC} N_j \\ &= N_{data} - F_{QCD} N_{data} - \sum_{j \in MC} N_j \end{aligned} \tag{5.13}$$

This means that the number of W + jets events is what remains when the QCD background and all of the MC-based backgrounds are subtracted from the number of data events. $N_{W+\mathrm{jets}}$ is used as the total normalization of the W + jets distributions in the pretag sample. However, when we consider the tagged samples, we need to consider what quarks the jets came from because they behave differently. We consider two general categories: heavy and light-flavored jets.

5.5.3.1. *W + Heavy-Flavored Jets* In order to calculate the number of W + HF events in the tagged sample, we first need to calculate the heavy flavor fraction ($f_{W+b\bar{b}}$ and $f_{W+c/c\bar{c}}$), the tagging efficiency ($\epsilon^{tag}_{W+b\bar{b}}$ and $\epsilon^{tag}_{W+c/c\bar{c}}$), and the K factor ($KF$). The heavy flavor fraction is the fraction of matched events in the total W + jets MC,

which consists of W + LF, $W + b\bar{b}$, and $W + c/c\bar{c}$. Matching refers to the process of matching detector-level jets to quarks from the observed particle branch (`obsp`). The observed particle branch, which only exists in MC samples, identifies the particles that are observed in our detector. For example, when we identify a jet using the identification requirements from Sec. 3.3.1, we can look in the `obsp` branch for a particle that is within $\Delta R = 0.4$ of the jet and then identify that particle's type. We are specifically interested in seeing whether one or more jets in an event match a bottom, charm, or light quark, in that order. Events that contain one or more jets matched to a bottom quark are considered matched to one or more bottom quarks. The heavy flavor content of the W + jets sample is studied in more detail in [35]. In this analysis, we consider two heavy flavor samples, $W + b\bar{b}$ and $W + c/c\bar{c}$, so we need to consider the following two heavy flavor fractions:

$$f_{W+b\bar{b}} = \frac{N^{\geq 1b}_{W+b\bar{b}} + N^{\geq 1b}_{W+c/c\bar{c}} + N^{\geq 1b}_{W+\mathrm{LF}}}{N_{W+b\bar{b}} + N_{W+c/c\bar{c}} + N_{W+\mathrm{LF}}} \tag{5.14}$$

$$f_{W+c/c\bar{c}} = \frac{N^{\geq 1c}_{W+b\bar{b}} + N^{\geq 1c}_{W+c/c\bar{c}} + N^{\geq 1c}_{W+\mathrm{LF}}}{N_{W+b\bar{b}} + N_{W+c/c\bar{c}} + N_{W+\mathrm{LF}}} \tag{5.15}$$

where $N^{\geq 1b}_{(\mathrm{sample})}$ and $N^{\geq 1c}_{(\mathrm{sample})}$ stand for the number of events matched to one or more bottom or charm quark in the sample. The tagging efficiencies for the $\geq$2S tagging category are defined as follows:

$$\epsilon^{\geq 2\mathrm{S}}_{W+b\bar{b}} = \frac{N^{\geq 1b,\geq 2\mathrm{S}}_{W+b\bar{b}} + N^{\geq 1b,\geq 2\mathrm{S}}_{W+c/c\bar{c}} + N^{\geq 1b,\geq 2\mathrm{S}}_{W+\mathrm{LF}}}{N^{\geq 1b}_{W+b\bar{b}} + N^{\geq 1b}_{W+c/c\bar{c}} + N^{\geq 1b}_{W+\mathrm{LF}}} \tag{5.16}$$

$$\epsilon^{\geq 2\mathrm{S}}_{W+c/c\bar{c}} = \frac{N^{\geq 1c,\geq 2\mathrm{S}}_{W+b\bar{b}} + N^{\geq 1c,\geq 2\mathrm{S}}_{W+c/c\bar{c}} + N^{\geq 1b,\geq 2\mathrm{S}}_{W+\mathrm{LF}}}{N^{\geq 1c}_{W+b\bar{b}} + N^{\geq 1c}_{W+c/c\bar{c}} + N^{\geq 1c}_{W+\mathrm{LF}}} \tag{5.17}$$

where $N^{\geq 2\mathrm{S}}$ is the number of events that are in the $\geq$2S tagging category. The calculations of the tagging efficiencies for S+J, S+R, and 1S follow in the same way by substituting the relevant tagging category above.

Table 5.9: The K factors that are used for this analysis [11].

	$W + b\bar{b}$	$W + c/c\bar{c}$
KF	1.4 ± 0.4	1.4 ± 0.4

Due to the low number of matched events in any one lepton category, the above fractions are determined from the combined TLEP sample and then applied to all four lepton categories. This is based on the assumption that the heavy flavor content is independent of the lepton category.

The K factor (KF) is the calibration factor of the heavy flavor fraction, and its calculation is performed in [11]. This factor is needed to correct our MC samples because the MC simulation models the gluon splitting incorrectly. It also corrects the MC samples for higher-order effects since we only use leading-order MC simulations [36]. Here is the definition of the K factor:

$$KF = \frac{f_{\text{data}}^{\geq 1b}}{f_{\text{MC}}^{\geq 1b}} \tag{5.18}$$

Table 5.9 gives the value that was calculated in [11] and that we will use in this analysis.

Now that we have defined all of the factors, we can estimate the number of events containing heavy-flavored jets in our sample. Here is how we do it for the $\geq$2S tagging category:

$$N_{W+b\bar{b}}^{\geq 2\text{S}} = N_{W+\text{jets}} \cdot KF \cdot f_{W+b\bar{b}} \cdot \epsilon_{W+b\bar{b}}^{\geq 2\text{S}} \tag{5.19}$$

$$N_{W+c/c\bar{c}}^{\geq 2\text{S}} = N_{W+\text{jets}} \cdot KF \cdot f_{W+c/c\bar{c}} \cdot \epsilon_{W+c/c\bar{c}}^{\geq 2\text{S}} \tag{5.20}$$

The number of events containing heavy-flavored jets are calculated in the same for the S+J, S+R, and 1S tagging categories by substituting the relevant tagging category above.

5.5.3.2. *W + Light-Flavored Jets / Mistags* The last background that we need to determine is the contamination of our tagged sample with jets that originate from light-flavored quarks. We estimate this by calculating the negative tag fraction in the W + LF MC sample as follows:

$$f_- = \frac{N_-}{N_{\text{total}}} \tag{5.21}$$

where (N_-) is the number of negatively tagged events in the W + LF MC sample and N_{total} is the total number of events in the W + LF MC sample. The number of light flavor jets in the data can then be calculated as follows:

$$N_{W+\text{LF}} = f_- \left(N_{W+\text{jets}} - N^{\text{pretag}}_{W+b\bar{b}} - N^{\text{pretag}}_{W+c/c\bar{c}} \right) \tag{5.22}$$

where $N^{\text{pretag}}_{W+b\bar{b}}$ and $N^{\text{pretag}}_{W+c/c\bar{c}}$ come from the pretag fit outlined in Sec. 5.5. We use negative tags to estimate the number of mistagged jets because they are a good indication of the number of positively tagged light-flavored quarks. The idea is that a light-flavored quark is equally likely to be tagged positively or negatively because of its short lifetime. A heavy-flavored quark, on the other hand, is very unlikely to be negatively tagged, so light- and heavy-flavored quarks make up the set of positively tagged jets. We can therefore use the number of negatively tagged jets to infer the number of light-flavored quarks in the positively tagged sample. The total number of negatively tagged jets in the W + LF sample are estimated with the use of three mistag matrices, which give the probability of negatively tagging a jet. Each tagging algorithm has its own mistag matrix. In this analysis, we use the Secondary Vertex Tagger (SecVtx) mistag matrix derived from 5.6 fb^{-1} of data [37] together with its asymmetry corrections [38], the Jet Probability Tagger (JetProb) mistag matrix derived from 5.6 fb^{-1} [39] together with an asymmetry correction factor of 1.27, and the Roma Neural Network Tagger (RomaNN) mistag matrix derived from 4.3 fb^{-1} [40]. The asymmetry correction factor accounts for the effect

that the number of negatively and positively tagged light-flavored jets is not exactly the same because of material interactions in the detector and long-lived particles within light jets [38].

The mistag matrices provide us with a mistag rate for each jet in an event. In order to count the total number of negatively tagged events (N_-) in a sample, we need to combine the jet mistag rates into a mistag probability for each event. The total number of negatively tagged events is then the sum of the per-event mistag probabilities for all events in the sample. We calculate a mistag probability for each tagging category. Let us define the following four probabilities:

- $r_{\mathrm{S}}(j)$: The probability that jet j is mistagged by SecVtx.
- $r_{\mathrm{J}}(j)$: The probability that jet j is mistagged by JetProb, but is not mistagged by SecVtx.
- $r_{\mathrm{R}}(j)$: The probability that jet j is mistagged by RomaNN. Ideally, we would use the probability that jet j is mistagged by RomaNN, but is not mistagged by either SecVtx or JetProb, but unfortunately such a mistag matrix has not been calculated yet.
- $r_{\mathrm{n}}(j)$: The probability that jet j is not mistagged by any tagger. Since there is no specific mistag matrix for this, we assume that $r_{\mathrm{n}}(j) \approx 1 - r_{\mathrm{R}}(j)$. The results are consistent within the systematic uncertainties if we would use $1 - r_{\mathrm{S}}(j)$ or $1 - r_{\mathrm{J}}(j)$.

The mistag probability calculations vary for each jet sample, so let us explain them individually:

- If the event contains exactly one jet, we only need the mistag probability for the 1S category:

$$P_{1\mathrm{S}} = r_{\mathrm{S}}(1) \tag{5.23}$$

- If the event contains exactly two jets, the mistag probabilities are given as follows:

$$P_{\geq 2S} = r_S(1)r_S(2) \quad (5.24)$$

$$P_{S+J} = r_S(1)r_J(2) + r_J(1)r_S(2) \quad (5.25)$$

$$P_{S+R} = r_S(1)r_R(2) + r_R(1)r_S(2) \quad (5.26)$$

$$P_{1S} = r_S(1)r_n(2) + r_n(1)r_S(2) \quad (5.27)$$

- If the event contains three or more jets, the mistag probabilities are given as follows:

$$\begin{aligned} P_{\geq 2S} &= r_S(1)r_S(2)r_S(3) + \\ &\quad r_S(1)r_S(2)r_n(3) + r_S(1)r_n(2)r_S(3) + r_n(1)r_S(2)r_S(3) \quad (5.28) \\ P_{S+J} &= r_S(1)r_J(2)r_n(3) + r_S(1)r_n(2)r_J(3) + r_n(1)r_S(2)r_J(3) + \\ &\quad r_J(1)r_S(2)r_n(3) + r_J(1)r_n(2)r_S(3) + r_n(1)r_J(2)r_S(3) \quad (5.29) \\ P_{S+R} &= r_S(1)r_R(2)r_n(3) + r_S(1)r_n(2)r_R(3) + r_n(1)r_S(2)r_R(3) + \\ &\quad r_R(1)r_S(2)r_n(3) + r_R(1)r_n(2)r_S(3) + r_n(1)r_R(2)r_S(3) \quad (5.30) \\ P_{1S} &= r_S(1)r_n(2)r_n(3) + r_n(1)r_S(2)r_n(3) + r_n(1)r_n(2)r_S(3) \quad (5.31) \end{aligned}$$

As mentioned before, we estimate N^- by summing the above probabilities over the W + LF sample without applying the heavy flavor filter.

5.6 Results of the Background Modeling

In this section, we will look at the results of the modeling described in the previous section. Tables 5.10 through 5.13 show the background estimates for the two and three-jet samples for the TLEP and PHX lepton categories. The background estimates for the control and signal samples for all tagging categories are shown in Figs. 5.3 and 5.4 for the TLEP and PHX lepton categories, respectively.

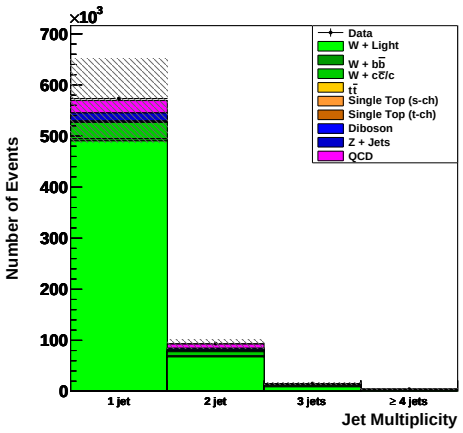

(a) Pretag

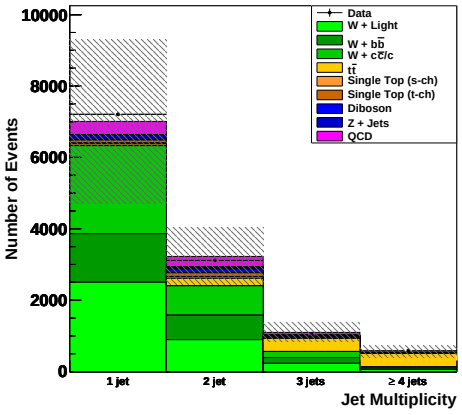

(b) 1S

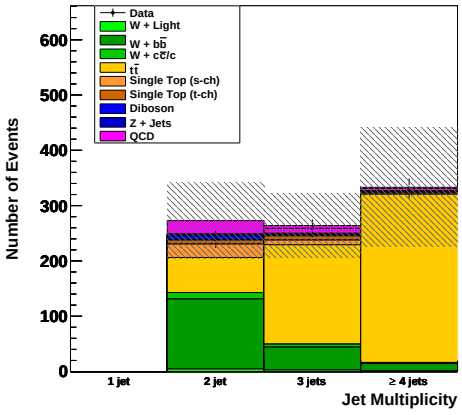

(c) $\geq$2S

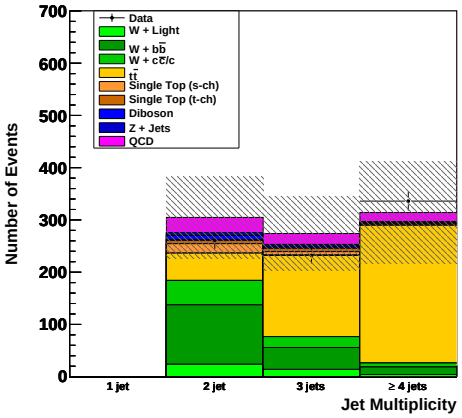

(d) S+J

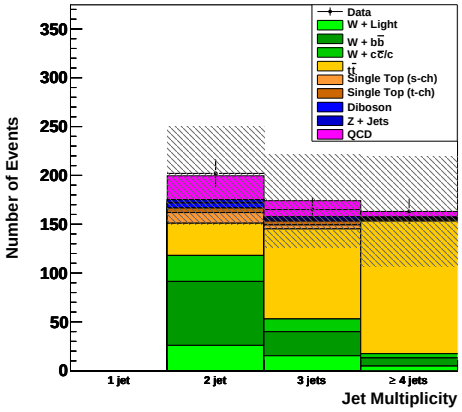

(e) S+R

Figure 5.3: The total background estimates for the tight lepton sample (TLEP) for the pretag category and all of the tagging categories.

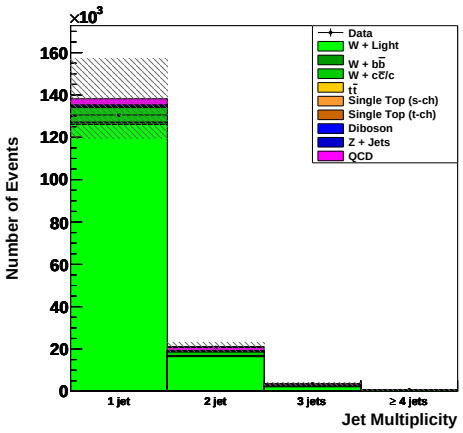

(a) Pretag

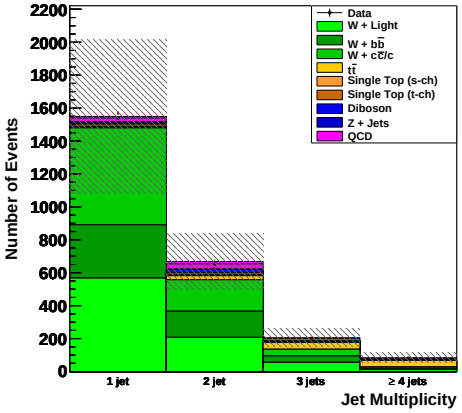

(b) 1S

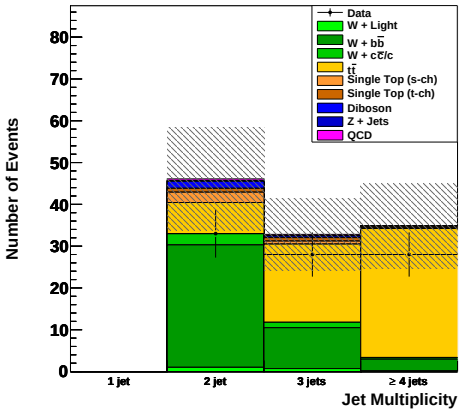

(c) ≥2S

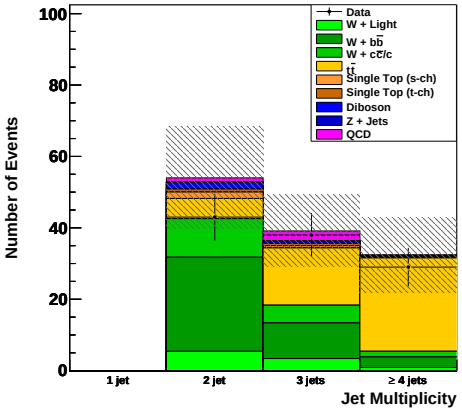

(d) S+J

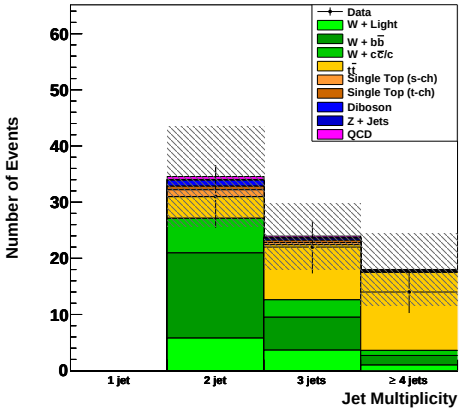

(e) S+R

Figure 5.4: The total background estimates for the PHX lepton sample for the pretag category and all of the tagging categories.

Table 5.10: The background estimation for the two-jet sample in the tight lepton category (TLEP).

	1S	≥2S	S+J	S+R
W + LF	891.98 ± 183.78	4.65 ± 1.94	23.65 ± 8.32	25.87 ± 5.20
$W + b\bar{b}$	686.57 ± 196.73	126.55 ± 36.52	113.85 ± 32.61	65.52 ± 18.80
$W + c/c\bar{c}$	823.86 ± 236.07	11.61 ± 3.35	46.70 ± 13.38	26.65 ± 7.65
$t\bar{t}$	209.87 ± 27.57	63.33 ± 10.32	52.19 ± 7.62	32.94 ± 5.08
Single Top (s-ch)	51.39 ± 6.75	24.35 ± 3.97	18.18 ± 2.65	10.95 ± 1.69
Single Top (t-ch)	102.19 ± 13.42	7.27 ± 1.19	7.37 ± 1.08	4.66 ± 0.72
Diboson	108.38 ± 11.29	7.18 ± 1.02	8.34 ± 1.02	5.20 ± 0.69
Z + jets	57.98 ± 7.97	3.62 ± 0.61	5.61 ± 0.85	3.34 ± 0.53
Non-W QCD	293.48 ± 117.39	24.27 ± 9.71	28.89 ± 11.56	24.46 ± 9.78
Total Background	3225.68 ± 800.98	272.83 ± 68.61	304.80 ± 79.08	199.58 ± 50.15
WH Signal	6.86 ± 0.68	3.33 ± 0.46	2.45 ± 0.29	1.48 ± 0.19
Observed Events	3114	239	261	202

Table 5.11: The background estimation for the two-jet sample in the PHX lepton category.

	1S	≥2S	S+J	S+R
W + LF	207.43 ± 40.49	1.00 ± 0.40	5.40 ± 1.66	5.79 ± 1.10
$W + b\bar{b}$	158.93 ± 46.13	29.30 ± 8.52	26.35 ± 7.57	15.17 ± 4.38
$W + c/c\bar{c}$	190.71 ± 55.35	2.69 ± 0.78	10.81 ± 3.11	6.17 ± 1.78
$t\bar{t}$	24.74 ± 3.44	7.46 ± 1.24	5.66 ± 0.84	3.85 ± 0.60
Single Top (s-ch)	5.86 ± 0.81	2.47 ± 0.41	1.81 ± 0.27	1.23 ± 0.19
Single Top (t-ch)	11.76 ± 1.63	0.93 ± 0.16	0.83 ± 0.12	0.63 ± 0.10
Diboson	19.44 ± 2.21	1.68 ± 0.25	1.80 ± 0.22	1.08 ± 0.15
Z + jets	2.72 ± 0.39	0.11 ± 0.02	0.15 ± 0.02	0.12 ± 0.02
Non-W QCD	47.03 ± 18.81	0.47 ± 0.47	1.19 ± 0.47	0.52 ± 0.52
Total Background	668.62 ± 169.27	46.09 ± 12.24	54.00 ± 14.29	34.56 ± 8.85
WH Signal	0.78 ± 0.08	0.34 ± 0.05	0.24 ± 0.03	0.15 ± 0.02
Observed Events	654	33	43	31

Table 5.12: The background estimation for the three-jet sample in the tight lepton category.

	1S	≥2S	S+J	S+R
W + LF	227.91 ± 39.92	2.96 ± 1.09	13.84 ± 3.90	15.24 ± 2.65
$W + b\bar{b}$	163.52 ± 52.36	41.14 ± 12.47	41.96 ± 12.89	24.63 ± 7.77
$W + c/c\bar{c}$	171.03 ± 54.76	5.43 ± 1.65	20.82 ± 6.39	13.07 ± 4.12
$t\bar{t}$	367.09 ± 71.23	179.66 ± 33.70	156.05 ± 28.61	92.25 ± 18.87
Single Top (s-ch)	14.41 ± 2.80	8.45 ± 1.59	6.66 ± 1.22	4.02 ± 0.82
Single Top (t-ch)	24.87 ± 4.83	7.64 ± 1.43	6.44 ± 1.18	3.96 ± 0.81
Diboson	24.92 ± 4.41	2.21 ± 0.38	3.72 ± 0.61	1.95 ± 0.37
Z + jets	16.79 ± 3.33	2.31 ± 0.44	3.56 ± 0.67	2.37 ± 0.49
Non-W QCD	86.08 ± 34.43	14.06 ± 5.62	20.99 ± 14.69	16.62 ± 11.64
Total Background	1096.61 ± 268.06	263.87 ± 58.38	274.04 ± 70.17	174.11 ± 47.54
WH Signal	1.55 ± 0.27	0.92 ± 0.15	0.72 ± 0.12	0.40 ± 0.07
Observed Events	1040	259	232	165

Table 5.13: The background estimation for the three-jet sample in the PHX lepton category.

	1S	≥2S	S+J	S+R
W + LF	55.79 ± 9.60	0.70 ± 0.25	3.39 ± 0.89	3.64 ± 0.63
$W + b\bar{b}$	38.90 ± 12.97	9.79 ± 3.15	9.98 ± 3.11	5.86 ± 1.82
$W + c/c\bar{c}$	40.68 ± 13.56	1.29 ± 0.42	4.95 ± 1.54	3.11 ± 0.96
$t\bar{t}$	41.03 ± 8.82	18.71 ± 4.03	16.05 ± 3.06	9.81 ± 1.92
Single Top (s-ch)	1.51 ± 0.32	0.72 ± 0.15	0.62 ± 0.12	0.38 ± 0.08
Single Top (t-ch)	2.73 ± 0.59	0.83 ± 0.18	0.65 ± 0.12	0.41 ± 0.08
Diboson	4.01 ± 0.80	0.39 ± 0.08	0.65 ± 0.11	0.35 ± 0.06
Z + jets	1.36 ± 0.30	0.12 ± 0.03	0.15 ± 0.03	0.08 ± 0.02
Non-W QCD	19.40 ± 7.76	0.27 ± 0.27	2.68 ± 1.07	0.31 ± 0.31
Total Background	205.41 ± 54.72	32.82 ± 8.56	39.13 ± 10.07	23.96 ± 5.86
WH Signal	0.17 ± 0.03	0.09 ± 0.02	0.07 ± 0.01	0.04 ± 0.01
Observed Events	201	28	38	22

CHAPTER SIX

Data Analysis

6.1 Introduction

In this chapter we will analyze the composition of the data in order to identify *WH* signal events. In Chap. 5, we detailed the background composition of our data sample, so we will begin this chapter by describing how we model *WH* signal. With the signal template in hand, we can proceed to separate background-like events from signal-like events. In the two-jet sample, we employ a Bayesian Neural Network, which has proven effective in separating signal-like events from background-like events in the past. In the three-jet sample, we will introduce a new technique of forming a multijet mass to discriminate signal events from background events.

6.2 WH Signal Modeling

As discussed in Sec. 1.5, the current theory does not predict the mass of the Higgs boson, so we have to model the Higgs signal separately for each possible Higgs mass. We also saw in Sec. 1.5 that this analysis is most sensitive for a Higgs boson within the mass range of 100 to 150 GeV/c^2. We model the Higgs signal in 5 GeV/c^2 increments, so we will create signal templates for the following ten Higgs mass points: 100, 105, 110, 115, 120, 125, 130, 135, 140, 145, and 150 GeV/c^2. The *WH* signal template for each mass point is modeled in the same way as the MC-based backgrounds described in Sec. 5.2 using the cross sections, branching ratios, and samples given in Table 6.1. The cross sections in Table 6.1 are calculated by taking the product of each Higgs boson production cross section and its *WH* decay branching ratio from Table 1.3. The W branching ratio in Table 6.1 is necessary

because the WH MC samples were generated exclusively with leptonic W decay modes.

Table 6.1: WH MC sample information. The cross section is calculated by taking the product of the Higgs boson production cross section and its WH decay branching ratio from Table 1.3. All samples are generated using PYTHIA.

Higgs Mass (GeV/c^2)	WH Cross Section (fb)	W Branching Ratio	Sample ID
100	234.48	0.324	`chgt7a`
105	195.16	0.324	`chgt7b`
110	160.90	0.324	`chgt7c`
115	130.87	0.324	`chgt7d`
120	103.99	0.324	`chgt7e`
125	80.35	0.324	`chgt7f`
130	59.82	0.324	`chgt7g`
135	42.78	0.324	`chgt7h`
140	29.17	0.324	`chgt7i`
145	18.82	0.324	`chgt7j`
150	11.24	0.324	`chgt7k`

6.3 Two-Jet Sample

For the two-jet sample, we employ a Bayesian Neural Network (BNN) to separate signal events from background events [41]. The BNN calculates an output value for each event based on the values of that event's kinematic variables. This output is a real numeric value in the range between zero and one. An output close to zero indicates that the event is likely to be a background event, whereas an output close to one indicates that the event is likely to be a signal event.

In this analysis, we use a different network for each one of the ten mass points and three for the different tagging categories, so we use a total of thirty networks. We use one set of networks for the $\geq$2S tagging category, another set for the 1S tagging category, and a third set for both the S+J and S+R tagging categories. All of the networks have been trained for a data sample corresponding to an integrated lumi-

nosity of 4.3 fb^{-1} and have been used in a previous WH search [41]. Table 6.2 shows the kinematic variables that are used as inputs for the different tagging categories.

Table 6.2: The kinematic inputs for the three different categories of networks. The inputs are sorted in order of importance within the network with the most important variable on top.

$\geq$2S	S+J and S+R	1S
M_{jj}	M_{jj}	M_{jj}
p_T imbalance	$\sum E_T$(loose jets)	$\sum E_T$(loose jets)
$M_{\ell\nu j}^{\max}$	$q_{\text{lep}}\eta_{\text{lep}}$	$q_{\text{lep}}\eta_{\text{lep}}$
$q_{\text{lep}}\eta_{\text{lep}}$	$M_{\ell\nu j}^{\min}$	$p_T(W)$
$\sum E_T$(loose jets)	H_T	H_T
$p_T(W)$	$p_T(W)$	$\not{E}_T$
H_T	$\not{E}_T$	p_T imbalance

The kinematic variables in Table 6.2 are defined as follows:

- M_{jj} is the reconstructed dijet mass of the two jets. This is the most sensitive discrimination variable in this analysis, so we further improve its resolution by applying another neural network to correct the b-jet energies [42].
- p_T imbalance is defined as p_T(jet 1) + p_T(jet 2) + p_T(lepton) – $\not{E}_T$.
- $M_{\ell\nu j}^{\max}$ and $M_{\ell\nu j}^{\min}$ are the reconstructed masses from the lepton, neutrino ($\not{E}_T$), and one jet. Since there are two jets, there are two possible values for this mass, which we label as max and min corresponding to the larger and smaller value, respectively. This variable is used to discriminate WH events from top quark events, since the top quark can decay into one W boson and one bottom quark.
- $q_{\text{lep}}\eta_{\text{lep}}$ is the product of the charge and the η angle of the lepton.
- $p_T(W)$ is the transverse momentum of the reconstructed W boson.

- $\sum E_T$(loose jets) is the sum of all the loose jets' E_T. A loose jet is defined as a jet that fails at least one of our two jet requirements on E_T and η from Sec. 3.3.1 but passes both of the following two requirements:
  - Jet energy corrected $E_T > 12.0$ GeV
  - $|\eta_{\text{detector}}| < 2.4$
- H_T is the scalar sum of all transverse energies and is defined as E_T(jet 1) + E_T(jet 2) + p_T(lepton) + $\not\!\!E_T$.

Figures 6.1 through 6.4 show all of the kinematic input variables for the BNN for the pretag sample and each of the lepton categories. We can see that our backgrounds model the data well. Also note the superimposed red line for the *WH* signal at a mass point of 115 GeV/c^2, which has been scaled up by 100 to make its shape visible.

6.3.1 Two-Jet Discriminants

Figures 6.5 through 6.8 show the outputs of the $m_H = 115$ GeV/c^2 BNN with the *WH* signal scaled by a factor of 10. We use these templates in Chap. 8 to calculate how much *WH* signal is in our data. The effectiveness of the BNN in separating background events (BNN output = 0) from signal events (BNN output = 1) is clearly seen in the right-hand plots with a logarithmic scale.

6.4 Three-Jet Sample

In this section, we discuss a novel technique to improve discrimination of signal events in the three-jet sample. While we search for a *WH* decay signature that includes a bottom and an antibottom quark, it is possible that one of those quarks radiates a very energetic gluon that is identified as a jet, yielding an event with three jets. In this case, the mass of the Higgs boson will be underestimated when

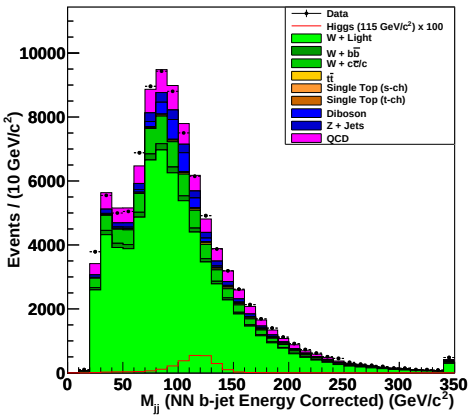

(a) M_{jj}

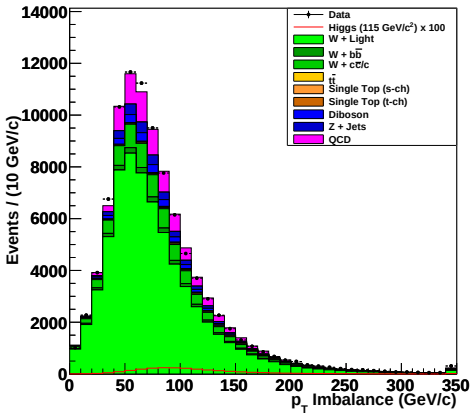

(b) p_T imbalance

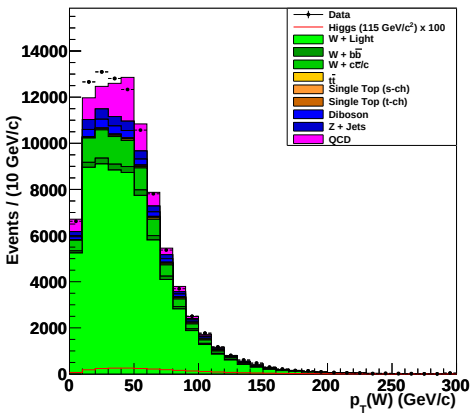

(c) $p_T(W)$

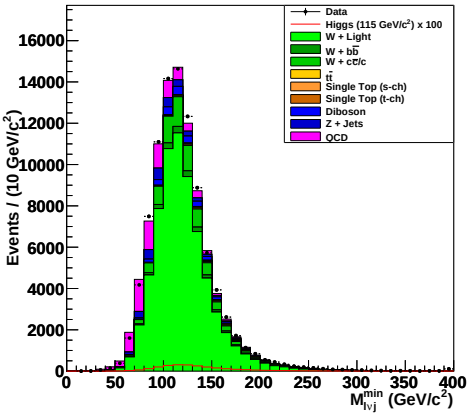

(d) $M^{\min}_{\ell\nu j}$

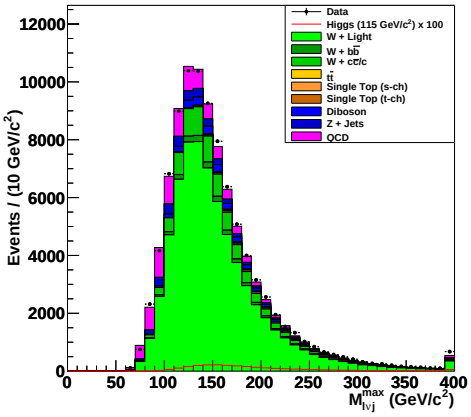

(e) $M^{\max}_{\ell\nu j}$

Figure 6.1: The BNN input variables for the tight leptons before any tagging requirement is applied. The WH ($m_H = 115$ GeV/c^2) signal has been scaled up by a factor of 100 and superimposed on the plots in red.

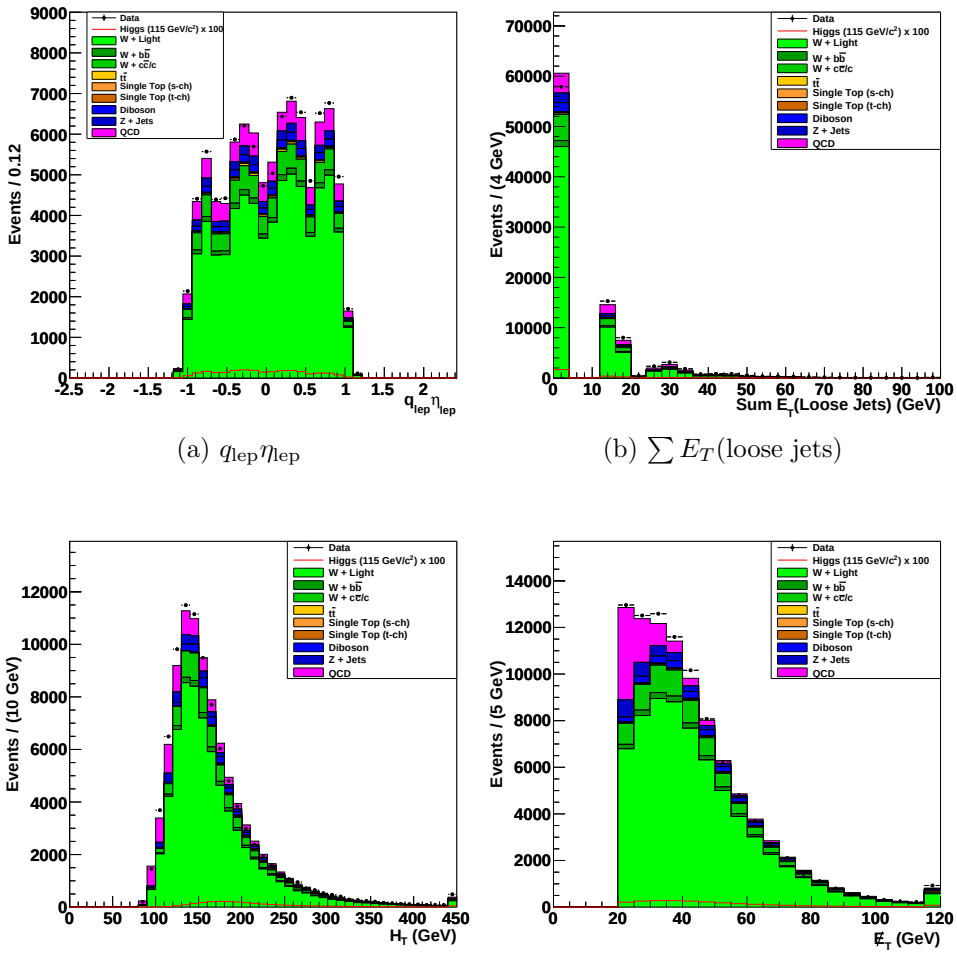

(a) $q_{\text{lep}}\eta_{\text{lep}}$ (b) $\sum E_T(\text{loose jets})$

(c) H_T (d) $\not\!\!E_T$

Figure 6.2: The BNN input variables for the tight leptons before any tagging requirement is applied. The WH ($m_H = 115$ GeV/c^2) signal has been scaled up by a factor of 100 and superimposed on the plots in red.

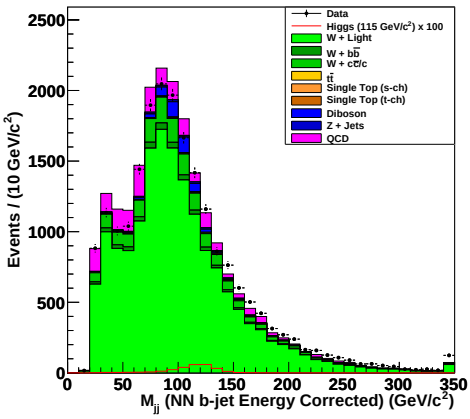

(a) M_{jj}

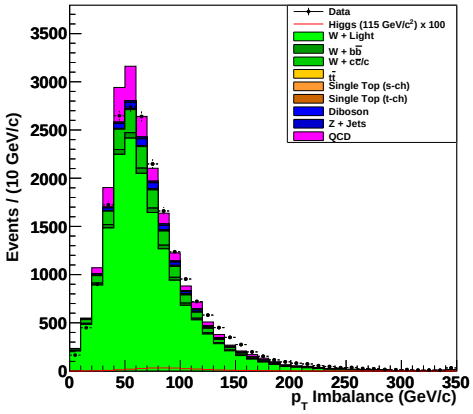

(b) p_T imbalance

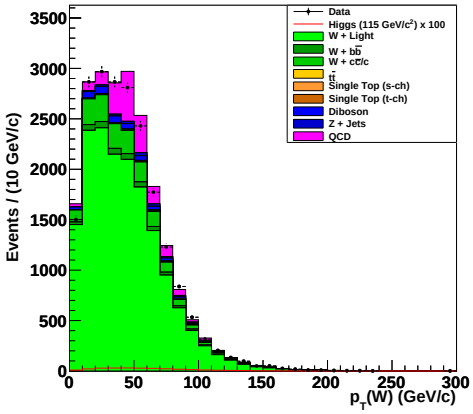

(c) $p_T(W)$

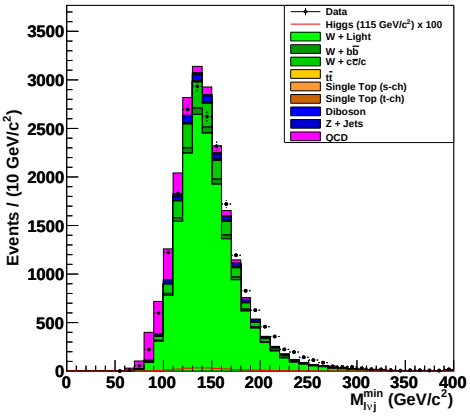

(d) $M^{\min}_{\ell\nu j}$

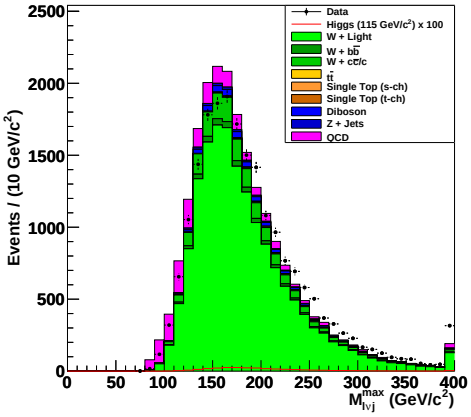

(e) $M^{\max}_{\ell\nu j}$

Figure 6.3: The BNN input variables for the PHX leptons before any tagging requirement is applied. The WH ($m_H = 115$ GeV/c^2) signal has been scaled up by a factor of 100 and superimposed on the plots in red.

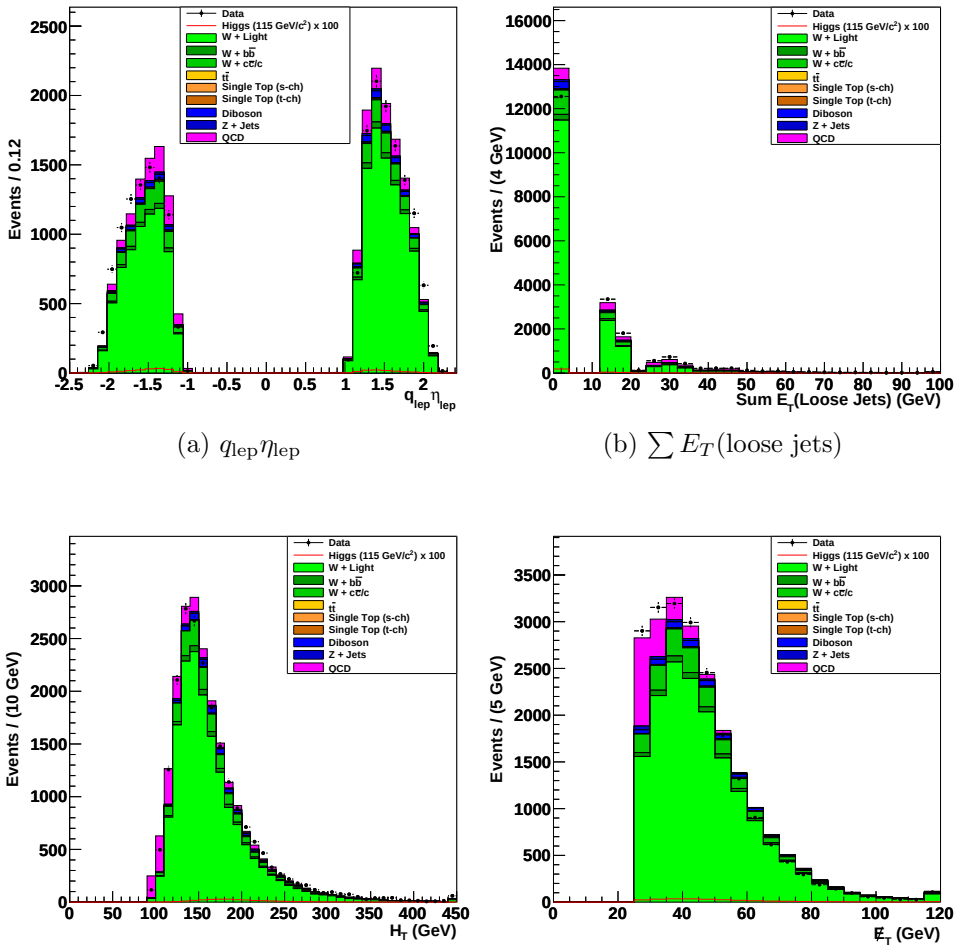

(a) $q_{\text{lep}}\eta_{\text{lep}}$ (b) $\sum E_T(\text{loose jets})$

(c) H_T (d) $\not\!\!E_T$

Figure 6.4: The BNN input variables for the PHX leptons before any tagging requirement is applied. The WH ($m_H = 115$ GeV/c^2) signal has been scaled up by a factor of 100 and superimposed on the plots in red.

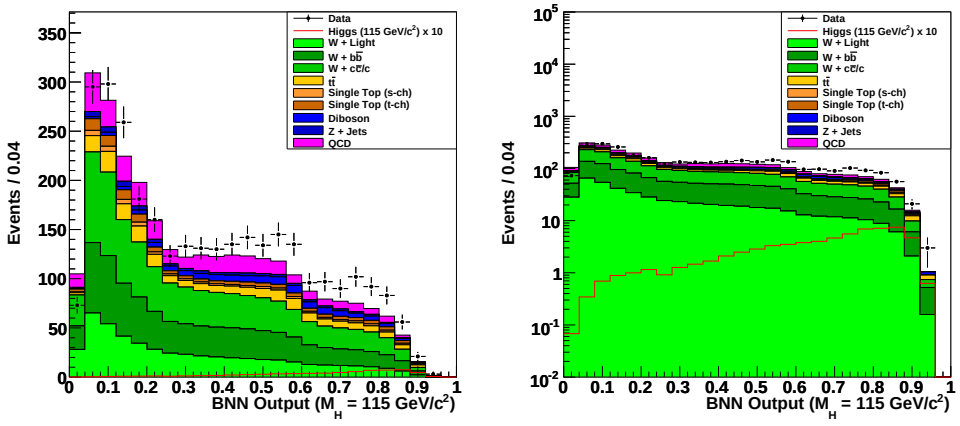

(a) Tight Leptons

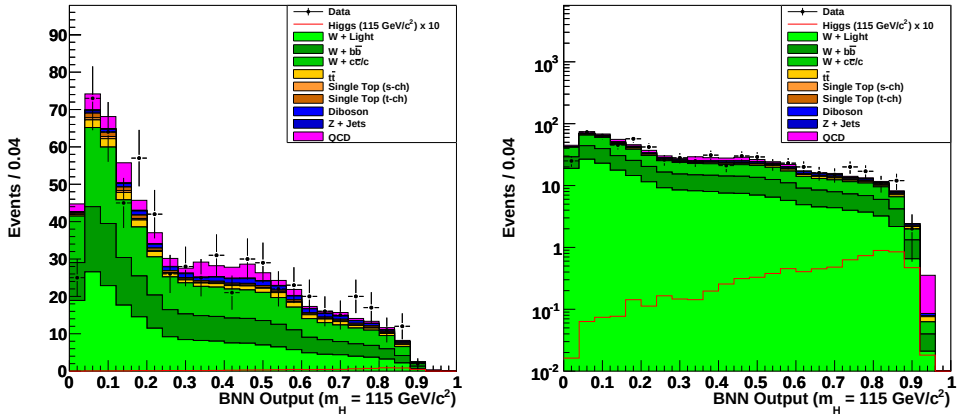

(b) PHX Leptons

Figure 6.5: The output distributions for the 1S $m_H = 115$ GeV/c^2 BNN for the tight and PHX leptons. The left plots have a linear scale and the right plots a logarithimic scale. The superimposed WH ($m_H = 115$ GeV/c^2) signal is scaled up by a factor of 10.

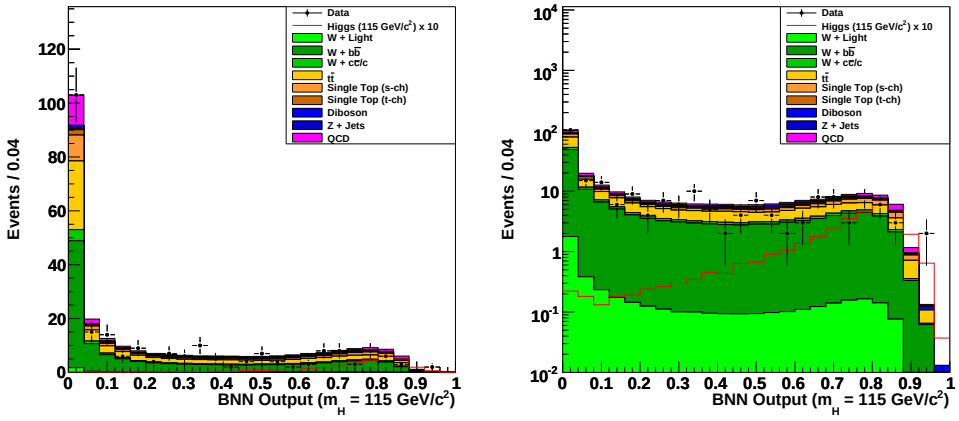

(a) Tight Leptons

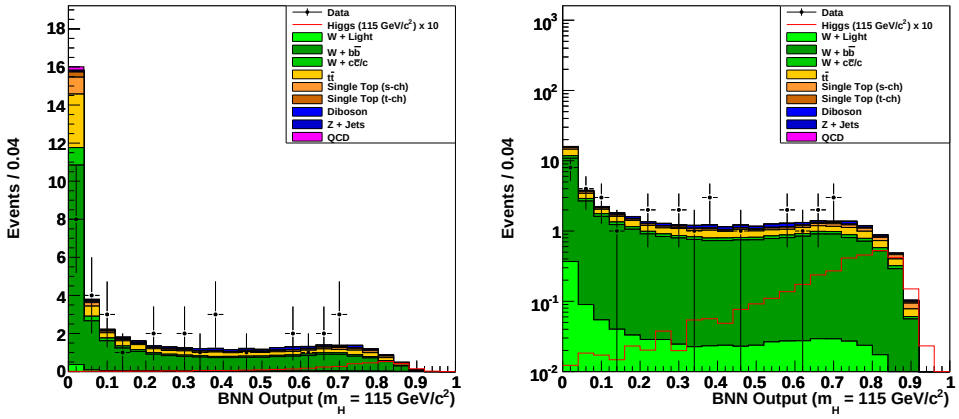

(b) PHX Leptons

Figure 6.6: The output distributions for the $\geq$2S $m_H = 115$ GeV/c^2 BNN for the tight and PHX leptons. The left plots have a linear scale and the right plots a logarithimic scale. The superimposed WH ($m_H = 115$ GeV/c^2) signal is scaled up by a factor of 10.

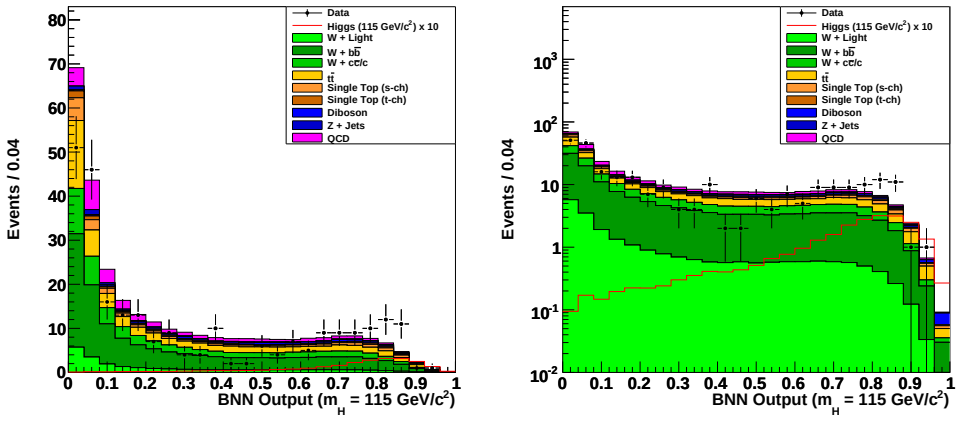

(a) Tight Leptons

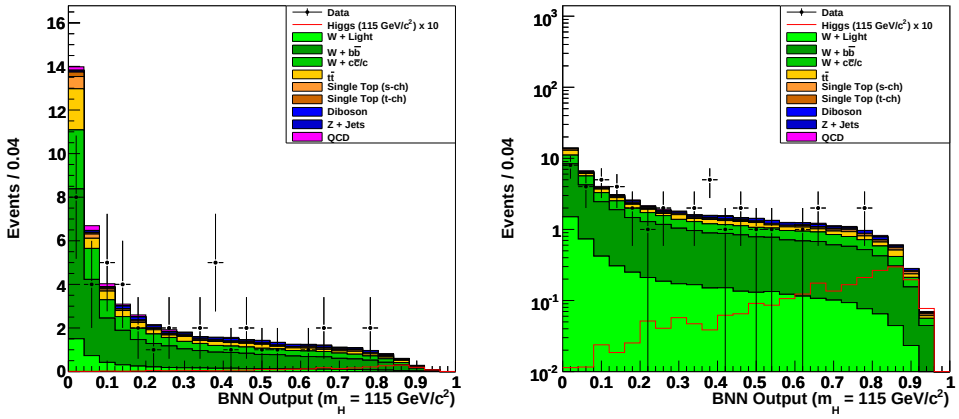

(b) PHX Leptons

Figure 6.7: The output distributions for the S+J $m_H = 115$ GeV/c^2 BNN for the tight and PHX leptons. The left plots have a linear scale and the right plots a logarithimic scale. The superimposed WH ($m_H = 115$ GeV/c^2) signal is scaled up by a factor of 10.

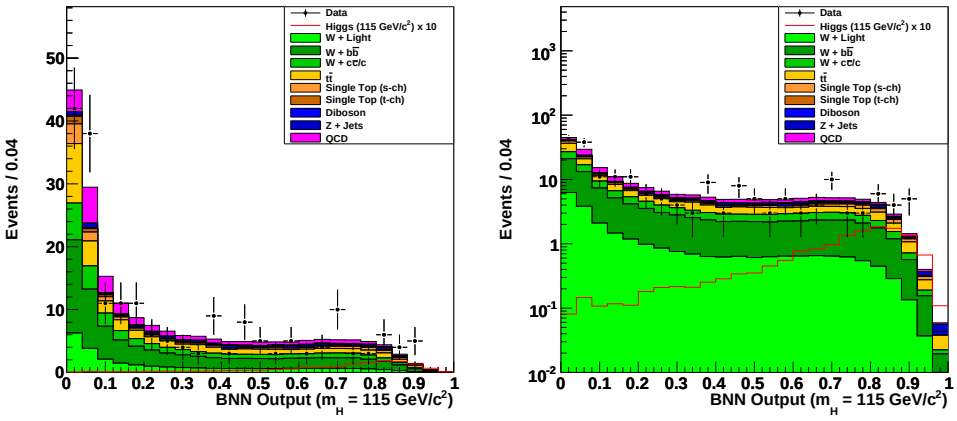

(a) Tight Leptons

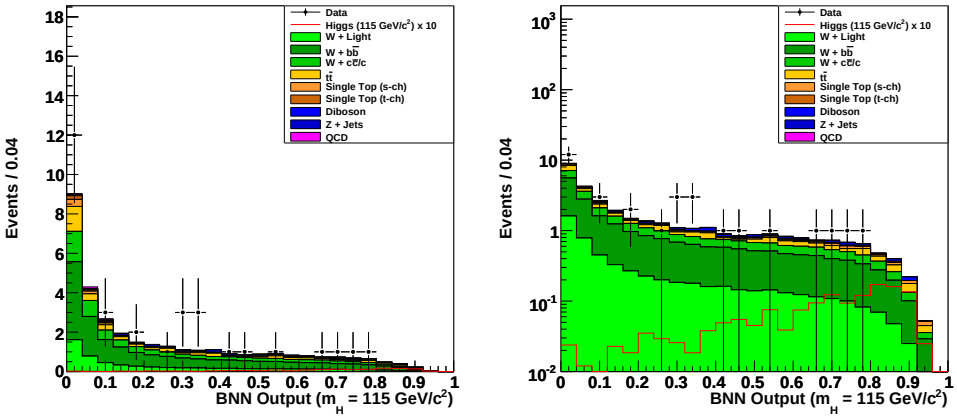

(b) PHX Leptons

Figure 6.8: The output distributions for the S+R $m_H = 115$ GeV/c^2 BNN for the tight and PHX leptons. The left plots have a linear scale and the right plots a logarithimic scale. The superimposed WH ($m_H = 115$ GeV/c^2) signal is scaled up by a factor of 10.

only two jets are used for the reconstruction. There are other cases in which a jet can be created in the underlying $p\bar{p}$ interaction or can radiate a gluon from the incoming quarks; in such cases, we would not want to use the third jet for the Higgs boson reconstruction. Below we explain how we first studied these different types of events and then developed a technique to identify an event based only on its kinematic attributes. At the end of the section we will show the three-jet sample's discriminatory variables together with their background modeling.

6.4.1 The Third Jet

In order to differentiate between three-jet events caused by a WH decay and those caused by other factors, we must examine the origin of the third jet in a given event. The first step is to investigate a WH Monte Carlo (MC) sample. In general, a MC sample is generated based on a decay process, and the MC program then propagates the resulting decay products as they travel through space and continue to yield more particles. This decay information is recorded in the MC sample for each event in a data structure called `hepg`, and we therefore refer to it as `hepg`-level information. This information is ideal for our purposes because we can trace each particle through its decay hierarchy to find its origin. We can therefore look at the simulated particles that make up all three jets and determine their origin.

6.4.2 Jet Clustering

Now that we can trace the decay hierarchy of an individual particle, we need to determine what particles make up a given jet. This is a very difficult question to answer since jet formation from initial quarks is not well understood. At CDF, we use clustering algorithms to form jets from the individual particles that we detect. We therefore need to cluster the individual `hepg` particles into jets, so that we can compare them to the detector-level jets. The detector-level jets are the jets clustered

from the detector response from the CDF simulation based on the MC simulation output (see Sec. 5.2). The jet clustering algorithm that we use for the general analysis is JetClu with a clustering parameter of $R = 0.4$ (see Sec. 3.3.1). One of the effects that might be responsible for the third jet is the choice of clustering algorithm, so for this study we employ a different clustering algorithm. We use the K_T algorithm, which is diagramed in Fig. 6.9 with a clustering parameter of $R = 0.4$. One of the advantages of the K_T algorithm over the JetClu algorithm is that it is simpler to implement.

There are three types of `hepg` particles, which are identified by the value of `hepg.stdHep` shown in parentheses: generator-level particles (3), intermediate particles (2), and final-state particles (1). Once the MC simulation declares a particle to be in its final state, it is not decayed any further. For this study, we use the final state particles as the initial set of preclusters for the K_T algorithm.

Let us now consider two specific events from the WH MC sample corresponding to a Higgs mass of 115 GeV/c^2 and compare the detector-level jets to the K_T-clustered jets. Figure 6.10 shows the jet positions of these two events, and we can see that the agreement is excellent. In this study, we only consider events for which each K_T-clustered jet falls within a $\Delta R = 0.4$ of a detector-level jet. This corresponds to approximately 70% of all events in the three-jet sample.

6.4.3 b-Fraction

We can now determine the origin of a given detector-level jet by looking at its corresponding K_T-clustered jet, which we created from the MC final-state particles. We can trace the origin of each particle to see where in the decay chain it was produced. Specifically, we can check whether the particles in a jet came from a b or $\bar{b}$ quark. If the majority of particles in a jet derive from a b or $\bar{b}$, the jet is identified as being the result of the Higgs boson decay. To make this identification,

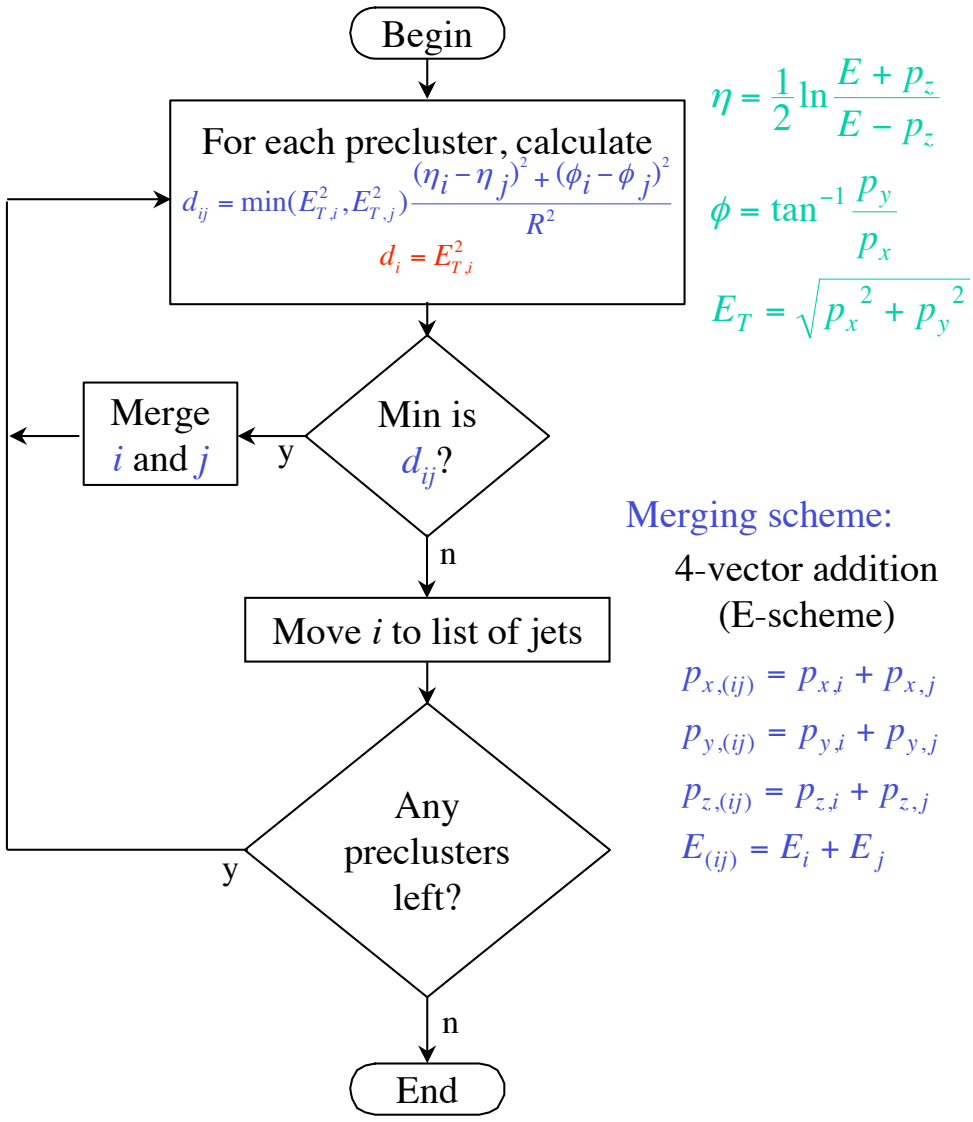

Figure 6.9: Simple Implementation of K_T Algorithm. This diagram shows the method for clustering particle-level jets that we use for the three-jet sample studies. The algorithm starts with a list of preclusters, `hepg` particles in our case, and then iteratively decides whether to merge two preclusters or declare a precluster a jet. The d_{ij} are determined for all pairs of preclusters, and the d_i are determined for every individual precluster. If the smallest of all d_{ij} and d_i is a specific d_i then precluster i is declared a jet; otherwise, precluster i and j of the smallest d_{ij} are merged into a new precluster. The equations used for merging two preclusters are given on the bottom right.

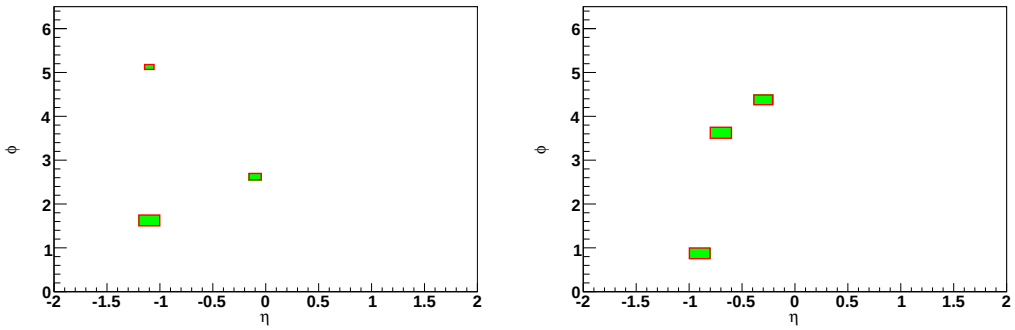

(a) Run 176696 Event 8 (b) Run 177314 Event 162

Figure 6.10: The positions in ϕ-η space of the jets in two different WH events. The green boxes show the position of the detector-level jets, and the red lines show the positions of the K_T-clustered jets. The size of the box represents the E_T of the jet; we only plotted jets with $E_T > 20$ GeV/c^2. The agreement between the detector-level jets and K_T-clustered jets is excellent.

we calculate the b-fraction (F_b) for each jet as follows:

$$F_b = \frac{\sum_{b \text{ particles}} E_T}{\sum_{\text{all particles}} E_T} \tag{6.1}$$

where b particles are the particles in a jet that contain a b or $\bar{b}$ in their decay hierarchy. This fraction provides a measure of how likely it is that a jet comes from a b decay, which in turn measures its likeliness of having come from a Higgs boson decay in our WH MC sample. In this analysis, we consider jets that have a b-fraction of more than 25% to come from a Higgs boson decay. Generally speaking, jets fall into two major groups, jets with F_b close to zero and jets with F_b close to one. This means that the exact value of F_b at which we assign a jet to come from a Higgs boson does not greatly impact this analysis. Figure 6.11 shows the values of F_b for each of the jets from Fig. 6.10 and indicates with a circle those jets that are considered to come from a Higgs boson decay (i.e. $F_b > 0.25$).

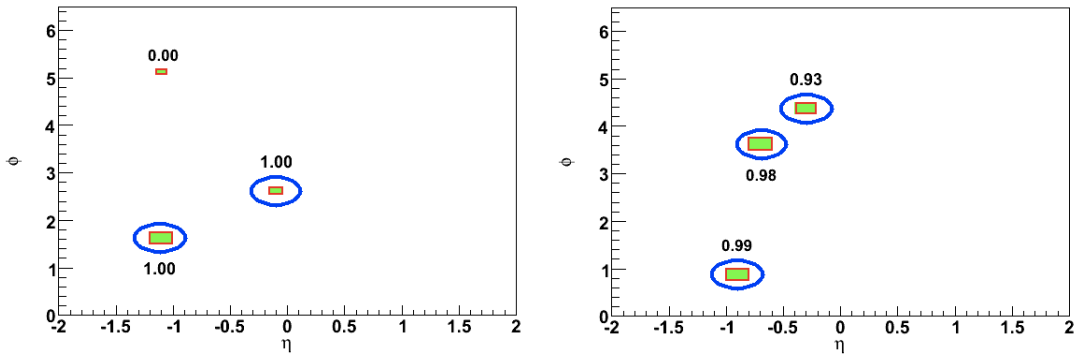

(a) Run 176696 Event 8 (b) Run 177314 Event 162

Figure 6.11: The positions in ϕ-η space of the jets for the same events as in Fig. 6.10 together with the b-fraction (F_b) of each event. The circles indicate jets that we consider to come from the Higgs decay (i.e. $F_b > 0.25$).

6.4.4 Higgs Boson Reconstruction

We see in Fig. 6.11 that the Higgs boson has to be reconstructed from different numbers of jets depending on the event. In this section, we will first compare the standard dijet reconstruction technique, which only uses the leading two jets, to our new multijet reconstruction method for the WH MC sample. We then proceed to find kinematic variables to help us determine which jets need to be used to reconstruct the Higgs boson.

In the WH MC sample, we can determine the b-fraction for every jet and then use the jets with $F_b > 0.25$ to reconstruct the Higgs boson mass, which will be referred to as the multijet mass. Mathematically, this is expressed as:

$$m_H^{\text{multijet}} = \left| \sum_i {p_i}^{\text{jet}} \right| \tag{6.2}$$

where ${p_i}^{\text{jet}}$ is the four-momentum of jet i and the sum is taken over all jets with $F_b > 0.25$. We only consider events that have at least two jets with $F_b > 0.25$ because we cannot properly reconstruct the Higgs boson from only one jet because the other jets from the Higgs boson most likely escaped our detection. Figure 6.12 shows the resultant distribution for the WH ($m_H = 115$ GeV/c^2) sample. For comparison, we

also show the mass distribution if only the two highest E_T jets are used to reconstruct the Higgs boson mass, which is known as the standard dijet mass. It is clear that the multijet mass distribution reflects the resonance better close to $m_H = 115$ GeV/c^2.

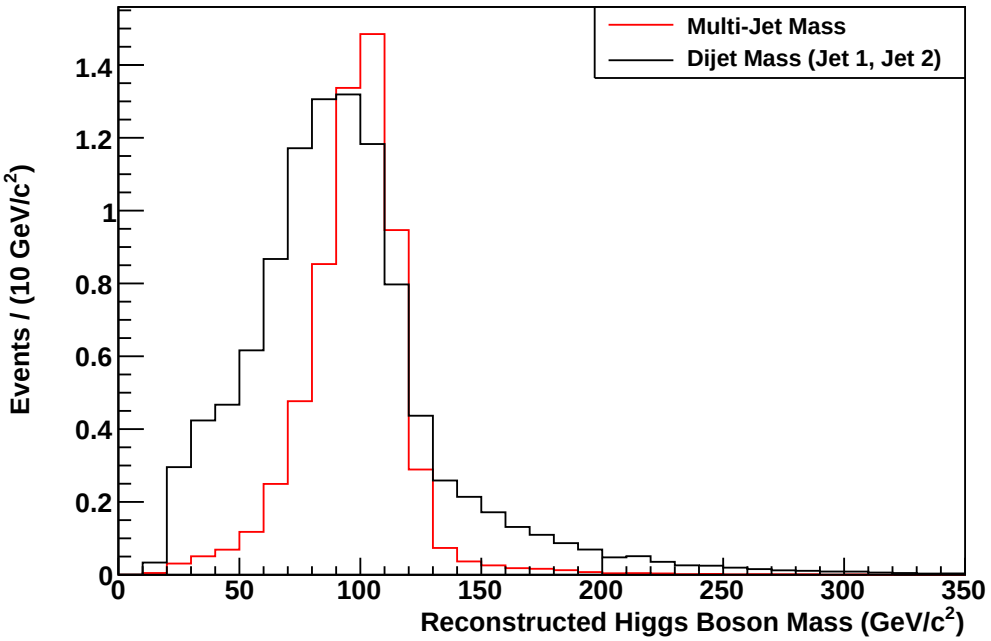

Figure 6.12: The reconstructed Higgs boson mass using two different reconstruction methods. The red distribution was generated with the multijet mass method described in Eq. (6.2). The black distribution shows the standard dijet mass for comparison. Both distributions come from the WH ($m_H = 115$ GeV/c^2) sample and include events in the three-jet sample that contain at least two Higgs-like jets before any lepton selection or tagging requirement.

Having demonstrated the value of using this multijet reconstruction technique, we next need to find a way to apply it to data events. Of course, the data do not contain any `hepg` level information, so we cannot calculate the b-fractions to determine which jets to use for the multijet mass. Instead we have to look to general kinematic variables to indicate which jets most likely come from the Higgs decay. In the three-jet sample, there are four ways to reconstruct a Higgs boson from the combination of at least two jets:

(1) Combine jets 1, 2, and 3 (39%).

(2) Combine jets 1 and 2 (32%) (commonly known as the standard dijet mass).

(3) Combine jets 1 and 3 (20%).

(4) Combine jets 2 and 3 (9%).

The percentages in parentheses indicate the fraction of simulated events that have at least two jets with b-fractions larger than 0.25. It is difficult to find discrimination variables to isolate the four kinds of events, so we will focus here on isolating events from the first two categories, which account for more than 70%. We have investigated many kinematic variables to discriminate category 1 from category 2 events and found that the following two provide the best separation:

- Leading Jet E_T (E_T(jet 1)): E_T of the highest E_T jet.
- $\sum \Delta R$: The sum of the separation in R between all three jet pairs:

$$\sum \Delta R = \Delta R(\mathrm{j}_1, \mathrm{j}_2) + \Delta R(\mathrm{j}_1, \mathrm{j}_3) + \Delta R(\mathrm{j}_2, \mathrm{j}_3) \tag{6.3}$$

  where j_i stands for jet i.

The distributions of these two kinematic variables are shown in Fig. 6.13. We can see that the distributions can be used to separate the two types of events. In order to enhance the discrimination power of the two variables, let us consider the $\sum \Delta R$ distributions for various leading jet E_T(jet 1) ranges. Fig. 6.14 shows these distributions for four E_T(jet 1) ranges. We can see that in the lowest E_T(jet 1) range (E_T(jet 1) $<$ 40 GeV) most events have three jets coming from the Higgs boson, which might be predicted intuitively because the jet energies are split among three jets rather than two. We also notice that events with three jets coming from the Higgs boson tend to have a low $\sum \Delta R$. This is because three jets coming from the

Higgs boson are expected to be more collimated than if only two jets came from the Higgs boson and the third jet came from elsewhere.

Using the four diagrams in Fig. 6.14, we can classify events into two categories based on how we combine the jets to reconstruct the Higgs boson; these categories correspond to items 1 and 2 in the above list. We can either reconstruct the Higgs boson mass using all three jets (m_{123}) or only the leading two jets (m_{12}). Here is how we define m_H^{multijet} based on the kinematic variables of the event:

- If $E_T(\text{jet 1}) < 40$ GeV, $m_H^{\text{multijet}} = m_{123}$.
- If $40 < E_T(\text{jet 1}) < 60$ GeV, and
  - $\sum \Delta R < 6.5$, $m_H^{\text{multijet}} = m_{123}$.
  - $\sum \Delta R > 6.5$, $m_H^{\text{multijet}} = m_{12}$.
- If $60 < E_T(\text{jet 1}) < 100$ GeV, and
  - $\sum \Delta R < 5.0$, $m_H^{\text{multijet}} = m_{123}$.
  - $\sum \Delta R > 5.0$, $m_H^{\text{multijet}} = m_{12}$.
- If $E_T(\text{jet 1}) > 100$ GeV, and
  - $\sum \Delta R < 3.5$, $m_H^{\text{multijet}} = m_{123}$.
  - $\sum \Delta R > 3.5$, $m_H^{\text{multijet}} = m_{12}$.

The $\sum \Delta R$ requirements are indicated with a red arrow in the four plots in Fig. 6.14. Figure 6.15 shows the reconstructed multijet mass (m_H^{multijet}) distribution for the data and the backgrounds, from which we can see that the backgrounds model the data well. The WH ($m_H = 115$ GeV/c^2) signal is superimposed and scaled up by a factor of 100. We can see that the signal distribution takes on the expected mass distribution and peaks at the modeled Higgs mass.

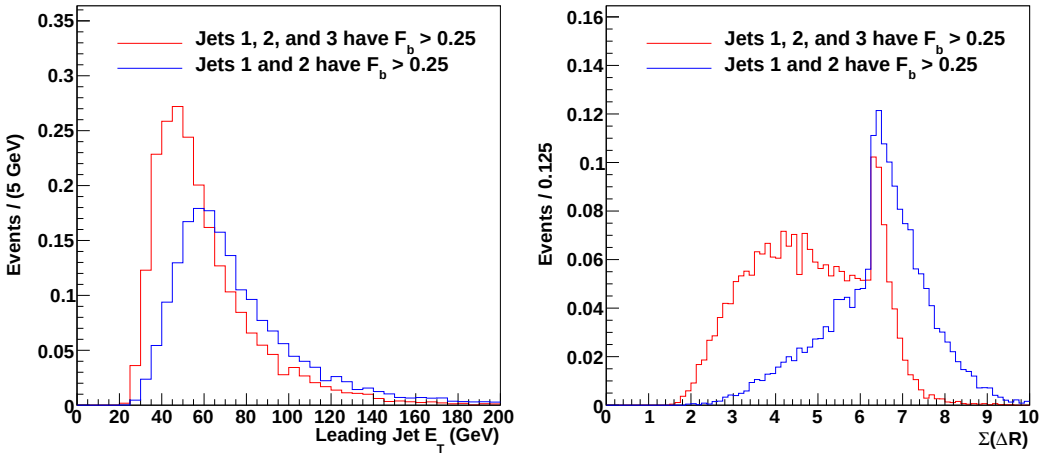

(a) Leading Jet E_T Distributions (b) $\sum \Delta R$ Distributions

Figure 6.13: The kinematic variables that we will use to separate events with three jets coming from the Higgs boson from events with only the leading two jets coming from the Higgs boson. Both distributions come from the WH ($m_H = 115$ GeV/c^2) sample and include events in the three-jet sample that contain at least two Higgs-like jets before any lepton selection or tagging requirement is applied.

Figure 6.16 show the input variables for our multijet mass for the tight leptons (TLEP) and PHX leptons before any tagging requirement. The backgrounds model the data well, so we can proceed to look at the multijet reconstructed mass distributions for all the tagging categories.

6.4.5 Three-Jet Discriminants

Figures 6.17 through 6.18 show the multijet mass distributions with the WH signal scaled up by a factor of 10. We will use these templates in Chap. 8 to calculate how much WH signal is present in our data.

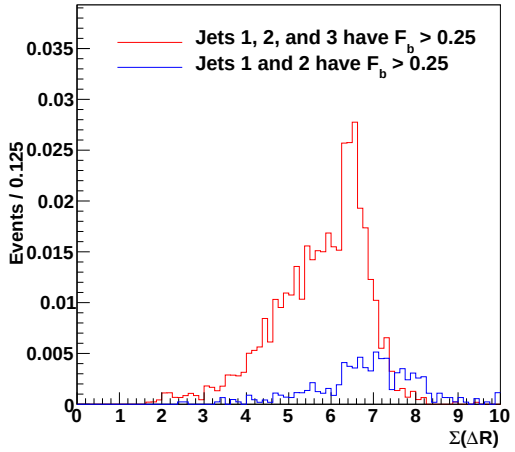

(a) $E_T(\text{jet } 1) < 40$ GeV

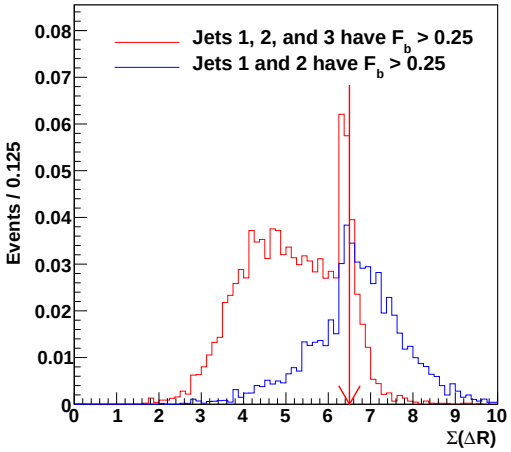

(b) $40 < E_T(\text{jet } 1) < 60$ GeV

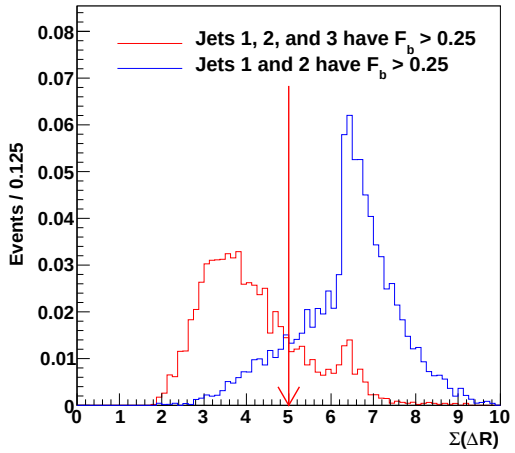

(c) $60 < E_T(\text{jet } 1) < 100$ GeV

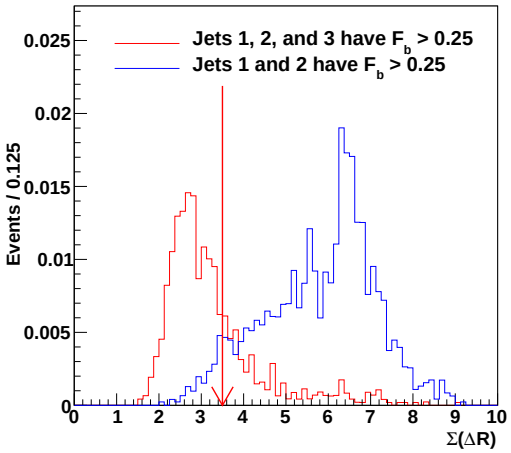

(d) $E_T(\text{jet } 1) > 100$ GeV

Figure 6.14: The $\sum \Delta R$ distributions for four leading jet E_T (E_T(jet 1)) ranges. The red arrows indicate the $\sum \Delta R$ requirements for our definition of the reconstructed multijet mass (m_H^{multijet}), if the value is lower than the red arrow, we use all three jets to reconstruct the Higgs boson, and if it is above, we only use the two leading jets. If $E_T(\text{jet } 1) < 40$ GeV, we always use all three jets for the reconstruction.

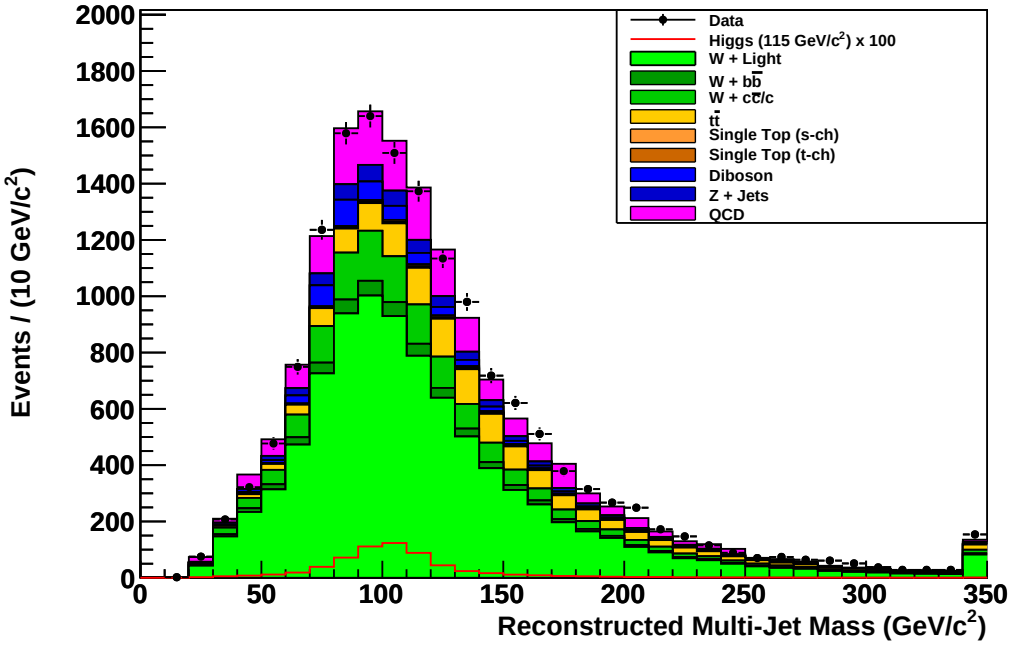

Figure 6.15: The reconstructed multijet mass (m_H^{multijet}) with all of the backgrounds for the tight leptons before any tagging requirement is applied. The WH (m_H = 115 GeV/c^2) signal is superimposed and scaled up by a factor of 100.

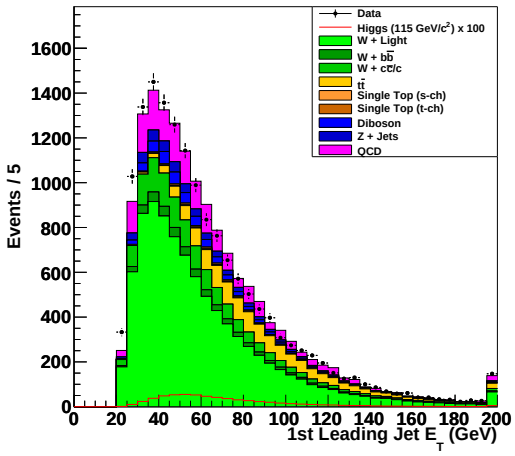

(a) Leading Jet E_T for TLEP

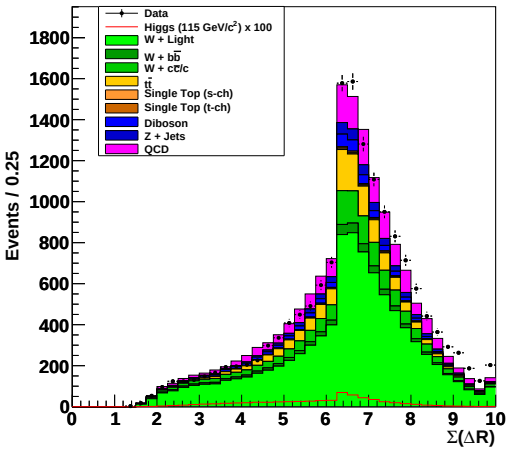

(b) $\sum \Delta R$ for TLEP

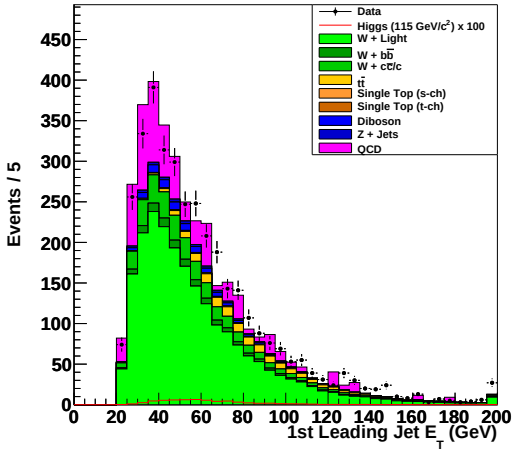

(c) Leading Jet E_T for PHX

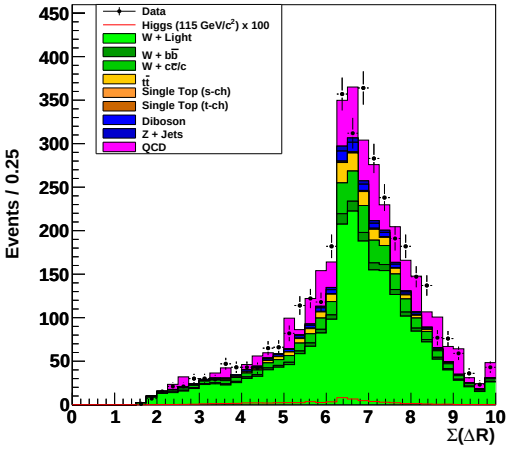

(d) $\sum \Delta R$ for PHX

Figure 6.16: The three-jet sample discrimination variables together with their background predictions before any tagging requirement is applied. The superimposed WH ($m_H = 115$ GeV/c^2) signal is scaled up by a factor of 100.

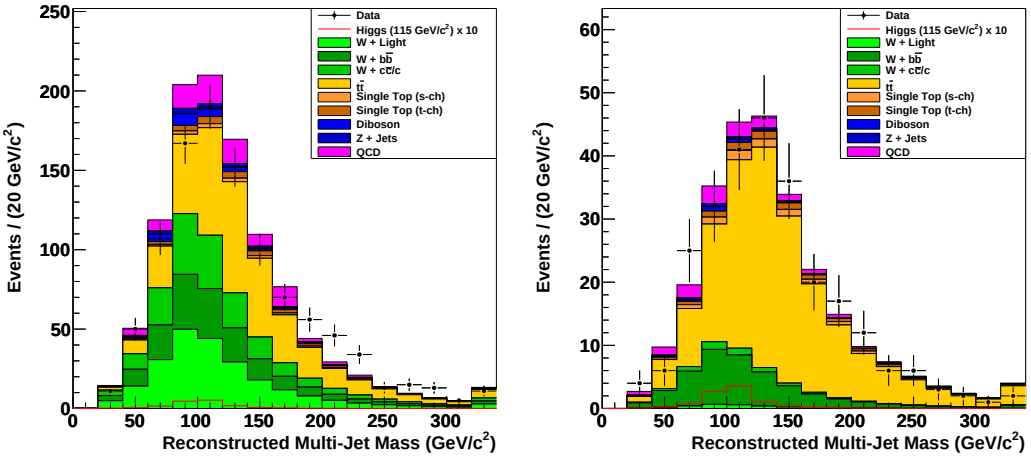

(a) 1S

(b) $\geq$2S

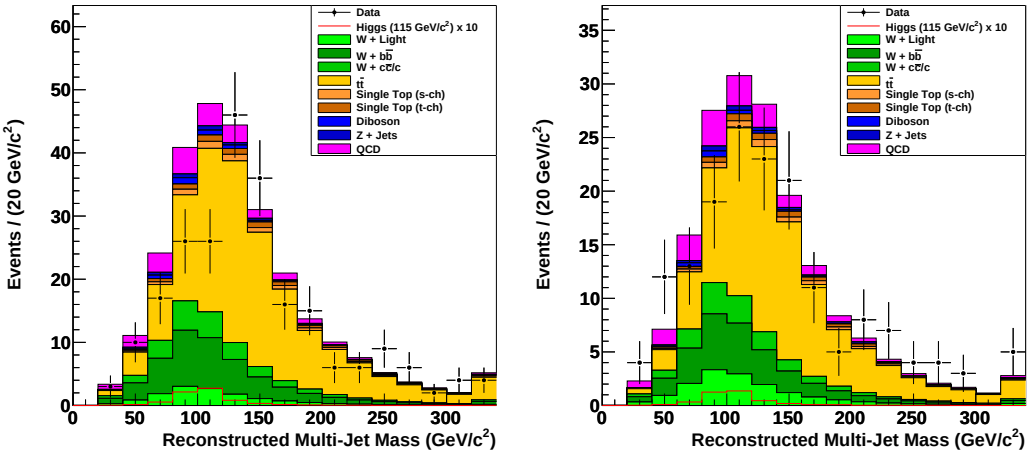

(c) S+J

(d) S+R

Figure 6.17: The multijet mass distributions (m_H^{multijet}) for all tagging categories for the tight leptons.

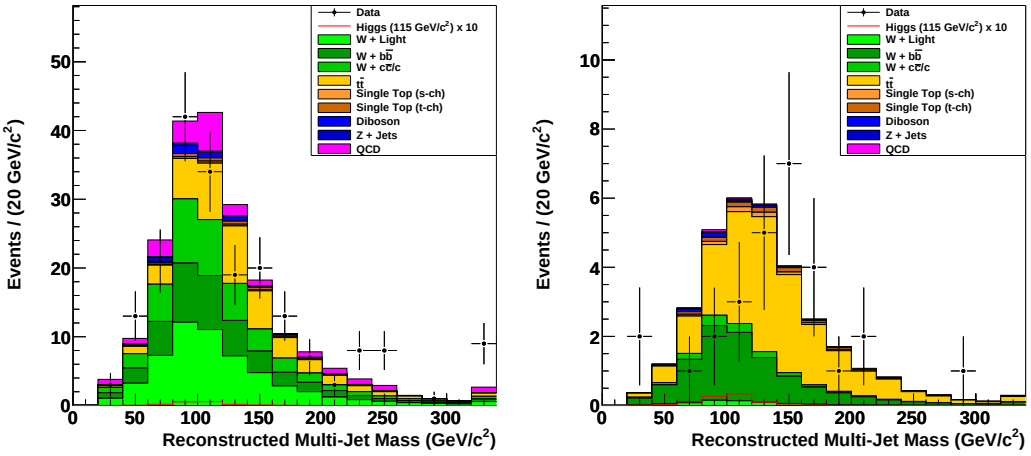

(a) 1S

(b) $\geq$2S

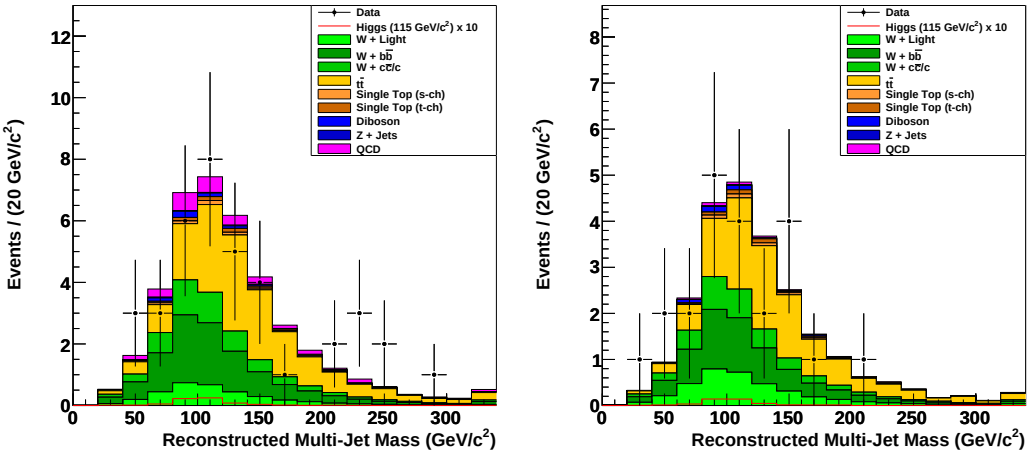

(c) S+J

(d) S+R

Figure 6.18: The multijet mass distributions (m_H^{multijet}) for all tagging categories for the PHX leptons.

CHAPTER SEVEN

Systematic Uncertainties

7.1 Introduction

Before determining how much Higgs signal we can extract from the data, we need to consider all of the uncertainties associated with our measurements. These include uncertainties on the backgrounds that we calculated in Chap. 5, uncertainties on the lepton and tagging identification from Chap. 4, uncertainties on measurements performed by our detector from Chap. 2, and uncertainties on the theoretical cross sections from Chap. 1. In this chapter, we explain how each uncertainty is calculated in detail and conclude by showing the uncertainties used for the limit calculation in Chap. 8.

The total uncertainties for the MC-based backgrounds and signal distributions come from the uncertainties of each of the terms in Eq. (5.1), which is reproduced here:

$$N_i = (\sigma \cdot BR)_i \cdot \int L\,dt \cdot \frac{N_i^{\text{sel}}}{N_i^{\text{tot}}} \cdot \epsilon_{z_0}^{\text{data}} \cdot \epsilon_{\text{trig}}^{\text{data}} \cdot SF_{\text{lep ID}} \cdot SF_{\text{tag}} \tag{7.1}$$

Let us first consider the uncertainties on each of the terms and then turn to the uncertainties associated with the other backgrounds.

7.2 Cross Section

We use the cross sections in Table 5.3 to normalize the MC-based backgrounds. We use the quoted uncertainty for the Z + jets template, which is equivalent to a relative uncertainty of 10.8%. For the other processes, we use the relative uncertainties set by the Tevatron New Phenomena & Higgs Working Group, which are 10% for all top processes ($t\bar{t}$, single top s-channel, single top t-channel), 6% for all

diboson processes (WW, WZ, and ZZ), and 5% for the WH cross sections from Table 6.1.

7.3 Branching Ratio

The branching ratio is purely related to the choice of MC sample and what processes are generated therein, so we do not associate an uncertainty with it.

7.4 Luminosity

We apply a 6% relative uncertainty due to mismeasurements of the luminosity with the CLC.

7.5 z_0 Vertex Efficiency

The relative uncertainty for the z_0 vertex efficiency is provided by the Joint Physics group and is approximately 0.2% (cf. Table 5.1).

7.6 Trigger Efficiency

The uncertainties for the trigger efficiency are also provided by the Joint Physics Group and are less than 1% for all of the lepton triggers (cf. Table 5.1).

7.7 Lepton Identification Efficiency

We use a 2% relative uncertainty for all lepton categories based on the study in [43].

7.8 b-Tagging Scale Factor

We calculate the scale factor uncertainties by propagating the uncertainties from Table 5.2 through the leading terms in Eqs. (5.2) – (5.5). This yields one

uncertainty for each tagging category:

$$\Delta_{\geq 2\mathrm{S}} = 2\,\frac{\Delta SF_{\mathrm{S}}}{SF_{\mathrm{S}}} \tag{7.2}$$

$$\Delta_{\mathrm{S+J}} = \sqrt{\left(\frac{\Delta SF_{\mathrm{S}}}{SF_{\mathrm{S}}}\right)^2 + \left(\frac{\Delta SF_{\mathrm{J}}}{SF_{\mathrm{J}}}\right)^2} \tag{7.3}$$

$$\Delta_{\mathrm{S+R}} = \sqrt{\left(\frac{\Delta SF_{\mathrm{S}}}{SF_{\mathrm{S}}}\right)^2 + \left(\frac{\Delta SF_{\mathrm{R}}}{SF_{\mathrm{R}}}\right)^2} \tag{7.4}$$

$$\Delta_{1\mathrm{S}} = \frac{\Delta SF_{\mathrm{S}}}{SF_{\mathrm{S}}} \tag{7.5}$$

7.9 Initial- and Final-State Radiation

Initial-state (final-state) radiation refers to the gluon radiation from the incoming (outgoing) quarks. We set a parameter that controls the amount of gluon radiation from the quarks when we generate MC samples. In order to study the effects of this MC parameter, we generate two WH ($m_H = 120$ GeV/c^2) MC samples. For one, we increase the amount of initial- and final-state radiation (`chgt70`), and for the other, we decrease the amount of initial- and final- state radiation (`chgt71`). The uncertainty is then calculated from the difference in the number of accepted events between the samples with more ISR/FSR (N_{more}) and less ISR/FSR (N_{less}). Here is the mathematical definition of the relative uncertainty:

$$\Delta_{\mathrm{ISR/FSR}} = \frac{|N_{\mathrm{more}} - N_{\mathrm{less}}|}{2N_{\mathrm{nominal}}} \tag{7.6}$$

where N_{nominal} is the number of accepted events in the standard WH ($m_H = 120\,\mathrm{GeV}/c^2$) MC sample (`chgt7e`).

7.10 Parton Distribution Function

When we generate MC samples, we use Parton Distribution Function (PDF) sets to describe the momentum distribution of the partons inside of a proton. The Coordinated Theoretical-Experimental Project on QCD (CTEQ) collaboration compiles these PDF sets from experimental data. At CDF, we use the CTEQ5L PDF

set to generate our MC samples. In order to study the uncertainty due to this PDF set, we use the Joint Physics Group's recommended PDF reweighting procedure. The idea is to calculate event weights for 22 different PDF sets and then calculate the relative uncertainty by comparing the weighted events to the nominal CTEQ5L events. The 22 PDF sets consist of 20 CTEQ6M sets (CTEQ6M1 – CTEQ6M20) and two PDF sets from the MRST collaboration (MRST72 and MRST75). The uncertainties calculated by this method are asymmetric, so we use the larger of the two for this analysis.

7.11 Jet Energy Scale

We also have to account for uncertainties due to the the jet energy corrections that we calculated in Sec. 3.3.1, known as jet energy scale (JES) uncertainties. We do this by shifting the corrected jet E_T up and down by one standard deviation and then calculating the uncertainty from the difference between accepted events and the nominal value. We use the WH ($m_H = 115$ GeV/c^2) sample for this study. The acceptances are N_{up} for the up-shifted sample, N_{down} for the down-shifted sample, and N_{nominal} for the standard sample. The relative uncertainty is the larger of the following two:

$$\begin{aligned} \Delta_{\text{up}} &= \frac{|N_{\text{nominal}} - N_{\text{up}}|}{N_{\text{nominal}}} \\ \Delta_{\text{down}} &= \frac{|N_{\text{nominal}} - N_{\text{down}}|}{N_{\text{nominal}}} \end{aligned} \tag{7.7}$$

7.12 QCD Estimation

The uncertainties due to the QCD estimation method in this section are based on unpublished studies performed within the WH group. We use a 40% relative uncertainty for samples that use the standard QCD estimation and a 100% uncertainty for the double-tagged samples that require the low-statistics QCD estimation method (cf. Sec. 5.5.1). In the TLEP samples, we use a 70% relative uncertainty

if at least one of the QCD estimates for CEM, CMUP, and CMX were performed with the low-statistics method; if all three were performed with the low-statistics method, we use 100%.

7.13 W + Heavy Flavored Jets

The largest uncertainty on the $W + b\bar{b}$ and $W + c/c\bar{c}$ samples comes from the K factors from Table 5.9.

7.14 W + Light Flavored Jets / Mistags

The mistag matrices discussed in Sec. 5.5.3.2 provide uncertainties for their tag rates. For each tagger, we individually shift the mistag rates up and down and then calculate the resulting shift in the number of negative tags (N_-) using the same method as in Eq. (7.7). The uncertainty for each tagger is the larger of the two shift uncertainties. We then combine the uncertainties for the three taggers as follows:

$$\Delta_{\text{mistag}} = \sqrt{\Delta_{\text{S}}^2 + \Delta_{\text{J}}^2 + \Delta_{\text{R}}^2} \tag{7.8}$$

7.15 Combined Uncertainties for the Limit Calculation

In this section, we show what uncertainties are combined for the background and signal samples. The uncertainties for each sample are added in quadrature for Tables 5.10–5.13. In Chap. 8, we explain how the uncertainties are combined for the limit calculation. We conclude this section with tables showing the numeric values of the individual uncertainties that are used for the limit calculation.

For the WH signal, diboson (WW, WZ, ZZ), top ($t\bar{t}$, single top s-channel, single top t-channel), and Z + jets samples, we combine the uncertainties of the following quantities:

- cross section
- luminosity

- z_0 vertex efficiency
- trigger efficiency
- lepton identification efficiency
- b-tagging scale factor
- initial- and final-state radiation
- parton distribution function
- jet energy scale

For the $W + b\bar{b}$ and $W + c/c\bar{c}$ samples, we combine the uncertainties of the following quantities:

- K factor
- initial- and final-state radiation
- parton distribution function
- jet energy scale

For the W + LF sample, we only use the uncertainty due to the mistag estimation method and for the QCD sample, we only use the uncertainty due to the QCD estimation method. Tables 7.1 and 7.2 show the relative uncertainties that change for each sample category for the two-jet and three-jet samples, respectively. Table 7.3 shows the relative uncertainties that are the same for all samples. The total uncertainty for a given background sample is calculated by summing the relevant uncertainties from the tables in quadrature.

Table 7.1: The relative uncertainty values given as percentages for each sample category in the two-jet sample.

Sample Category	Trigger	b-Tagging	ISR/FSR	PDF	JES	QCD	Mistags
TLEP 1S	0.8	5.2	1.5	0.8	1.3	40.0	20.6
TLEP $\geq$2S	0.8	10.4	3.9	0.9	0.6	40.0	41.8
TLEP S+J	0.8	8.3	1.8	0.8	0.4	40.0	35.2
TLEP S+R	0.8	9.5	2.4	0.8	1.0	40.0	20.1
PHX 1S	0.1	5.2	1.8	2.5	4.1	40.0	19.5
PHX $\geq$2S	0.1	10.4	4.7	2.4	1.4	100.0	39.7
PHX S+J	0.1	8.3	1.1	2.5	1.5	40.0	30.8
PHX S+R	0.1	9.5	3.0	2.4	1.1	100.0	19.1

Table 7.2: The relative uncertainty values given as percentages for each sample category in the three-jet sample.

Sample Category	Trigger	b-Tagging	ISR/FSR	PDF	JES	QCD	Mistags
TLEP 1S	0.8	5.2	5.1	0.7	13.5	40.0	17.5
TLEP $\geq$2S	0.8	10.4	3.0	0.8	9.7	40.0	36.9
TLEP S+J	0.8	8.3	4.0	0.9	10.5	70.0	28.2
TLEP S+R	0.8	10.0	6.1	0.8	11.8	70.0	17.4
PHX 1S	0.1	5.2	7.2	2.7	15.4	40.0	17.2
PHX $\geq$2S	0.1	10.4	7.8	2.7	12.1	100.0	36.4
PHX S+J	0.1	8.3	3.0	3.1	11.7	40.0	26.3
PHX S+R	0.1	10.0	1.5	2.2	11.7	100.0	17.2

Table 7.3: The relative uncertainty values that are the same for all sample categories.

Uncertainty Type	Value
Luminosity	6%
z_0 Vertex Efficiency	0.185%
Lepton Identification Efficiency	2%
WH Cross Sections	5%
Top Cross Sections	10%
Diboson Cross Sections	6%
Z + jets Cross Section	10.8%
K factor	28.6%

CHAPTER EIGHT

Limit Calculation

Now that we have the discriminant distributions from Chap. 6 and the systematic uncertainties from Chap. 7, we can calculate how much Higgs boson signal is in our data. We do this by calculating the upper limit on the Higgs boson production cross section allowed for by our data. In high-energy particle physics, limits are consistently reported with a 95% confidence level. In this chapter, we will first explain how to calculate a general limit using a Bayesian approach and then account for systematic uncertainties; we will then explain how to determine an expected limit range with the use of pseudodata, and we will conclude by presenting the limits for this analysis.

8.1 Statistical Inference

In experimental physics, we often want to infer the statistical properties of a distribution based on a measurement. In this analysis, the measurements are subdivided into discrete bins, so the data in each bin can be considered the result of a one-bin counting experiment. We can use a Poisson distribution to describe the outcomes of these one-bin experiments. To rephrase the initial question, we want to infer the expected number of events (μ) of the Poisson distribution from the number of collected events (n) in each bin. The Poisson probability of n events occurring for an expectation of μ is given by:

$$p(n|\mu) = \frac{\mu^n e^{-\mu}}{n!} \tag{8.1}$$

There are two approaches to making such an inference, the Frequentist and Bayesian approaches. The Frequentist approach assumes no prior knowledge of the probability distributions and relies on a test statistic to separate background and

signal. This approach is used by DØ. At CDF, we employ the Bayesian approach, which is based on Bayes' theorem:

$$p(\mu|n) = \frac{p(n|\mu)p(\mu)}{p(n)} \tag{8.2}$$

where $p(\mu)$ represents the assumed probability distribution of μ before the experiment, known as the prior probability. Similarly, $p(\mu|n)$ is known as the posterior probability distribution; this is the distribution that we want to calculate. The denominator of Eq. (8.2) is called the marginal probability and is defined as follows:

$$p(n) = \int p(n|\mu)p(\mu)d\mu \tag{8.3}$$

where the integral is taken over all values of μ.

Before we can rewrite Eq. (8.2) in terms of the number of background, signal, and data events, we have to define the prior probability distribution. Let us first define the following three quantities:

- D: The number of observed data events (cf. Tables 5.10–5.13).
- B: The total number of background events (cf. Tables 5.10–5.13).
- S: The number of signal events. This is the number that we are ultimately interested in.

The sum of background and signal corresponds to the expected number of events (i.e. $\mu = B + S$), and D corresponds to the number of observed events (n). We do not want to favor any one expected number of signal events over another, and we do not want to allow a negative number of expected signal events, so we assume the following prior probability distribution:

$$p(\mu) = \begin{cases} 0 & \text{when } \mu < B \\ k & \text{when } \mu \geq B \end{cases} \tag{8.4}$$

where k is a constant. We can now rewrite Eq. (8.2) as follows:

$$p(\mu|n) = \begin{cases} 0 & \text{when } \mu < B \\ c_n p(n|\mu) & \text{when } \mu \geq B \end{cases} \tag{8.5}$$

where $p(n|\mu)$ is given by Eq. (8.1), and $c_n = \frac{k}{p(n)}$ is a constant for a given value of n and can be determined with the normalization condition:

$$\int p(\mu|n)d\mu = 1 \tag{8.6}$$

Since we are interested in placing an upper limit on the number of signal events, let us rewrite S as a function of the number of calculated WH signal events s predicted by the standard model (cf. Tables 5.10–5.13) multiplied by a scaling factor f:

$$S(f) = f \cdot s \tag{8.7}$$

We want to calculate the 95% confidence level limit (x_{95}) on f so that we can report the limit on the multiplicative factor of the standard model prediction. The significance of using f rather than S is that if the observed limit for f falls below one, we can exclude the existence of a standard model Higgs boson with a 95% confidence level. We can now form the limit integral in terms of B, D, s, and f:

$$\begin{aligned} 0.95 &= \int_0^{x_{95}} p(B + f \cdot s|D)df \\ &= \int_0^{x_{95}} c_D p(D|B + f \cdot s)df \\ &= \int_0^{x_{95}} c_D \frac{(B + f \cdot s)^D e^{-(B+f\cdot s)}}{D!} df \end{aligned} \tag{8.8}$$

8.2 Uncertainties

The discussions in the previous section did not take uncertainties associated with the measurement and the background predictions into account. We assume that our systematic uncertainties follow a Gaussian distribution. This means that,

given a nominal value $\hat{r}$ and an uncertainty σ_r, we expect the probability distribution to be Gaussian, which is defined as follows:

$$p^g(r;\hat{r},\sigma_r) =\sim \frac{1}{\sqrt{2\pi\sigma_r^2}} e^{-\frac{(r-\hat{r})^2}{2\sigma_r^2}} \tag{8.9}$$

In order to incorporate a Gaussian uncertainty (σ) into our limit calculation, we introduce a nuisance parameter (k) with Gaussian probability distribution $p^g(k;1,\sigma)$. For example, B is the sum of several backgrounds $B = \sum b_i$, and each one of these backgrounds has an uncertainty σ_i. We can therefore rewrite the expected number of events as a function of the k_i as follows:

$$\mu(f,k_i) = B(k_i) + f \cdot s = \sum_i (k_i \cdot b_i) + f \cdot s \tag{8.10}$$

Of course, we also have uncertainties that apply to multiple backgrounds collectively, as for example the lepton identification uncertainty, and we have uncertainties that are only applied to the signal, so we have to introduce nuisance parameters for all of these uncertainties. Taking all of these uncertainties into account, the combined expectation becomes:

$$\mu(f,k_{ij}) = \sum_{i\geq 1} \left(\left(\prod_{j\in\Delta_i} k_{ij} \right) \cdot b_i \right) + \left(\prod_{j\in\Delta_0} k_{0j} \right) \cdot f \cdot s \tag{8.11}$$

where Δ_0 and Δ_j are the sets of indices of the nuisance parameters that apply to the signal and background, respectively. We then form the probability distribution by convolving the probability with a Gaussian distribution for each nuisance parameter as follows:

$$P(D|\mu(f,k_{ij})) = p(D|\mu(f,k_{ij})) \prod_j p_j^g(k_{ij};1,\sigma_j) \tag{8.12}$$

where $p(D|\mu(f,k_{ij}))$ is formed by substituting Eq. (8.11) into Eq. (8.5). In order to form the confidence level integral from Eq. (8.8), we also have to integrate over all k_j. This is known as integrating out the nuisance parameters and mathematically

it looks like this:

$$0.95 = \int_0^{x_{95}} \left[\int P(D|\mu(f, k_{ij}))dk_1...dk_j \right] df \tag{8.13}$$

Note that P has to be normalized.

All of the previous discussion was based on a one-bin counting experiment, so in order to form the limit integral over several bins, we convolve the probabilities of all bins. If the probability of one bin is given by P_m, then Eq. (8.13) can be rewritten as follows:

$$0.95 = \int_0^{x_{95}} \left[\int \prod_m \{P_m(D|\mu(f, k_{ij}))\} \, dk_1...dk_j \right] df \tag{8.14}$$

In this equation, the number of nuisance parameters (k_j) has increased to include uncertainties for individual bins as well as uncertainties that span several bins. Finally, we can form the limit integral over several channels by concatenating the discriminant histograms from Secs. 6.3.1 and 6.4.5 into one long histogram with several bins.

8.3 Pseudodata and Expected Limit

As discussed in previous sections, we rely heavily on simulation techniques to interpret the detector data and to calculate our background and signal distributions. For this reason, it is not possible to calculate analytically what our final sensitivity to WH production is, so we generate so-called pseudodata based on our backgrounds in the absence of signal. Pseudodata is generated by fluctuating the background estimates within their uncertainties, which yields a distribution that resembles our expected data distribution. With this pseudodata, we calculate the 95% confidence level upper limit as described in the previous sections. If our detector and analysis techniques were ideal, this should yield a limit close to zero since the pseudodata were produced in the absence of signal. The process of performing the analysis with pseudodata is known as a pseudoexperiment. In order to obtain a sta-

tistically meaningful range of expected limits, we generate 1000 pseudoexperiments that yield a distribution of 1000 limits. The median of this distribution is considered the expected limit. In Sec. 8.4, we will report the distribution of the 1000 pseudo-experiments with the following five quantities: the median, the lower and upper one standard deviation bounds ($\pm 1\sigma$), and the lower and upper two standard deviation bounds ($\pm 2\sigma$).

8.4 Results

In this section we present the 95% confidence level upper limits on the *WH* production cross section calculated for this analysis. First, we will present the limits for the three-jet sample using our multijet reconstruction technique and compare them to the three-jet sample limits that would result from using only the dijet mass. We will then present the two-jet sample limits and the final limits resulting from the combination of the two- and three-jet samples.

We use the following channels for the three-jet sample limit calculation:

- TLEP $\geq$2S
- TLEP S+R
- PHX 1S
- PHX $\geq$2S
- PHX S+J
- PHX S+R

The TLEP 1S and TLEP S+J were excluded from the limit calculation because their individual limits fall far below the expected range. This is due to the fact that the background model cannot incorporate the large downward fluctuation of the data in the signal region of the TLEP S+J channel and because of its underestimation in the high mass tail of the TLEP 1S channel.

We use the following channels for the two-jet sample limit calculation:

- TLEP ≥2S
- TLEP S+J
- TLEP S+R
- PHX ≥2S
- PHX S+J
- PHX S+R

As explained in Sec. 6.3, the BNN discrimination templates in the two-jet sample are based on a previous WH search [41]. Since that analysis was performed, the accepted method of calculating the W + LF background has changed. This does not play a large role in the double-tagged categories because the W + LF contribution is small; however, in the 1S category this causes our W + LF estimates to be different from the ones in [41]. For this reason, we exclude the 1S channels from the limit calculation.

As discussed in Sec. 8.3, the expected limit is a measure of the sensitivity of our search. In Table 8.1, we compare the limit calculated in the three-jet sample using the dijet reconstruction technique with the limit calculated using the multijet reconstruction technique. We see that the new multijet technique improves our search sensitivity by up to 3.9% for some Higgs boson masses. More important than an improvement in the sensitivity is that we are able to better model the WH signal distribution using the multijet reconstruction technique (see Fig. 6.12). In the future, we plan to better exploit this modeling to separate the signal and background events in the three-jet sample.

Figure 8.1 shows the expected and observed limits for the two-jet sample using the BNN discriminants and for the three-jet sample using the multijet reconstructed mass. Figure 8.2 shows the combined limit for the two- and three-jet samples, and Table 8.2 gives the numerical values. Based on the observed limits, we set upper

Table 8.1: The median expected 95% confidence level upper limits on WH production normalized to the standard model prediction. The limits are based on the three-jet sample using the dijet and multijet reconstructed masses. The improvement is relative to the dijet limit and is only displayed for masses for which the new multijet technique improved the limit.

Higgs Boson Mass (GeV/c^2)	Dijet Limit	Multijet Limit	Improvement
100	24.6	23.7	3.7%
105	27.2	26.6	2.2%
110	31.1	31.9	-
115	36.9	37.4	-
120	43.7	43.5	0.5%
125	56.7	54.5	3.9%
130	71.0	73.4	-
135	97.3	96.1	1.2%
140	149	144	3.4%
145	194	193	0.5%
150	270	280	-

limits on the WH production rate between 3.36 and 28.7 times the standard model prediction in the Higgs boson mass range from 100 to 150 GeV/c^2.

In Table 8.3 we compare the median expected limit for the two-jet sample with that of the combined two- and three-jet sample. We see that the addition of the three-jet sample with the multijet reconstruction technique improved our overall search sensitivity between 1.1 and 11.5% in the entire Higgs boson mass range from 100 to 150 GeV/c^2.

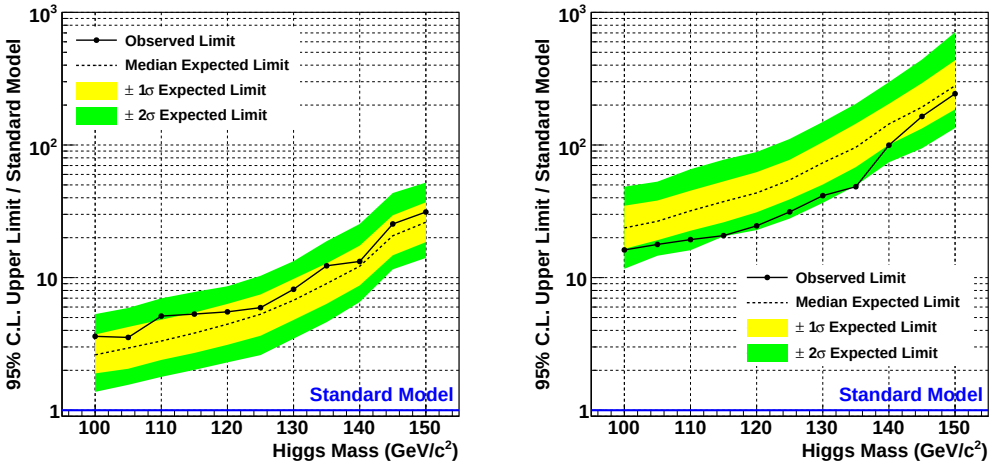

(a) Two-Jet Sample (b) Three-Jet Sample

Figure 8.1: The 95% confidence level upper limits on the WH production cross section as a function the Higgs boson mass. The limits are normalized to the standard model prediction, which is indicated by the blue line.

Table 8.2: The observed and median expected 95% confidence level upper limits on WH production normalized to the standard model prediction. The limits are shown for the combined two- and three-jet samples.

Higgs Boson Mass (GeV/c^2)	Observed Limit	Median Expected Limit
100	3.45	2.59
105	3.36	2.84
110	4.68	3.23
115	4.75	3.54
120	4.94	4.14
125	5.17	4.83
130	6.91	6.36
135	10.2	8.24
140	12.1	10.8
145	23.3	19.6
150	28.7	24.1

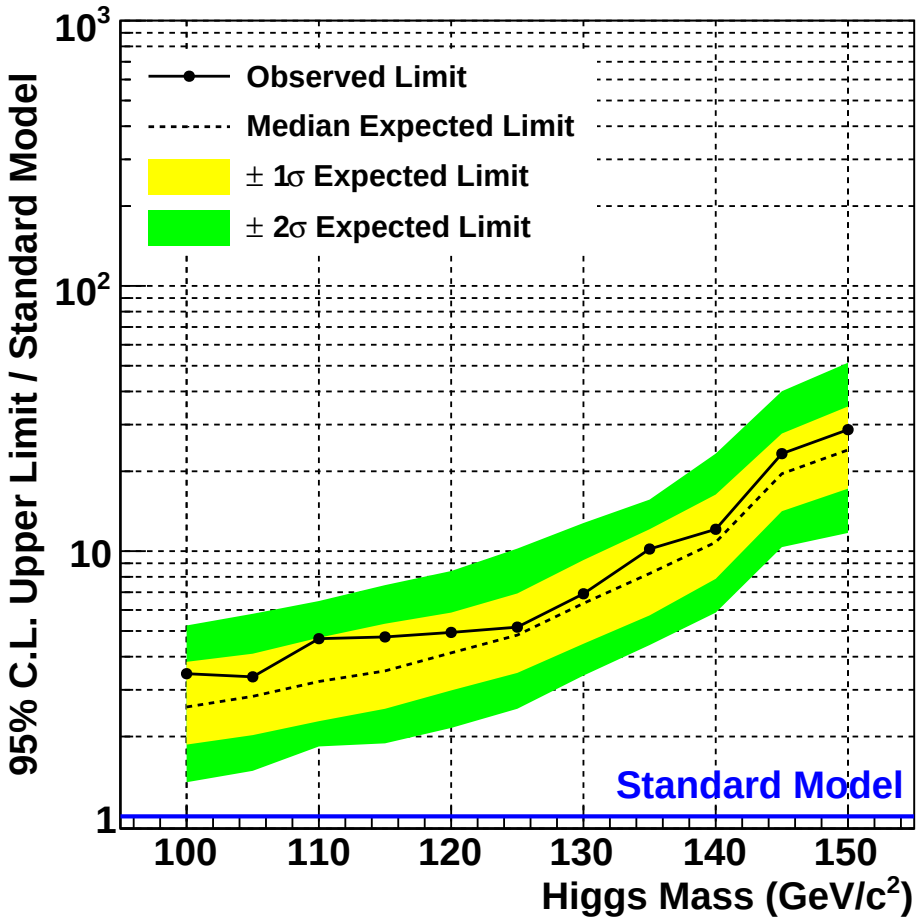

Figure 8.2: The combined two- and three-jet sample 95% confidence level upper limits on the WH production cross section as a function the Higgs boson mass. The limits are normalized to the standard model prediction, which is indicated by the blue line. The numerical values of the observed and median expected limit are shown in Table 8.2.

Table 8.3: The median expected 95% confidence level upper limits on WH production normalized to the standard model prediction. The limits are shown for the two-jet sample and the combined two- and three-jet sample. The improvement is relative to the two-jet sample limit.

Higgs Boson Mass (GeV/c^2)	Two-Jet Sample	Two- and Three-Jet Sample	Improvement
100	2.62	2.59	1.1%
105	2.95	2.84	3.7%
110	3.33	3.23	3.0%
115	3.82	3.54	7.3%
120	4.46	4.14	7.2%
125	5.30	4.83	8.9%
130	6.75	6.36	5.8%
135	9.02	8.24	8.6%
140	12.2	10.8	11.5%
145	20.7	19.6	5.3%
150	26.2	24.1	8.0%

CHAPTER NINE

Conclusion

We performed a direct search for standard model Higgs boson production in $p\bar{p}$ collisions at a center of mass energy of $\sqrt{s} = 1.96$ TeV. The search was performed using the CDF II detector and a data set corresponding to an integrated luminosity of 6.3 fb^{-1}. We searched for Higgs boson production in association with a W boson with the Higgs boson decaying into a bottom/antibottom quark pair. We introduced a novel technique to reconstruct a Higgs boson in the three-jet sample using a multijet reconstruction technique and found that this technique improves the signal modeling over the standard dijet reconstruction technique. Furthermore, by combining the BNN discriminants in the two-jet sample with the multijet mass in the three-jet sample, we found an overall improvement of our search sensitivity of 1.1 to 11.5% for Higgs boson masses between 100 and 150 GeV/c^2.

Our data shows no evidence of a Higgs boson since the observed limits are within the expected limit range, so we set 95% confidence level upper limits on the WH production rate. The limit for a Higgs boson mass of 115 GeV/c^2 is

$$\sigma(p\bar{p} \to W^{\pm}H) \times \mathrm{BR}(H \to b\bar{b}) < 4.75 \times \mathrm{SM}$$

where SM stands for the standard model prediction. We set limits between 3.36 and 28.7 times the standard model prediction for the Higgs boson mass range from 100 to 150 GeV/c^2.

APPENDICES

APPENDIX A

Trigger Tables

In this appendix we will show the detailed trigger tables for the triggers that we currently use. Trigger table versions change over time, so we will only show the most current tables here. As described in Sec. 2.4, we use a three level triggering system, so each trigger table below will show the level one, two, and three requirements. Here are the main triggers for the four lepton categories (CEM, PHX, CMUP, and CMX):

- CEM Electrons (`ELECTRON_CENTRAL_18`)
  - Level 1:

```
ELECTRON ET_CENTRAL = 8 GeV
ELECTRON HAD_EM_CENTRAL = .125
ELECTRON NUMBER = 1
ELECTRON XFT_CHARGE = 0
ELECTRON XFT_LAYERS = 4
ELECTRON XFT_PT = 8.34 GeV/c
```

  - Level 2:

```
ElectronCluster ABS_ETA_MAX = 1.317
ElectronCluster ABS_ETA_MIN = 0
ElectronCluster CLUSTER_PASS = 14
ElectronCluster ET = 18 GeV
ElectronCluster HAD_EM = .125
ElectronCluster NUMBER = 1
ElectronCluster XFT_LAYERS = 4
```

```
ElectronCluster XFT_PT = 8 GeV/c
ElectronCluster XFT_STEREO_CONFIRM = 0
```

– Level 3:

```
CalorRegion = 0
LShr = 0.4
ZVert = 2
cenDeltaZ = 8
cenEt = 18.0
cenHadEm = 0.125
cenTrackPt = 9.0
nEmObj = 1
nTowersHadEm = 3
```

- PHX Electrons (MET_PEM)

  – Level 1:

```
PHOTON ET_CENTRAL = 8 GeV
PHOTON ET_PLUG = 8 GeV
PHOTON HAD_EM_CENTRAL = .125
PHOTON HAD_EM_PLUG = .0625
PHOTON NUMBER = 1
MET_PULSAR ET = 15 GeV
```

  – Level 2:

```
GlobalMisEt ET = 15 GeV
GlobalMisEt MET_TYPE = 2
PhotonCluster ABS_ETA_MAX = 3.6
PhotonCluster ABS_ETA_MIN = 1.1
```

```
PhotonCluster CLUSTER_PASS = 14
PhotonCluster ET = 20 GeV
PhotonCluster ET_TOTAL = 0 GeV
PhotonCluster HAD_EM = .125
PhotonCluster ISO_ET = 999 GeV
PhotonCluster ISO_FRACTION = 999
PhotonCluster NUMBER = 1
```

  - Level 3:

```
CalorRegion = 1
ZVert = 2
nEmObj = 1
plugEt = 20
plugHadEm = 0.125
plugHadEmCeiling = 9999
MetCut = 15.0
```

- CMUP Muons (`MUON_CMUP18`)

  - Level 1:

```
MUON_CMU(P) CMU_STUB_PT = 6 GeV/c
MUON_CMU(P) CMU_XFT_PT = 4.09 GeV/c
MUON_CMU(P) REQUIRE_CMP = 1
MUON_CMU(P) REQUIRE_CSP = 0
MUON_CMU(P) REQUIRE_HTDC_CMU = 0
```

  - Level 2:

```
Muon CALOR_TYPE = 0
Muon MUON_TYPE = 3
```

```
Muon NUMBER = 1
Muon USE_CSP = 0
Muon XFT_LAYERS = 4
Muon XFT_PT = 14.77 GeV/c
Muon XFT_STEREO_CONFIRM = 3
```

  - Level 3:

```
cmpDx = 20
cmuDx = 10
minPt = 18.0
nMuon = 1
selectCMUP  = true
```

- CMX Muons (`MUON_CMX18`)
  - Level 1:

```
MUON_CMX CMX_STUB_PT = 6 GeV/c
MUON_CMX CMX_XFT_LAYERS = 4
MUON_CMX CMX_XFT_PT = 8.34 GeV/c
MUON_CMX REQUIRE_CSX = 1
MUON_CMX REQUIRE_HTDC_CMX = 0
```

  - Level 2:

```
Muon CALOR_TYPE = 0
Muon MUON_TYPE = 4
Muon NUMBER = 1
Muon REQUIRE_HTDC = 1
Muon USE_CSP = 0
Muon XFT_LAYERS = 4
```

```
Muon XFT_PT = 14.77 GeV/c

Muon XFT_STEREO_CONFIRM = 3
```

– Level 3:

```
cmxDx = 10

minPt = 18.0

nMuon = 1

selectCMX = true
```

APPENDIX B

The CDF Collaboration

T. Aaltonen,[21] B. Álvarez González[w],[9] S. Amerio,[41] D. Amidei,[32] A. Anastassov,[36] A. Annovi,[17] J. Antos,[12] G. Apollinari,[15] J.A. Appel,[15] A. Apresyan,[46] T. Arisawa,[56] A. Artikov,[13] J. Asaadi,[51] W. Ashmanskas,[15] B. Auerbach,[59] A. Aurisano,[51] F. Azfar,[40] W. Badgett,[15] A. Barbaro-Galtieri,[26] V.E. Barnes,[46] B.A. Barnett,[23] P. Barria[dd],[44] P. Bartos,[12] M. Bauce[bb],[41] G. Bauer,[30] F. Bedeschi,[60] D. Beecher,[28] S. Behari,[23] G. Bellettini[bb],[60] J. Bellinger,[58] D. Benjamin,[14] A. Beretvas,[15] A. Bhatti,[48] M. Binkley*,[15] D. Bisello[bb],[41] I. Bizjak[hh],[28] K.R. Bland,[5] B. Blumenfeld,[23] A. Bocci,[14] A. Bodek,[47] D. Bortoletto,[46] J. Boudreau,[45] A. Boveia,[11] B. Brau[a],[15] L. Brigliadori[aa],[6] A. Brisuda,[12] C. Bromberg,[33] E. Brucken,[21] M. Bucciantonio[cc],[44] J. Budagov,[13] H.S. Budd,[47] S. Budd,[22] K. Burkett,[15] G. Busetto[bb],[41] P. Bussey,[19] A. Buzatu,[31] C. Calancha,[29] S. Camarda,[4] M. Campanelli,[33] M. Campbell,[32] F. Canelli[12],[15] A. Canepa,[43] B. Carls,[22] D. Carlsmith,[58] R. Carosi,[44] S. Carrillo[k],[16] S. Carron,[15] B. Casal,[9] M. Casarsa,[15] A. Castro[aa],[6] P. Catastini,[15] D. Cauz,[52] V. Cavaliere[cc],[44] M. Cavalli-Sforza,[4] A. Cerri[f],[26] L. Cerrito[q],[28] Y.C. Chen,[1] M. Chertok,[7] G. Chiarelli,[44] G. Chlachidze,[15] F. Chlebana,[15] K. Cho,[25] D. Chokheli,[13] J.P. Chou,[20] W.H. Chung,[58] Y.S. Chung,[47] C.I. Ciobanu,[42] M.A. Ciocci[dd],[44] A. Clark,[18] G. Compostella[bb],[41] M.E. Convery,[15] J. Conway,[7] M.Corbo,[42] M. Cordelli,[17] C.A. Cox,[7] D.J. Cox,[7] F. Crescioli[cc],[44] C. Cuenca Almenar,[59] J. Cuevas[w],[9] R. Culbertson,[15] D. Dagenhart,[15] N. d'Ascenzo[u],[42] M. Datta,[15] P. de Barbaro,[47] S. De Cecco,[49] G. De Lorenzo,[4] M. Dell'Orso[cc],[44] C. Deluca,[4] L. Demortier,[48] J. Deng[c],[14] M. Deninno,[6] F. Devoto,[21] M. d'Errico[bb],[41] A. Di Canto[cc],[44] B. Di Ruzza,[44] J.R. Dittmann,[5] M. D'Onofrio,[27] S. Donati[cc],[44] P. Dong,[15] M. Dorigo,[52] T. Dorigo,[41] K. Ebina,[56] A. Elagin,[51] A. Eppig,[32] R. Erbacher,[7] D. Errede,[22] S. Errede,[22] N. Ershaidat[z],[42] R. Eusebi,[51] H.C. Fang,[26] S. Farrington,[40] M. Feindt,[24] J.P. Fernandez,[29] C. Ferrazza[ee],[44] R. Field,[16] G. Flanagan[s],[46] R. Forrest,[7] M.J. Frank,[5] M. Franklin,[20] J.C. Freeman,[15] Y. Funakoshi,[56] I. Furic,[16] M. Gallinaro,[48] J. Galyardt,[10] J.E. Garcia,[18] A.F. Garfinkel,[46] P. Garosi[dd],[44] H. Gerberich,[22] E. Gerchtein,[15] S. Giagu[ff],[49] V. Giakoumopoulou,[3] P. Giannetti,[44] K. Gibson,[45] C.M. Ginsburg,[15] N. Giokaris,[3] P. Giromini,[17] M. Giunta,[44] G. Giurgiu,[23] V. Glagolev,[13] D. Glenzinski,[15] M. Gold,[35] D. Goldin,[51] N. Goldschmidt,[16] A. Golossanov,[15] G. Gomez,[9] G. Gomez-Ceballos,[30] M. Goncharov,[30] O. González,[29] I. Gorelov,[35] A.T. Goshaw,[14] K. Goulianos,[48] S. Grinstein,[4] C. Grosso-Pilcher,[11] R.C. Group,[55] J. Guimaraes da Costa,[20] Z. Gunay-Unalan,[33] C. Haber,[26] S.R. Hahn,[15] E. Halkiadakis,[50] A. Hamaguchi,[39] J.Y. Han,[47] F. Happacher,[17] K. Hara,[53] D. Hare,[50] M. Hare,[54] R.F. Harr,[57] K. Hatakeyama,[5] C. Hays,[40] M. Heck,[24] J. Heinrich,[43] M. Herndon,[58] S. Hewamanage,[5] D. Hidas,[50] A. Hocker,[15] W. Hopkins[g],[15] D. Horn,[24] S. Hou,[1] R.E. Hughes,[37] M. Hurwitz,[11] U. Husemann,[59] N. Hussain,[31] M. Hussein,[33] J. Huston,[33] G. Introzzi,[44] M. Iori[ff],[49] A. Ivanov[o],[7] E. James,[15] D. Jang,[10] B. Jayatilaka,[14] E.J. Jeon,[25] M.K. Jha,[6] S. Jindariani,[15] W. Johnson,[7] M. Jones,[46] K.K. Joo,[25] S.Y. Jun,[10] T.R. Junk,[15] T. Kamon,[51] P.E. Karchin,[57] Y. Kato[n],[39] W. Ketchum,[11] J. Keung,[43] V. Khotilovich,[51] B. Kilminster,[15] D.H. Kim,[25] H.S. Kim,[25] H.W. Kim,[25] J.E. Kim,[25] M.J. Kim,[17] S.B. Kim,[25] S.H. Kim,[53] Y.K. Kim,[11] N. Kimura,[56] M. Kirby,[15] S. Klimenko,[16] K. Kondo,[56] D.J. Kong,[25] J. Konigsberg,[16] A.V. Kotwal,[14] M. Kreps,[24] J. Kroll,[43] D. Krop,[11] N. Krumnack[l],[5] M. Kruse,[14] V. Krutelyov[d],[51] T. Kuhr,[24] M. Kurata,[53] S. Kwang,[11] A.T. Laasanen,[46] S. Lami,[44] S. Lammel,[15] M. Lancaster,[28] R.L. Lander,[7] K. Lannon[v],[37] A. Lath,[50] G. Latino[cc],[44] T. LeCompte,[2] E. Lee,[51] H.S. Lee,[11] J.S. Lee,[25] S.W. Lee[x],[51] S. Leo[cc],[44] S. Leone,[44] J.D. Lewis,[15] A. Limosani[r],[14] C.-J. Lin,[26] J. Linacre,[40] M. Lindgren,[15] E. Lipeles,[43] A. Lister,[18] D.O. Litvintsev,[15] C. Liu,[45] Q. Liu,[46] T. Liu,[15] S. Lockwitz,[59] N.S. Lockyer,[43] A. Loginov,[59] D. Lucchesi[bb],[41] J. Lueck,[24] P. Lujan,[26] P. Lukens,[15] G. Lungu,[48] J. Lys,[26] R. Lysak,[12] R. Madrak,[15] K. Maeshima,[15] K. Makhoul,[30] P. Maksimovic,[23] S. Malik,[48] G. Manca[b],[27] A. Manousakis-Katsikakis,[3] F. Margaroli,[46] C. Marino,[24] M. Martínez,[4] R. Martínez-Ballarín,[29] P. Mastrandrea,[49] M. Mathis,[23] M.E. Mattson,[57] P. Mazzanti,[6] K.S. McFarland,[47] P. McIntyre,[51] R. McNulty[i],[27] A. Mehta,[27] P. Mehtala,[21] A. Menzione,[44] C. Mesropian,[48] T. Miao,[15] D. Mietlicki,[32] A. Mitra,[1] H. Miyake,[53] S. Moed,[20] N. Moggi,[6] M.N. Mondragon[k],[15] C.S. Moon,[25] R. Moore,[15] M.J. Morello,[15] J. Morlock,[24] P. Movilla Fernandez,[15] A. Mukherjee,[15] Th. Muller,[24] P. Murat,[15] M. Mussini[aa],[6] J. Nachtman[m],[15] Y. Nagai,[53] J. Naganoma,[56] I. Nakano,[38] A. Napier,[54] J. Nett,[51] C. Neu,[55] M.S. Neubauer,[22] J. Nielsen[e],[26] L. Nodulman,[2] O. Norniella,[22] E. Nurse,[28] L. Oakes,[40] S.H. Oh,[14] Y.D. Oh,[25] I. Oksuzian,[55] T. Okusawa,[39] R. Orava,[21] L. Ortolan,[4] S. Pagan Griso[bb],[41] C. Pagliarone,[52] E. Palencia[f],[9] V. Papadimitriou,[15] A.A. Paramonov,[2] J. Patrick,[15] G. Pauletta[gg],[52] M. Paulini,[10] C. Paus,[30] D.E. Pellett,[7] A. Penzo,[52] T.J. Phillips,[14] G. Piacentino,[44] E. Pianori,[43] J. Pilot,[37] K. Pitts,[22] C. Plager,[8] L. Pondrom,[58] K. Potamianos,[46] O. Poukhov*,[13] F. Prokoshin[y],[13] A. Pronko,[15] F. Ptohos[h],[17] E. Pueschel,[10] G. Punzi[cc],[44] J. Pursley,[58] A. Rahaman,[45] V. Ramakrishnan,[58] N. Ranjan,[46] I. Redondo,[29] P. Renton,[40] M. Rescigno,[49] F. Rimondi[aa],[6] L. Ristori[45],[15] A. Robson,[19] T. Rodrigo,[9] T. Rodriguez,[43] E. Rogers,[22] S. Rolli,[54] R. Roser,[15] M. Rossi,[52] F. Rubbo,[15] F. Ruffini[dd],[44] A. Ruiz,[9] J. Russ,[10] V. Rusu,[15] A. Safonov,[51] W.K. Sakumoto,[47] Y. Sakurai,[56] L. Santi[gg],[52] L. Sartori,[44]

K. Sato,[53] V. Saveliev[u],[42] A. Savoy-Navarro,[42] P. Schlabach,[15] A. Schmidt,[24] E.E. Schmidt,[15] M.P. Schmidt[*],[59] M. Schmitt,[36] T. Schwarz,[7] L. Scodellaro,[9] A. Scribano[dd],[44] F. Scuri,[44] A. Sedov,[46] S. Seidel,[35] Y. Seiya,[39] A. Semenov,[13] F. Sforza[cc],[44] A. Sfyrla,[22] S.Z. Shalhout,[7] T. Shears,[27] P.F. Shepard,[45] M. Shimojima[t],[53] S. Shiraishi,[11] M. Shochet,[11] I. Shreyber,[34] A. Simonenko,[13] P. Sinervo,[31] A. Sissakian[*],[13] K. Sliwa,[54] J.R. Smith,[7] F.D. Snider,[15] A. Soha,[15] S. Somalwar,[50] V. Sorin,[4] P. Squillacioti,[15] M. Stancari,[15] M. Stanitzki,[59] R. St. Denis,[19] B. Stelzer,[31] O. Stelzer-Chilton,[31] D. Stentz,[36] J. Strologas,[35] G.L. Strycker,[32] Y. Sudo,[53] A. Sukhanov,[16] I. Suslov,[13] K. Takemasa,[53] Y. Takeuchi,[53] J. Tang,[11] M. Tecchio,[32] P.K. Teng,[1] J. Thom[g],[15] J. Thome,[10] G.A. Thompson,[22] E. Thomson,[43] P. Ttito-Guzmán,[29] S. Tkaczyk,[15] D. Toback,[51] S. Tokar,[12] K. Tollefson,[33] T. Tomura,[53] D. Tonelli,[15] S. Torre,[17] D. Torretta,[15] P. Totaro,[41] M. Trovato[ee],[44] Y. Tu,[43] F. Ukegawa,[53] S. Uozumi,[25] A. Varganov,[32] F. Vázquez[k],[16] G. Velev,[15] C. Vellidis,[3] M. Vidal,[29] I. Vila,[9] R. Vilar,[9] J. Vizán,[9] M. Vogel,[35] G. Volpi[cc],[44] P. Wagner,[43] R.L. Wagner,[15] T. Wakisaka,[39] R. Wallny,[8] S.M. Wang,[1] A. Warburton,[31] D. Waters,[28] M. Weinberger,[51] W.C. Wester III,[15] B. Whitehouse,[54] D. Whiteson[c],[43] A.B. Wicklund,[2] E. Wicklund,[15] S. Wilbur,[11] F. Wick,[24] H.H. Williams,[43] J.S. Wilson,[37] P. Wilson,[15] B.L. Winer,[37] P. Wittich[g],[15] S. Wolbers,[15] H. Wolfe,[37] T. Wright,[32] X. Wu,[18] Z. Wu,[5] K. Yamamoto,[39] J. Yamaoka,[14] T. Yang,[15] U.K. Yang[p],[11] Y.C. Yang,[25] W.-M. Yao,[26] G.P. Yeh,[15] K. Yi[m],[15] J. Yoh,[15] K. Yorita,[56] T. Yoshida[j],[39] G.B. Yu,[14] I. Yu,[25] S.S. Yu,[15] J.C. Yun,[15] A. Zanetti,[52] Y. Zeng,[14] and S. Zucchelli[aa6]

(CDF Collaboration[†])

[1]*Institute of Physics, Academia Sinica, Taipei, Taiwan 11529, Republic of China*
[2]*Argonne National Laboratory, Argonne, Illinois 60439, USA*
[3]*University of Athens, 157 71 Athens, Greece*
[4]*Institut de Fisica d'Altes Energies, ICREA, Universitat Autonoma de Barcelona, E-08193, Bellaterra (Barcelona), Spain*
[5]*Baylor University, Waco, Texas 76798, USA*
[6]*Istituto Nazionale di Fisica Nucleare Bologna, [aa]University of Bologna, I-40127 Bologna, Italy*
[7]*University of California, Davis, Davis, California 95616, USA*
[8]*University of California, Los Angeles, Los Angeles, California 90024, USA*
[9]*Instituto de Fisica de Cantabria, CSIC-University of Cantabria, 39005 Santander, Spain*
[10]*Carnegie Mellon University, Pittsburgh, Pennsylvania 15213, USA*
[11]*Enrico Fermi Institute, University of Chicago, Chicago, Illinois 60637, USA*
[12]*Comenius University, 842 48 Bratislava, Slovakia; Institute of Experimental Physics, 040 01 Kosice, Slovakia*
[13]*Joint Institute for Nuclear Research, RU-141980 Dubna, Russia*
[14]*Duke University, Durham, North Carolina 27708, USA*
[15]*Fermi National Accelerator Laboratory, Batavia, Illinois 60510, USA*
[16]*University of Florida, Gainesville, Florida 32611, USA*
[17]*Laboratori Nazionali di Frascati, Istituto Nazionale di Fisica Nucleare, I-00044 Frascati, Italy*
[18]*University of Geneva, CH-1211 Geneva 4, Switzerland*
[19]*Glasgow University, Glasgow G12 8QQ, United Kingdom*
[20]*Harvard University, Cambridge, Massachusetts 02138, USA*
[21]*Division of High Energy Physics, Department of Physics, University of Helsinki and Helsinki Institute of Physics, FIN-00014, Helsinki, Finland*
[22]*University of Illinois, Urbana, Illinois 61801, USA*
[23]*The Johns Hopkins University, Baltimore, Maryland 21218, USA*
[24]*Institut für Experimentelle Kernphysik, Karlsruhe Institute of Technology, D-76131 Karlsruhe, Germany*
[25]*Center for High Energy Physics: Kyungpook National University, Daegu 702-701, Korea; Seoul National University, Seoul 151-742, Korea; Sungkyunkwan University, Suwon 440-746, Korea; Korea Institute of Science and Technology Information, Daejeon 305-806, Korea; Chonnam National University, Gwangju 500-757, Korea; Chonbuk National University, Jeonju 561-756, Korea*
[26]*Ernest Orlando Lawrence Berkeley National Laboratory, Berkeley, California 94720, USA*
[27]*University of Liverpool, Liverpool L69 7ZE, United Kingdom*
[28]*University College London, London WC1E 6BT, United Kingdom*
[29]*Centro de Investigaciones Energeticas Medioambientales y Tecnologicas, E-28040 Madrid, Spain*
[30]*Massachusetts Institute of Technology, Cambridge, Massachusetts 02139, USA*
[31]*Institute of Particle Physics: McGill University, Montréal, Québec, Canada H3A 2T8; Simon Fraser University, Burnaby, British Columbia, Canada V5A 1S6; University of Toronto, Toronto, Ontario, Canada M5S 1A7; and TRIUMF, Vancouver, British Columbia, Canada V6T 2A3*
[32]*University of Michigan, Ann Arbor, Michigan 48109, USA*
[33]*Michigan State University, East Lansing, Michigan 48824, USA*
[34]*Institution for Theoretical and Experimental Physics, ITEP, Moscow 117259, Russia*

[35] University of New Mexico, Albuquerque, New Mexico 87131, USA
[36] Northwestern University, Evanston, Illinois 60208, USA
[37] The Ohio State University, Columbus, Ohio 43210, USA
[38] Okayama University, Okayama 700-8530, Japan
[39] Osaka City University, Osaka 588, Japan
[40] University of Oxford, Oxford OX1 3RH, United Kingdom
[41] Istituto Nazionale di Fisica Nucleare, Sezione di Padova-Trento, [bb] University of Padova, I-35131 Padova, Italy
[42] LPNHE, Universite Pierre et Marie Curie/IN2P3-CNRS, UMR7585, Paris, F-75252 France
[43] University of Pennsylvania, Philadelphia, Pennsylvania 19104, USA
[44] Istituto Nazionale di Fisica Nucleare Pisa, [cc] University of Pisa,
[dd] University of Siena and [ee] Scuola Normale Superiore, I-56127 Pisa, Italy
[45] University of Pittsburgh, Pittsburgh, Pennsylvania 15260, USA
[46] Purdue University, West Lafayette, Indiana 47907, USA
[47] University of Rochester, Rochester, New York 14627, USA
[48] The Rockefeller University, New York, New York 10065, USA
[49] Istituto Nazionale di Fisica Nucleare, Sezione di Roma 1,
[ff] Sapienza Università di Roma, I-00185 Roma, Italy
[50] Rutgers University, Piscataway, New Jersey 08855, USA
[51] Texas A&M University, College Station, Texas 77843, USA
[52] Istituto Nazionale di Fisica Nucleare Trieste/Udine,
I-34100 Trieste, [gg] University of Trieste/Udine, I-33100 Udine, Italy
[53] University of Tsukuba, Tsukuba, Ibaraki 305, Japan
[54] Tufts University, Medford, Massachusetts 02155, USA
[55] University of Virginia, Charlottesville, VA 22906, USA
[56] Waseda University, Tokyo 169, Japan
[57] Wayne State University, Detroit, Michigan 48201, USA
[58] University of Wisconsin, Madison, Wisconsin 53706, USA
[59] Yale University, New Haven, Connecticut 06520, USA
[60] Istituto Nazionale di Fisica Nucleare Pisa, [bb] University of Pisa,
[cc] University of Siena and [dd] Scuola Normale Superiore, I-56127 Pisa, Italy

PACS numbers:

*Deceased
†With visitors from [a] University of Massachusetts Amherst, Amherst, Massachusetts 01003, [b] Istituto Nazionale di Fisica Nucleare, Sezione di Cagliari, 09042 Monserrato (Cagliari), Italy, [c] University of California Irvine, Irvine, CA 92697, [d] University of California Santa Barbara, Santa Barbara, CA 93106 [e] University of California Santa Cruz, Santa Cruz, CA 95064, [f] CERN,CH-1211 Geneva, Switzerland, [g] Cornell University, Ithaca, NY 14853, [h] University of Cyprus, Nicosia CY-1678, Cyprus, [i] University College Dublin, Dublin 4, Ireland, [j] University of Fukui, Fukui City, Fukui Prefecture, Japan 910-0017, [k] Universidad Iberoamericana, Mexico D.F., Mexico, [l] Iowa State University, Ames, IA 50011, [m] University of Iowa, Iowa City, IA 52242, [n] Kinki University, Higashi-Osaka City, Japan 577-8502, [o] Kansas State University, Manhattan, KS 66506, [p] University of Manchester, Manchester M13 9PL, England, [q] Queen Mary, University of London, London, E1 4NS, England, [r] University of Melbourne, Victoria 3010, Australia, [s] Muons, Inc., Batavia, IL 60510, [t] Nagasaki Institute of Applied Science, Nagasaki, Japan, [u] National Research Nuclear University, Moscow, Russia, [v] University of Notre Dame, Notre Dame, IN 46556, [w] Universidad de Oviedo, E-33007 Oviedo, Spain, [x] Texas Tech University, Lubbock, TX 79609, [y] Universidad Tecnica Federico Santa Maria, 110v Valparaiso, Chile, [z] Yarmouk University, Irbid 211-63, Jordan, [hh] On leave from J. Stefan Institute, Ljubljana, Slovenia,

APPENDIX C

Biography

Martin Johannes Frank was born [redacted] in [redacted] Germany. In 1998, his parents, Dr. Klaus and Jutta Frank, his sister Eva, and he moved to the United States of America. His continuing interest in physics was inspired at Harrison High School in Kennesaw, GA, from which he graduated in 2001. He then attended Emory University in Atlanta, GA where he majored in physics and mathematics and minored in Chinese. In the spring semester of 2004, he studied abroad in Harbin, China. In 2005, he defended his honors thesis in biophysics and anesthesiology, received highest honors in physics, and graduated *summa cum laude* from Emory University. He entered the Ph.D. program in physics at Duke University in the fall of 2005 and transferred to Baylor University as a Presidential Scholar during the summer of 2006. He joined the CDF collaboration that same summer and started working for Prof. Jay Dittmann. He met his wonderful wife, Mary, in the spring of 2007 and they were married on August 7$^{\text{th}}$, 2010.

BIBLIOGRAPHY

[1] R. Barate et al., "Search for the standard model higgs boson at LEP," Phys. Lett. **B565**, 61 (2003).

[2] T. Aaltonen et al., "Combined CDF and DØ upper limits on standard model higgs-boson production with up to 6.7 fb^{-1} of data," (2010).

[3] Standard model higgs cross sections at hadron colliders, `http://maltoni.home.cern.ch/maltoni/TeV4LHC/SM.html`, Retrieved 2/19/2011.

[4] A. Djouadi, J. Kalinowski, and M. Spira, "HDECAY: A program for higgs boson decays in the standard model and its supersymmetric extension," Computer Physics Communications **108**, 56 (1998).

[5] Tevatron luminosity, `http://www.fnal.gov/pub/now/tevlum.html`, Retrieved 2/18/2011.

[6] A. Sill, "CDF run II silicon tracking projects," Nucl. Instrum. Meth. **A447**, 1 (2000).

[7] P. Schmüser, *Feynman-Graphen und Eichtheorien für Experimentalphysiker*, Springer-Verlag Berlin Heidelberg New York, 1995.

[8] K. N. et al. (Particle Data Group), "The review of particle physics," J. Phys. G **37**, 075021 (2010).

[9] J. Baglio and A. Djouadi, "Predictions for higgs production at the tevatron and the associated uncertainties," JHEP **10**, 064 (2010).

[10] J. Keung, E. Thomson, and C. Neu, "Binary mode RomaNN b-tagger efficiencies and scalefactors up to period 23," CDF Internal Note 9898, 2009 (unpublished).

[11] D. Amidei et al., "Calibration of heavy-flavor production in $W + 1$ jet data," CDF Internal Note 9187, 2008 (unpublished).

[12] About fermilab, `http://www.fnal.gov/pub/about/whatis/history.html`, Retrieved 2/18/2011.

[13] Fermilab Operations Department, *Accelerator Concepts Rookie Book*, v3.6 edition, 2010.

[14] Fermilab Operations Department, *Booster Rookie Book*, v4.1 edition, 2009.

[15] R. Blair et al., The CDF II detector technical design report, Technical Report FERMILAB-Pub-96/390-E, Fermilab, 1996.

[16] F. Abe et al., "The CDF detector: an overview," Nucl. Instrum. Methods Phys. Res. Sect. A **271**, 387 (1988).

[17] G. Pauletta, "Operation and performance of the CDF calorimeters," J. Phys.: Conf. Ser. **160**, 012007 (2009).

[18] C. Avila et al., "A measurement of the proton-antiproton total cross section at TeV," Physics Letters B **445**, 419 (1999).

[19] M. M. Block and R. N. Cahn, "High-energy $p\bar{p}$ and pp forward elastic scattering and total cross sections," Rev. Mod. Phys. **57**, 563 (1985).

[20] J. D. Martin Frank, Nils Krumnack, "The XFT monitor," CDF Internal Note 9191, 2008 (unpublished).

[21] W. Badgett et al., "Description of the CDF data structure for run II," CDF Internal Note 4152, 2007 (unpublished).

[22] C. Hays et al., "The COT pattern recognition algorithm and offline code," CDF Internal Note 6992, 2004 (unpublished).

[23] B. Ashmanskas et al., "Open-cell chamber to replace the CTC," CDF Internal Note 3648, 1996 (unpublished).

[24] A. Attal and A. Canepa, "Photon conversion removal efficiency," CDF Internal Note 8073, 2006 (unpublished).

[25] R. G. Wagner, "Electron identification for run II: Understanding and using *Lshr*," CDF Internal Note 6249, 2003 (unpublished).

[26] D. Glenzinski, F. D. Snider, J. Incandela, N. M. Shaw, and W. Yao, "A detailed study of the secvtx algorithm," CDF Internal Note 2925, 1994 (unpublished).

[27] S. Acosta et al., "Introduction to run II jet probability heavy flavor tagger," CDF Internal Note 6315, 2003 (unpublished).

[28] C. Ferrazza and D. Jeans, "A new b & c jet identification algorithm," CDF Internal Note 8451, 2006 (unpublished).

[29] W. K. Sakumoto, "Event $|z_{\rm vtx}| \leq 60$ cm cut acceptance for run II," CDF Internal Note 8318, 2006 (unpublished).

[30] T. Aaltonen et al., "Observation of single top quark production and measurement of $|V_{tb}|$ with CDF," Phys. Rev. **D82**, 112005 (2010).

[31] D. Acosta et al., "Measurement of the $t\bar{t}$ production cross section in $p\bar{p}$ collisions at $\sqrt{s} = 1.96$ tev using lepton + jets events with secondary vertex $b-$tagging," Phys. Rev. **D71**, 052003 (2005).

[32] J. Adelman et al., "Method II for you," CDF Internal Note 9185, 2008 (unpublished).

[33] B. Cooper and A. Messina, "Estimation of the background to $W^{\pm} \to e^{\pm}\nu + n$ jet events," CDF Internal Note 7760, 2005 (unpublished).

[34] R. Barlow and C. Beeston, "Fitting using finite monte carlo samples," Computer Physics Communications **77**, 219 (1993).

[35] Franklin et al., "Heavy-flavor content of the W + jets sample," CDF Internal Note 8765, 2007 (unpublished).

[36] Franklin et al., "Calibration of heavy-flavor production in QCD data," CDF Internal Note 8768, 2007 (unpublished).

[37] W. Johnson and T. Junk, "Secvtx mistag matrices for 5.6 fb^{-1} of data up to p28," CDF Internal Note 10179, 2010 (unpublished).

[38] J. Freeman, "Summer 2009 secvtx mistag asymmetry corrections through period 22," CDF Internal Note 9847, 2009 (unpublished).

[39] B. Alvarez et al., "Combined jet probability-secvtx tag rate matrix for gen6 2.2 fb^{-1} data," CDF Internal Note 9228, 2008 (unpublished).

[40] J. Keung et al., "Binary mode RomaNN b-tagger mistag rates up to period 23," CDF Internal Note 9900, 2009 (unpublished).

[41] Y. Nagai et al., "Search for the standard model higgs boson production in association with $W^{\pm}$ boson using $\int Ldt = 4.3$ fb^{-1}," CDF Internal Note 9868, 2009 (unpublished).

[42] T. Aaltonen et al., "Neural network b-jet energy correction for WHNN analysis," CDF Internal Note 9858, 2009 (unpublished).

[43] M. McFarlane et al., "Study of high p_T lepton identification efficiency scale factor and related cuts and parameters in 5.3.3," CDF Internal Note 7682, 2005 (unpublished).